

CIRCULAR DICHROISM STUDIES OF SPIN DYNAMICS IN
4-AMINOMETHYL PIPERIDINIUM METHYL AMMONIUM
LEAD IODIDE PEROVSKITE QUANTUM WELLS

by

Drew Riley

Submitted in partial fulfillment of the requirements
for the degree of Master of Science

at

Dalhousie University
Halifax, Nova Scotia
December 2018

© Copyright by Drew Riley, 2018

This thesis is dedicated to Dorothy Tychie, whose love of education and travel has forever influenced me.

*“His locked, letter’d, braw brass collar
Shew’d him the gentleman an’ scholar;
But though he was o’ high degree,
The fient a pride, nae pride had he;
But wad hae spent an hour caressin,
Ev’n wi’ al tinkler-gipsy’s messin:
At kirk or market, mill or smiddie,
Nae tawted tyke, tho’ e’er sae duddie,
But he wad stan’t, as glad to see him,
An’ stroan’t on stanes an’ hillocks wi’ him. ”*

-Robert Burns

Table of Contents

List of Tables	vi
List of Figures	vii
Abstract	ix
List of Abbreviations and Symbols Used	x
Acknowledgements	xii
Chapter 1 Introduction	1
1.1 Overview	1
1.2 Bulk Semiconductors	8
1.2.1 Effects of Confinement on Semiconductors	11
1.3 2D Perovskite Materials	12
1.4 Optical Excitation	15
1.5 Dynamic Processes in Semiconductors	19
1.5.1 Ultrafast Probes of Carrier Dynamics	20
1.6 Rashba Effect in Semiconductors	23
1.7 Literature Review	23
1.7.1 Perovskite Photovoltaics	23
1.7.2 2D Perovskite	25
1.7.3 Spin-Orbit Coupling in Perovskite Materials	26
1.7.4 Spin-Dynamics in Perovskite Materials	29
1.7.5 Spintronic Applications of Perovskite Materials	31
1.8 Outline of Thesis	31
Chapter 2 Theoretical Considerations	33
2.1 Optical Selection Rules	33
2.1.1 Electronic Structure of Semiconductors Including Spin-Orbit Coupling	33
2.1.2 Optical Transitions in Semiconductors	35
2.2 Mechanisms of Spin Relaxation	37
2.2.1 Bir-Aronov-Pikus	37

2.2.2	Elliot-Yafet	39
2.2.3	D'yakonov-Perel	40
2.3	Symmetry Dependent Effects of Spin-Orbit Coupling	41
Chapter 3	Experimental Techniques	44
3.1	Sample Fabrication	44
3.1.1	Precursor Crystals	44
3.1.2	Thin Films	44
3.2	Linear Absorbance	45
3.2.1	Tauc Analysis	46
3.3	X-ray crystallography	48
3.4	Ultrafast Laser Source	50
3.4.1	Verdi-V18 Pump Laser	50
3.4.2	Mira HP-F	51
3.4.3	APE Optical Parametric Oscillator (OPO)	53
3.5	Ultrafast Spectroscopy Techniques	54
3.5.1	Differential Transmission	54
3.5.2	Circular Dichroism	57
3.5.3	Calibration of Quarter Wave Plates	58
Chapter 4	Results and Discussion	61
4.1	Photo Induced Degredation	61
4.2	Differential Transmission	62
4.3	Circular Dichroism	64
Chapter 5	Conclusion	72
Bibliography	74
Appendix A	Rights and Permissions	83
A.1	Figure 1.10 and Figure 4.9 (b) and Figure 2.2 (c)	83
A.2	Figure 1.4 (b)	84
A.3	Figure 1.4 (d)	85
A.4	Figure 1.14	86

A.5	Figure 1.15 (a)	87
A.6	Figure 1.17	88
A.7	Figure 2.2 (a) and (b)	89
A.8	Figure 3.3 (b) and (c)	90
A.9	Figure 4.9 (a)	91

List of Tables

2.1	Optical Selection Rules in GaAs from Electric Dipole Approximation	38
-----	--	----

List of Figures

1.1	Perovskite Crystal Structure	2
1.2	Solar Cell Efficiencies of Emerging Technologies	4
1.3	Solar Cell Architecture	4
1.4	Schematics for Various Spintronic Applications	6
1.5	SFET Schematic	7
1.6	Band Structure of Semiconductors	10
1.7	Schematic of a Semiconductor Quantum Well and the Associated Band Diagrams	12
1.8	2D Perovskite Crystal Structure	13
1.9	2D Perovskite Band Structure	14
1.10	Ruddlesden Popper and Dion Jacobson Perovskite Structures .	15
1.11	Optical Absorption in Bulk Semiconductors, Quantum wells, and Ruddlesden Popper Perovskites	18
1.12	Differential Transmission in Direct Band Gap Semiconductors .	21
1.13	Dispersion Relation for Rashba Splitting	24
1.14	Band structure for MAPbI ₃	27
1.15	Measured Rashba Splitting for Perovskite Structures	29
1.16	SFET Schematic	30
1.17	Schematic of Perovskite Based Optoelectronic-Spintronic Applications	31
2.1	Crystal and Band Structure of GaAs	34
2.2	Spin Orbit Coupling Effects in 2D Perovskites	35
2.3	Optical Selection Rules	38
2.4	Rashba Magnetic Field for Cases of Bulk Inversion Asymmetry In and Out of Plane	43

3.1	Linear absorption for 4AMP from Dalhousie and North Western University	47
3.2	Tauc Analysis of 4AMP	47
3.3	Schematic of XRD apparatus and XRD Results for 2D Perovskites	48
3.4	X-Ray Diffraction Results for Sister Sample Created at North Western University	50
3.5	Schematic Overview of Laser Source	51
3.6	Schematic of Mira HP-F	52
3.7	Schematic of APE OPO	55
3.8	Schematic of the Transient Absorption Apparatus	57
3.9	Schematic of the Differential Transmission Apparatus	58
3.10	Schematic of the Circular Dichroism Apparatus	59
3.11	Schematic of the Quarter Wave Plate Calibration Apparatus .	60
4.1	Photo Induced Degradation Test	62
4.2	Differential Transmission Signal for 38 meV above gap excitation	63
4.3	Differential Transmission Signal for Various Excitation Energies	64
4.4	Magnitude of the Differential Transmission Signal as a Function of Detuning	65
4.5	Circular dichroism results for 38meV above gap excitation . .	66
4.6	Examples of Circular Dichroism Results for Various Laser Detunings	67
4.7	Degree of Circular Polarization and Spin Lifetime as a Function of Laser Detuning	68
4.8	Spin Lifetime as a Function of Laser Fluence	69
4.9	Calculated Band Structure for BZ_2PbCl_4 and Molecular Structure Calculations for $(3\text{AMP})\text{MAPb}_2\text{I}_7$	71

Abstract

Two dimensional perovskites are planes of perovskite octahedra confined by an organic spacing layer, making a multiple quantum well structure. The structure of the organic spacing molecule causes distortions to the perovskite sheet which impacts the electronic and optoelectronic properties of the material. Using pump probe circular dichroism the spin dynamics of the 2D perovskite (4AMP)MAPb₂I₇ are reported and compared to a material with the same perovskite sheet but a different spacing molecule (BA₂MAPb₂I₇). The spin lifetime in (4AMP)MAPb₂I₇ was found to be 15 ps and decreased with increasing excitation energy, consistent with BA₂MAPb₂I₇. It was found that the spin lifetimes in (4AMP)MAPb₂I₇ had no dependence on carrier density over two orders of magnitude, contrary to BA₂MAPb₂I₇. This is attributed to the lack of out-of-plane tilting in (4AMP)MAPb₂I₇, which leads to a suppression of the precessional spin relaxation in this material.

List of Abbreviations and Symbols Used

E_G	Band Gap - the difference in energy between the highest occupied band and the lowest unoccupied band.
μ	Carrier Mobility - a measure of the ease of movement of a carrier through a lattice.
τ	Carrier Lifetime - The average time after excitation for a carrier to undergo an inter band decay process.
τ_s	Spin Lifetime - The average time for a fully spin polarized ensemble of carriers to decay to a statistically random distribution.
τ_{th}	Carrier Thermalization Time - The average time required for an excited distribution of carriers to reach quasi-equilibrium with the lattice.
L_D	Diffusion Length - a measure of the distance an excited carrier can travel through a lattice before recombination occurs.
4AMP	4-Aminomethyl Piperidinium Methyl Ammonium Lead Iodide $((C_6N_2H_{16})(CH_3NH_3)_{n-1}Pb_nI_{3n-1})$ - a Dion Jacobson perovskite
BA	Buytalamonium Methylammomium Lead Iodide $(BA_2MA_{n-1}Pb_nI_{3n-1})$ - a Ruddlesden Popper perovskite.

- BAP** Bir-Aronov-Pinkus - a spin relaxation mechanism occurring primarily in p-doped semiconductors.
- DP** D'yakonov perel mechanism - a spin relaxation mechanism occurring between momentum scattering events.
- EY** Elliot-Yafet Mechanism - a spin relaxation mechanism occurring during momentum scattering events.
- OPO** Optical Parametric Oscillator - a laser cavity used to up convert the Mira HP-F into the visible part of the spectrum.
- PEA** $(\text{PEA})_2(\text{MA})_2\text{Pb}_3\text{I}_7$ - a Ruddlesden Popper perovskite.
- SOC** Spin-Orbit Coupling - a relativistic interaction of a particle's spin with its motion inside a potential.
- XRD** X-Ray Diffraction - a experimental technique used to evaluate the structure and elemental components of a solid state crystal.

Acknowledgements

First and foremost I would like to thank all members, past and present, of the Hill and Hall groups at Dalhousie University. This work truly was a combined effort of many wonderful people. To Professor Kimberley Hall thank you for hosting me in your group and working patiently with me through the creation of this thesis. The knowledge you have imparted to me over the past few years will carry me farther than I ever thought possible. To Ajan, my go to consultant, thank you for all your help in the lab, advice you have given me, and for spending countless hours with me leak checking cryostat lines. To Sam, your unending ability to see the bright side of life has inspired me to re-evaluate my perspective. Thank you for teaching me the basics of the lab oh so long ago, I hope that we will work together in the future. To Seth, who laid the ground work for this thesis to progress, thank you for all the time you've spent organizing your notes and guiding me towards my conclusions. I hope that your future includes all the scotch, golf, and intramural championships fancy lawyer money can buy. To previous members of the Hall group, Dan, Ruble, Ali, our time together was too short. Thank you for all the time you have taken to create a user friendly lab. To Ian Hill, thank you for the use of your laboratory and equipment therein, this thesis could not have been completed without it. To Charlotte Clegg, thank you for all the time and care you have taken in answering my many questions about chemistry magic no mortal physicist could understand. To those collaborators at North Western University I would like to thank you for taking the time to host me and for all the knowledge imparted during my visit. To Constantinos Stoumpos thank you for spending the time necessary to bridge the chemistry/physics language barrier. To Justin Hoffman, thank you for all the time and effort you put into making my visit instructive and very worth while.

I would like to acknowledge all the support I have had from friends and family over the course of my education. To my mom Susan, thank you for all the support in living and working far away from home. I know you will visit me no matter where I end up. To my sister Chloe, thank you for your unending support and love. You

truly are the one I can count on. To Luke and Steve, thank you for getting me out of the city and to the beach as much as possible. I know that there are many more waves in many more countries for us to ride together. To Heather, thank you for all the support you've given me over the past two months. Keeping me fed and sane has allowed me to create this work.

Finally I would like to acknowledge the countless other perovskite researchers working diligently in labs throughout the world, as well as all the physicists and scientist throughout the ages. Without their work and efforts to stand on I would never have been able to see so far.

Chapter 1

Introduction

1.1 Overview

Demand for innovations in solid state electronic devices such as transistors, integrated circuits, diodes, solar cells, relays, and hard disks is on the rise, especially given the need to develop lower cost approaches to these technologies for use in developing nations and the quest for devices that take less energy both to produce and operate. Traditional solid state devices are typically silicon based. Although silicon is abundant in the earth's crust, it suffers from an expensive and energy intensive fabrication process [1]. The development of inexpensive alternatives to silicon using materials that could be deposited using low-cost solution processing techniques could open up a new era of cheap electronics. This has led to a surge of research into organic [2], and hybrid organic-inorganic materials [3].

One class of hybrid materials is known as perovskites. The crystal structure of a hybrid perovskite consists of corner sharing octahedra with an anion in each corner, surrounding a large cation, and bonded together by a smaller cation. Figure 1.1 shows the structure for the perovskite unit cell. These materials are described as organic-inorganic because the anion and large cation are inorganic materials while an organic constituent plays the role of the smaller cation. One of the most common material combinations studied in this class of materials is $\text{CH}_3\text{NH}_3\text{PbI}_3$, in which the inorganic matrix is formed by the lead-iodide octahedral and is stabilized by the organic molecule methyl ammonium. Bulk perovskite materials have the general formula ABX_3 . This structure was first characterized by Lev A Perovski for CaTiO_2 . Other naturally occurring perovskites include Calcium titanate (CaTiO_3), Loparite ($(\text{Ce,Na,Ca})(\text{Ti,Nb})\text{O}_3$) and Bridgmanite ($(\text{Fe,Mg})\text{SiO}_3$). A perovskite with a halogen as X, such as MAPbI_3 , MAPbBr_3 , or MAPbCl_3 , are known as halide perovskites. Halide perovskites were first synthesized by C.K. Moller in 1958 [4].

Hybrid organic-inorganic perovskites possess a number of interesting physical

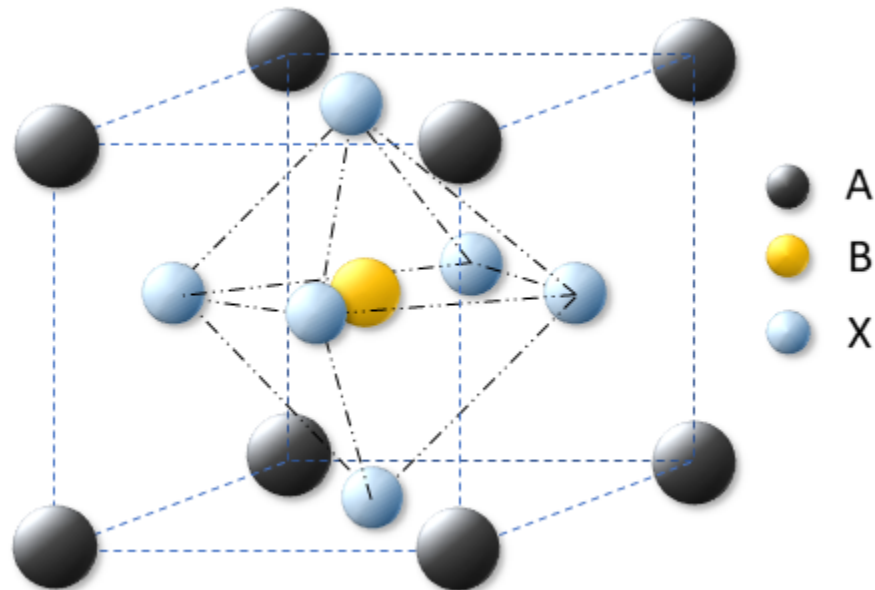


Figure 1.1: The crystal structure of an ABX₃ perovskite. The X site forms the corner sharing anion octahedra bound together through hydrogen bonding with the A site monovalent cation, the B site is occupied by a large divalent cation.

properties. For example, the organic constituents can undergo tumbling and other dynamic configuration changes at elevated temperatures. Together with the large size of the unit cell, this leads to a complex spectrum of phonon modes [5, 6]. The optical and electrical transport properties of these materials are also strongly affected by the hybrid nature of the crystal structure. Under optical excitation by a photon of energy exceeding the band gap, an electron is promoted from the valence band to the conduction band leaving behind a vacancy, which is often thought of as an excess positive charge known as a hole. The electrons and holes are the charge carriers that conduct current in an electronic device fabricated from the semiconductor. The strength of optical absorption is very large in perovskites [7]. In addition, despite the fact that perovskites are created through solution processing and so possess a large number of crystal defects, experiments have shown that charge carriers can undergo transport over long distances before the electron relaxes back down to the valence band, with diffusion lengths as long as 1 micron [8]. Furthermore, there are a variety of alternatives for the material constituents, and it is possible to realize perovskite

structures that naturally form into two-dimensional sheets of octahedra, confining the movement of electrons and holes to the sheet. This flexibility, together with the beneficial properties of these materials for optoelectronics, has led to the demonstration of a whole host of electronic and optoelectronic devices using these materials including light emitting diodes [9], microelectronics [10–12], telecommunications [13], lasing [14, 15] and photovoltaics [3, 16].

Among the optoelectronic devices that are being explored as potential applications of perovskites, photovoltaic applications (such as solar cells) have received by far the most attention. This is because the efficiency of perovskites-based solar cells, specifically those based on $\text{CH}_3\text{NH}_3\text{PbI}_3$, have undergone the fastest rise in solar cell efficiency of any technology in history. Figure 1.2 shows the maximum laboratory efficiency of emerging photovoltaic technologies since 1975 [17]. Perovskites based cells are represented by orange circles with yellow interior and can be seen to rise at a much steeper rate than any other technology. The typical structure for a hybrid organic-inorganic solar cell is shown in Figure 1.3. Photons from the sun are absorbed in the perovskite layer and the resulting electrons and holes are free to move through into other parts of the stack. An electron-transport material is deposited above the absorbing layer such that electrons will preferentially enter this material, which acts as a funnel to move electrons through the circuit. Similarly the hole-transport material is deposited below the absorbing layer and serves to “collect” holes, funnelling positive charge in the reverse direction through the circuit. The high absorption coefficient in the solar spectrum and the good electrical transport properties of $\text{CH}_3\text{NH}_3\text{PbI}_3$ are believed to be responsible for the rapid increase in solar cell efficiencies using these materials.

The hybrid organic-inorganic perovskites also possess interesting spin-related properties, making these materials of interest for spin-based electronics (also referred to as spintronics). The goal of the spintronics research field is to develop new technologies, or improve upon existing devices (*e.g.* by lowering the power consumption), by exploiting the spin property of the electron. Commercial spintronic technologies include semiconductor lasers incorporating integrated optical isolators fabricated from diluted magnetic semiconductors [18] and magnetic random access memory that

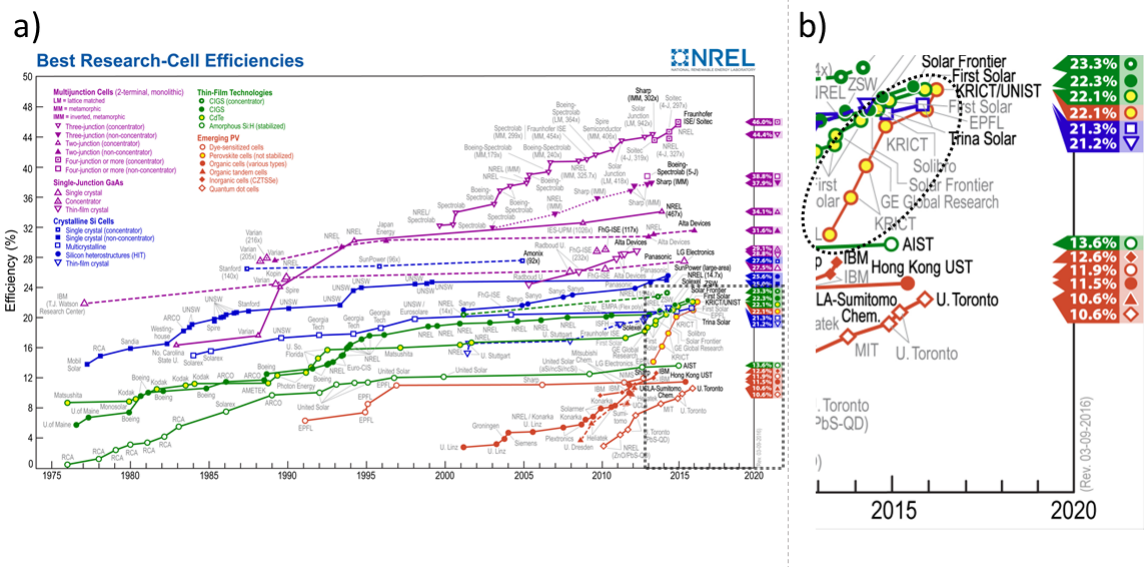


Figure 1.2: (a) The laboratory solar cell efficiencies of emerging photo-voltaic technologies. Orange circles with yellow interior indicate perovskite based solar cells. (b) enhanced version of the dotted region to highlight perovskites advances.

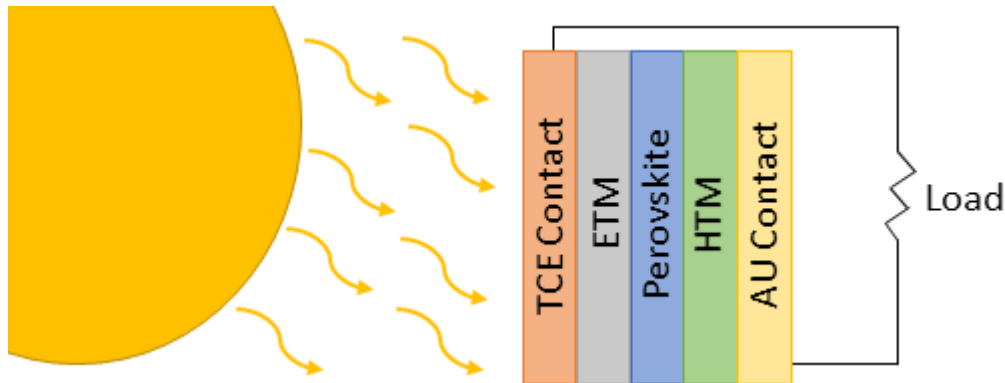


Figure 1.3: The architecture of a solar cell consisting of a transparent conductive electrode (TCE) as a top contact, an electron-transport material (ETM), a perovskite layer, a hole-transport material (HTM), a gold bottom contact, connected to a external load.

exploits magnetoresistance in a layered structure of metallic ferromagnetic materials [19, 20]. A number of other potential technologies have been proposed, including all optical switches that exploit spin relaxation of charge carriers, semiconductor lasers that exploit the spin degree of freedom to lower the threshold current, and spin-field effect transistors that exploit the spin degree of freedom to control the flow of current

between the source and the drain [21–23].

Perovskites are of interest for applications in this area because their excellent optical and charge transport properties are accompanied by strong spin-orbit coupling (SOC), due to the incorporation of heavy elements such as lead and iodine [24]. The SOC Hamiltonian in a semiconductor can be expressed as:

$$H_{\text{SO}} = \frac{\hbar}{4m_e^2c^2} \nabla V(\vec{r}) \times \mathbf{P} \cdot \boldsymbol{\sigma} \quad (1.1)$$

In equation 1.1, $V(\vec{r})$ is the potential experienced by the electrons and may contain both contributions from the periodic potential of the crystal and an externally applied potential, m_e is the electron mass, c is the speed of light, \mathbf{P} is the momentum operator, and $\boldsymbol{\sigma}$ are the Pauli spin matrices. Since $\nabla V(\vec{r})$ appears in equation 1.1, spin-orbit coupling reflects the interaction of the electrons spin with the electric fields in the crystal. From the form of the spin-orbit interaction, a moving electron (*i.e.* an electron with non-zero momentum) will experience these electric fields as an effective magnetic field $\boldsymbol{\Omega} \propto \nabla V(\vec{r}) \times \mathbf{P}$. This effective magnetic field may be exploited in a spintronic device since it provides a way to control the spin states of an electron. When the spin-orbit coupling is large, a small externally-applied electric field will produce a large effective magnetic field, allowing for a rapid manipulation of the spin state.

Contributions to the spin-orbit effective magnetic field in a semiconductor may be classified according to the source electric fields, all of which introduce inversion asymmetry to the crystal. When the electric fields are tied to the polar bonding in the crystal structure, the contribution to $\boldsymbol{\Omega}$ is called bulk inversion asymmetry. When an external electric field is applied, or an asymmetry is built-in to a structure (e.g. through layered growth), the contribution is referred to as structural inversion asymmetry. Bychov and Rashba analyzed the latter effect for electrons in a two-dimensional electron gas [25]. Following such work, all such effects are often termed Rashba effects. In addition to the effective magnetic field that can be used to operate on the electron spin, Rashba effects also lift the degeneracy of the two spin states of the electron within the bands away from $\vec{k} = 0$. This splitting can be used to realize spin-dependent transport [26].

Although few spintronic applications have made their way to large markets (save for magnetoresistive random-access memory (MRAM)) many potential applications

exist. These include: magnetic tunnel transistors [27], optical switches [28–30], antiferromagnetic storage [31], spin-cavity resonators for quantum information processing [32], integrated optical isolators [33], spin-valve electronics [34], and spin field-effect transistors (SFET) [35]. Figure 1.4 shows schematics for a few simple spintronics applications. Figure 1.5 shows a schematic diagram of an spin field-effect transistor. This device controls the flow of current through the channel by controlling the spin-state of the charge carriers, effectively stopping the flow of charge when the gate voltage is high.

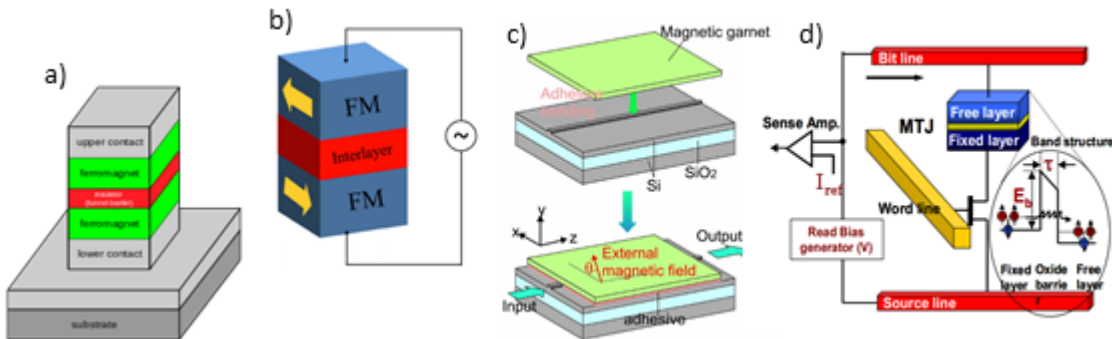


Figure 1.4: Assorted spintronic applications (a) a magnetic tunnelling junction (adapted from reference [36]), consisting of two ferromagnets isolated by a thin ($\leq 10\text{nm}$) electrical insulator. Switching of the relative polarizations of the two ferromagnets allows for a change in tunnelling resistance through the insulator. This switching activity is the basis for many spintronic applications. (b) A spin valve (adapted from reference [37]), consisting of two ferromagnetic domains, one of which is “pinned” i.e. the magnetization is insensitive to moderate external fields, while the other is “free” and can be manipulated with a relatively small applied field. A measurement of the resistance can then be a measure of the external field in the region (magnetic sensor application) or a binary storage mechanism (magnetic hard drive storage). (c) An optical isolator (adapted from reference [38]), this device rotates the polarization of light between the input and outputs of the isolator, in combination with a polarization filter at the input/output, this can allow light to propagate through the circuit in one direction. Optical isolators are used to limit unwanted feedback into optically insulated electronic chips or a laser cavities. (d) A Magnetic Random Access Memory read/write head (adapted from reference [39]), a non-volatile memory storage system based on a magnetic tunnelling junction system. The bit and source line hold a potential across a magnetic tunnelling junction and measure the resistance, application of a voltage to the word line can alter the orientation of the free layer, changing the systems resistance, and effectively changing the logic held in the bit.

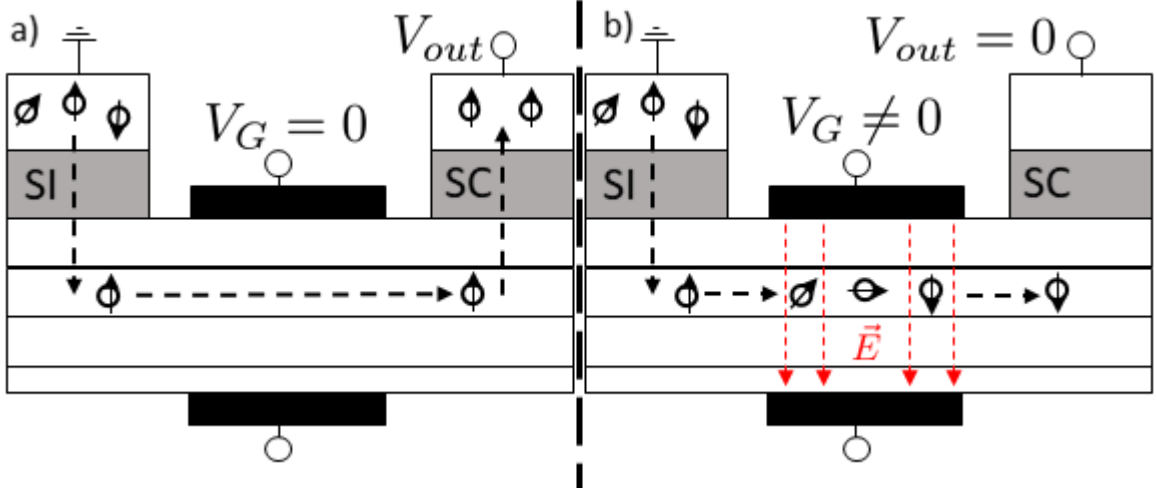


Figure 1.5: A Schematic diagram for a non-magnetic spin-field effect transistor. (a) When the gate voltage is low, the electrons pass unimpeded to the drain, creating a high output. (b) When the gate voltage is high precessional relaxation is induced causing the spins to re-orient to a statistically random sample, creating a low output. SI-spin injector. SC-spin collector. V_G -gate voltage.

The spin-related properties (including the Rashba effect) of inorganic semiconductors (in particular III-V materials such as GaAs, which possess bulk inversion asymmetry) have been studied extensively over the past two decades [40]. Such materials have also been the focus of the majority of efforts to develop semiconductor spintronic devices to date [41]. In contrast very little is known about the spin-related properties of perovskites. Only a few studies of the dynamics of electron spin have been carried out in these materials [42–45] and the mechanism of spin relaxation has not yet been identified. In addition, despite numerous theoretical predictions of Rashba effect in perovskites [46–50], only three reports have emerged claiming to provide direct experimental evidence of such effects [42, 44, 45].

This thesis aims to shed light on the spin-related properties of the two-dimensional perovskite material (4AMP)MAPb₂I₇. For a two-dimensional perovskite, the transport of electrons and holes is confined to two-dimensional sheets separated by insulating organic layers. 2D perovskites have also shown great promise for application in solar cells because the organic sheets protect the material from moisture degradation, which is a key barrier to wide scale adaptation of solar cells based on the bulk perovskite MAPbI₃ [51–53]. In this thesis work, measurements are made of

the spin lifetime in (4AMP)MAPb₂I₇ as a function of the density of optically-injected electron-hole pairs and the carrier energy. This work builds directly upon studies of a similar perovskite structure (BA₂MAPb₂I₇) by a previous masters student [45, 54], which revealed a Rashba effect detected through the spin relaxation time. The (4AMP)MAPb₂I₇ material studied in this work is expected to have differing spin related properties than BA₂MAPb₂I₇ because the symmetry-breaking directions differ for the two materials (for BA₂MAPb₂I₇, the symmetry breaking direction is along the stacking direction of the sheets, while for (4AMP)MAPb₂I₇ it is in the plane of the sheets). Our findings confirm the absence of an impact of the Rashba effect on the spin dynamics, as expected from the symmetry in (4AMP)MAPb₂I₇. This work will aid in the development of spintronic devices using perovskite materials. By providing insight into the fundamental properties of 2D perovskites, this work will also support the development of stable solar cells featuring this material.

This chapter is organized as follows. Section 1.2 will formally introduce the concepts of semiconductors including important insight into the impact of quantum confinement on the band structure. Section 1.3 will introduce how these confinement effects can be incorporated into perovskite semiconductors. Section 1.4 will introduce how charge carriers can be injected into a semiconductor using a light source, including the expected effects of quantum confinement. Section 1.5 introduces the dynamic processes that occur in semiconductors after excitation has occurred. Section 1.7 gives an up-to-date review of the literature of 3D (1.7.1) and 2D (1.7.2) perovskite materials, theoretical studies on the effects of SOC in perovskite materials (1.7.3), experimental studies of the spin-dynamics in perovskites (1.7.4), and existing applications of perovskite to spintronics (1.7.5.)

1.2 Bulk Semiconductors

A band structure describes the allowable energies states an electron can occupy in a solid crystal. These states arise from the quasi-continuous splitting of atomic energy levels due to interactions between the many ionic cores (and core electrons) in the solid [55]. This can be described by the nearly free electron model, in which the ions and core electrons are treated as a weak periodic potential ($V(\vec{r})$), with the periodicity of the lattice, \vec{R} . The wavefunctions of the electron are found by solving

the time-independent Schrödinger equation.

$$\left(\frac{-\hbar}{2m_e} \nabla^2 + V(\vec{r}) \right) \psi(\vec{r}) = E\psi(\vec{r}) \quad (1.2)$$

where $V(\vec{r}) = V(\vec{r} + \vec{R})$. Periodic solutions to Equation 1.2 are known as Bloch functions, expressed as:

$$\psi(\vec{r}) = U_k(\vec{r}) e^{i\vec{k} \cdot \vec{r}} \quad (1.3)$$

which are a product of a plane wave with a Bloch envelope function, $U_k(\vec{r})$, that shares the periodicity of the lattice. The energy eigenvalues, near the zone center, are described by:

$$E = \frac{\hbar^2 \vec{k}^2}{2m^*} \quad (1.4)$$

where m^* is the effective mass of the electrons, which differs from the bare electron mass due to the coupling of the electron with the lattice of ion cores in the crystal. The solutions in equation 1.3 describe the allowed states for an electron inside the crystal. There is a band associated with each orbital in the unit cell of the crystal, each characterized by its own effective mass. The band gap (E_G) is the difference in energy between the highest occupied band, known as the valence band, and the lowest unoccupied band, known as the conduction band. A direct band gap is one where the conduction band minimum and valence band maximum occur at the same wavevector. Figure 1.6 illustrates the highest energy valence and lowest energy conduction bands for a direct band gap semiconductor plotted as a function of the electron's wavevector.

The number of conduction band states ($\rho_c(E)$) between E and $E + dE$ will be given by $\rho_c(E)dE = \rho(k)dk$, where $\rho(k)$ is the density of states in a 3D electron gas (k^2/π^2). Therefore the density of allowed energies in the conduction band will be given by:

$$\rho_c(E) = \frac{k^2}{\pi^2} \left(\frac{dE}{dk} \right)^{-1} \quad (1.5)$$

Using equation 1.4 to find the derivative and combining with equation 1.5 we find the density of states in the conduction band to be:

$$\rho_c(E) = \frac{\sqrt{2}(m_c)^{3/2}}{2\pi^2 \hbar^3} (E - E_c)^{1/2} \quad (E \geq E_c) \quad (1.6)$$

where E_c is the lowest energy level in the conduction band, and m_c is the effective mass in the conduction band. Similarly, defining the highest energy in the valence

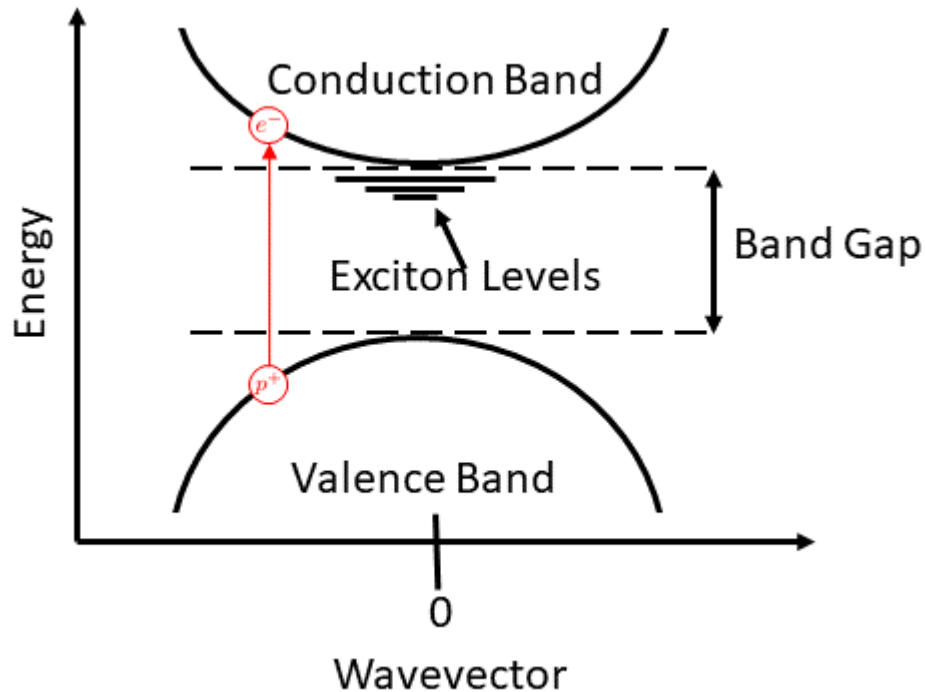


Figure 1.6: Simplest representation of a direct band gap semiconductor. The conduction band represents the lowest unoccupied electronic states, while the valence band represents the highest occupied states. The red line indicates a vertical transition from the valence band to the conduction band induced by the absorption of a photon.

band as E_v , we find the density of states for the valence band to be:

$$\rho_v(E) = \frac{\sqrt{2}(m_v)^{3/2}}{2\pi^2\hbar^2} (E_v - E)^{1/2} \quad (E \leq E_v) \quad (1.7)$$

where m_v is the effective mass in the valence band, so that the density of states near the band edges goes as the square root of the excess energy of the carrier.

Since the band gaps of semiconductors are relatively small (1 – 9 eV) the electronic properties can be manipulated through changes in temperature, doping, and illumination. This allows semiconductors to be used in many applications including transistors, LED's, solar cells, optical detectors, thermocouples, and Hall effect sensors to name a few.

1.2.1 Effects of Confinement on Semiconductors

The electrical properties of a semiconductor can be modified if the dimensions of the material are made sufficiently small, typically less than 10 nm. These systems can be achieved by shrinking a solid in one dimension creating a confined nano-sheet, or quantum well [56–58], in two dimensions creating a confined nano-wire [59,60], or in three dimensions creating a quantum dot [61,62]. Confining the structure changes the allowed energy states the carriers can occupy which radically alters the electrical properties from the three-dimensional case. Applications for confined systems include solar cells [63], single photon sources [64], quantum computation [65], solid lubricants [66], flexible electronics [67], photocatalysts [68], and LED's [69].

To gain insight into the influence of confinement on the electrical states of a semiconductor, consider confining a bulk material in one-dimension (the z-dimension) to a thickness L. In the bulk case, the wavefunction is a propagating wave with allowed wavevectors that form a quasicontinuum in all k_x, k_y , and k_z . Imposing the boundary conditions in a quantum well that the wavefunction must vanish at the edges of the well leads to a discrete set of allowed wavevectors in the z direction:

$$k_{nz} = \frac{2\pi}{\lambda_{nz}} = \frac{n\pi}{L} \quad (n = 1, 2, 3 \dots) \quad (1.8)$$

and the allowable energy eigenvalues become quantized as:

$$E_n = \frac{\pi^2 \hbar^2}{2m^* L^2} n_z^2 + \frac{\hbar^2 k_x^2}{2m^*} + \frac{\hbar^2 k_y^2}{2m^*} \quad (n_z = 1, 2, 3, \dots) \quad (1.9)$$

The eigenfunctions become:

$$\Psi(\vec{r}) = \sqrt{\frac{2}{L}} \sin(k_n z) e^{i(k_x x + k_y y)} \quad (1.10)$$

which are standing waves in the z direction, but travelling waves in the x and y directions. One can manufacture a semiconductor quantum well by growing one layer of a semiconductor on top of a flat monolayer of another semiconductor with differing band gaps. Figure 1.7 (a) shows a schematic of this structure, where the blue layer has a larger band gap than the confined yellow layer. Figure 1.7 (b) shows the highest energy in the valence band and the lowest energy in the conduction band as a function of z, as well as the first two confined solutions for each band. Electrons in this structure would be confined to move only within the yellow layer. Multiple

quantum wells can be made through the sequential deposition of these layers on top of one another. Figure 1.7 (c) shows how confinement affects the band structure. For each value of n_z , a subband exists representing in plane motion of the electron.

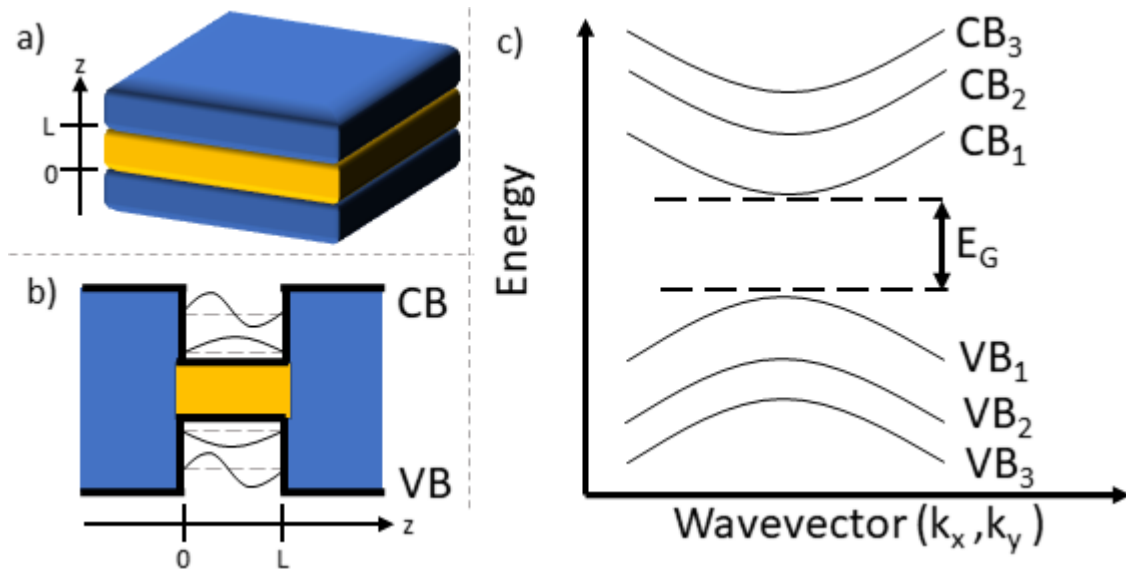


Figure 1.7: (a) A schematic and (b) band diagram of a semiconductor quantum well. The blue semiconductor has a higher band gap than the yellow semiconductor. Electrons in this structure will be confined to move in the yellow semiconductor. (b) The energy splitting caused by the confinement of electrons in the well. Each band splits into subbands, one for each value of n_z in equation 1.9. This shows the discretization of the available energy states in a confined structure.

1.3 2D Perovskite Materials

2D perovskites are composed of two dimensional sheets of the same octahedra present in the bulk perovskite (Figure 1.1). The octahedral sheets are separated from one another by a spacer layer that corresponds to a bilayer of long organic cations. The most general formula for this type of perovskite is $((\text{RNH}_3)_{(2,1)}\text{A}_{n-1}\text{B}_n\text{X}_{3n+1})$. Here RNH_3 is a large aliphatic or aromatic alkylammonium spacer cation that forms a spacer layer between the sheets of metal halide octahedra, and n indicates the number of layers of octahedra in each sheet. The subscript (2,1) indicates the charge of the spacer cation and dictates the phase of the 2D perovskite. These can be categorized

as Ruddlesden Popper ($((\text{RNH}_3)_2 \dots)$) and Dion Jacobson phases ($((\text{RNH}_3)_1 \dots)$). Ruddlesden Popper perovskites' spacing layer is made up of two sheets of (+1) cations, while Dion Jacobson perovskites' have one sheet of (+2) cations. Figure 1.8 shows a schematic representation of a 2D perovskite for various n values. As n tends towards infinity, the perovskite tends towards the bulk case. Figure 1.9 shows a schematic of the band diagram for a perovskite thin film (for the $n = 2$ case). As the spacer molecule has a much larger band gap and lower electron affinity than the perovskite layer, this structure represents a multiple quantum well. The barrier height is determined by the difference in band gap between the spacer molecule and the perovskite layer, the width of the well is determined by the layer number (n), and the band gap is determined by the perovskite material. Here the electrons will be confined to move in the perovskite material.

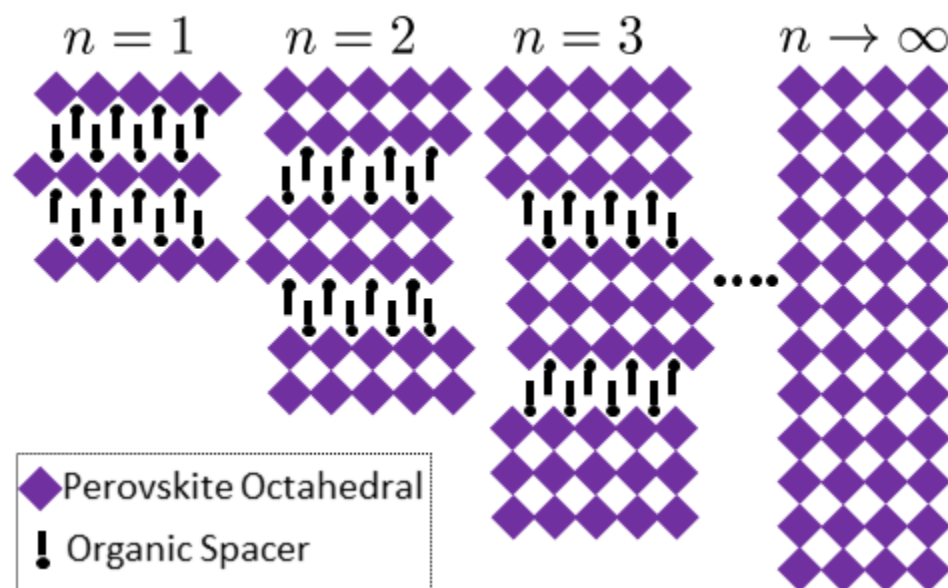


Figure 1.8: The crystal structure of 2D Ruddlesden Popper Perovskites. Here the perovskite octahedra are separated by the organic spacer molecule. As the layer number (n) grows the crystal structure tends towards the bulk case.

Figure 1.10 shows results of a molecular structural calculation of the crystal structures for butylammonium methylammonium lead iodide ($\text{BA}_2\text{MA}_{n-1}\text{Pb}_n\text{I}_{3n-1}$, $n = 3$) and 4-aminomethyl piperidinium methyl ammonium lead iodide ($((\text{C}_6\text{N}_2\text{H}_{16}))(\text{CH}_3\text{NH}_3)_{n-1}\text{Pb}_n\text{I}_{3n-1}$),

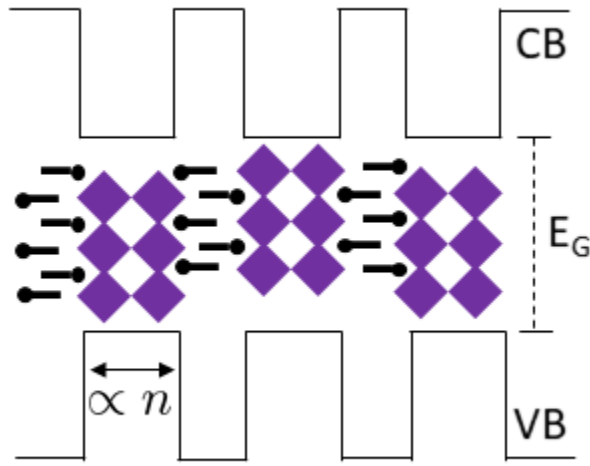


Figure 1.9: Schematic representation of the band edge diagram for the $n = 2$ case of 2D Ruddlesden Popper perovskites. CB-conduction band, VB-valence band, E_G -band gap. The width of the well is directly proportional to the layer number n , the barrier height is determined by the difference between the band gaps of the perovskite and organic spacer semiconductors, while the bandgap is determined by the perovskite material.

adapted from reference [70], hereafter referred to as BA and 4AMP respectively. Figure 1.10 (a) shows the structure for the $n = 3$ case of $\text{BA}_2\text{MA}_{n-1}\text{Pb}_n\text{I}_{3n-1}$. In this case the terminal NH_3 group of the BA spacer molecule occupies a site that would be occupied by a methylammonium cation in the 3D lattice. This functional group forms weak hydrogen bonds with the surrounding iodide atoms, this bonding causes out of plane tilting as well as in plane twisting of the perovskite octahedra. In Figure 1.10 (b) the terminal NH_3 and the aryl NH_2 functional groups of the 4AMP spacer molecule form weak hydrogen bonds with the bridging iodide atoms, indicated by the red dashed lines, this bonding limits the out of plane distortion of the octahedra. Further; this causes the in plane twisting to be in phase inside the octahedral layers, as seen in Figure 1.10 (c). Figure 1.10 also shows the structure of (d) 4-aminomethyl piperidinium and (e) butylammonium. As will be discussed below, the symmetry properties of the BA and 4AMP perovskites have crucial implications for the nature of the Rashba effect in each structure.

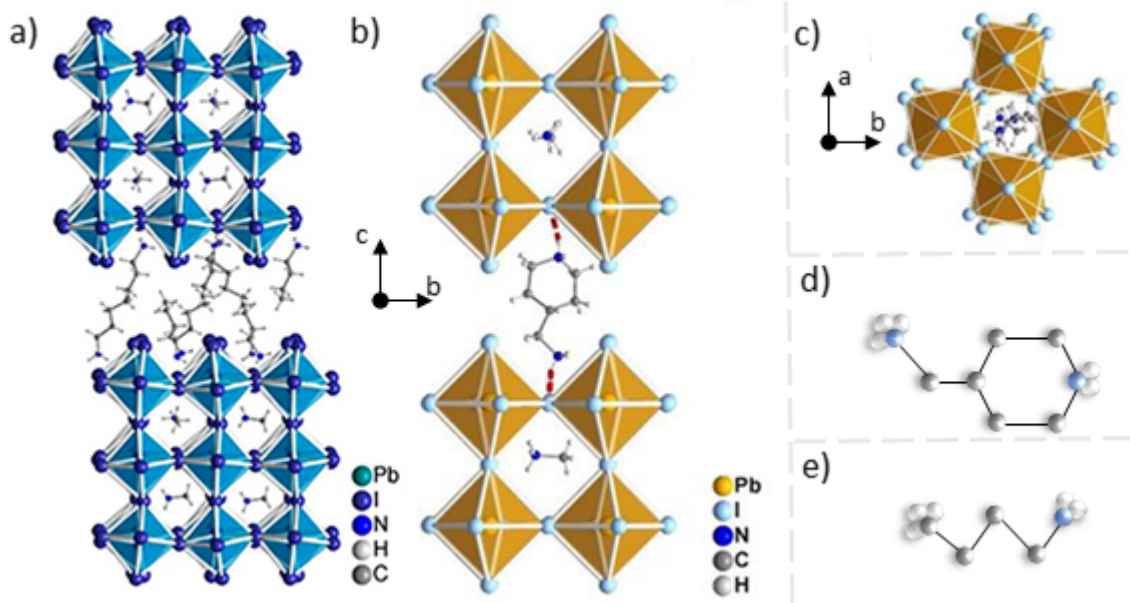


Figure 1.10: (a) Side on view: crystal structure of $BA_2MA_{n-1}Pb_nI_{3n-1}$ ($n = 3$) (b) side on and (c) top down view: crystal structure of $(4AMP)MAPb_2I_7$. Adapted from reference [70]. (d) The structure of 4-aminomethyl piperidinium. (e) The structure of butylammonium.

1.4 Optical Excitation

Optical excitation in a semiconductor occurs when an incident photon, with energy greater than the band gap of the material is absorbed by an electron in the valence band. This sets a limit on the maximum wavelength (or minimum energy) that can be absorbed by a semiconductor, given by:

$$\lambda_{\max} = \frac{hc}{E_G} \quad (1.11)$$

If the energy of the photon is greater than or equal to the band gap, the electron will be promoted to the conduction band, leaving a hole in the valence band. Since the momentum carried by a photon in the visible part of the spectrum is much smaller than the range of carrier momentum shown in an electron band diagram, an optical transition is represented by a vertical arrow (the red arrow in Figure 1.6). In order to determine the allowable energy transitions for an electron in a bulk semiconductor absorbing a photon of energy $E_{ph} = h\nu$, conservation of energy gives:

$$E_2 - E_1 = \frac{\hbar^2 \vec{k}^2}{2m_c} + E_G + \frac{\hbar^2 \vec{k}^2}{2m_v} = h\nu \quad (1.12)$$

where E_1 and E_2 are the initial and final states of the electron in the valence and conduction band respectively. Solving this for \vec{k} gives:

$$\vec{k}^2 = \frac{2m_r}{\hbar^2} \left(\frac{hc}{\lambda} - E_G \right) \quad (1.13)$$

where m_r is known as the reduced mass, given by:

$$\frac{1}{m_r} = \frac{1}{m_c} + \frac{1}{m_v} \quad (1.14)$$

Substituting equation 1.13 into equation 1.4 gives a relation between the energy of the excited electron and the frequency of the incident light.

$$E_2 = E_c + \frac{m_r}{m_c} (h\nu - E_G) \quad (1.15)$$

The density of states with which a photon interacts with an electron in a direct band gap semiconductor is known as the optical joint density of states ($\rho(\nu)$), this can be found through

$$\rho(\nu) = \rho_c(E_2) \frac{dE_2}{d\nu} \quad (1.16)$$

where $\rho_c(E_2)$ is found through equation 1.6 and the derivative is found through equation 1.15, this leads to the optical joint density of states:

$$\rho(\lambda) = \frac{(2m_r)^{3/2}}{\pi\hbar^2} (h\nu - E_g)^{1/2} \quad (1.17)$$

which describes the density of allowable energy excitations for a electron in a bulk semiconductor absorbing a photon of energy $h\nu$. The probability that an electron is absorbed in a semiconductor will be dependent on the fermi-distribution functions in both the conduction (f_c) and valence (f_v) bands. The probability of an electron making the transition from E_1 to E_2 if given by:

$$f_a(\lambda) = [1 - f_c(E_2)] f_v(E_1) \quad (1.18)$$

and the probability of an electron undergoing spontaneous emission from E_2 to E_1 is:

$$f_e(\lambda) = [1 - f_v(E_1)] f_c(E_2) \quad (1.19)$$

The absorption by a semiconductor of photons with wavelength λ can be found by considering the flux passing through a cylindrical region with unit radius and incremental length dz :

$$\frac{d\phi(\lambda)}{dz} = \frac{\lambda^2}{8\pi\tau_r} \rho(\nu) [f_a(\lambda) - f_e(\lambda)] \phi(\lambda) \quad (1.20)$$

Where $\phi(\lambda)$ is the incident flux of wavelength λ and τ_r is the spontaneous lifetime of the final state. Therefore the attenuation of light, or the absorption of light ($\alpha(\lambda)$), through this region of the semiconductor can be written:

$$\alpha(\lambda) = \frac{\lambda^2}{8\pi\tau_r} \rho(\nu) [f_v(E_1) - f_c(E_2)] \quad (1.21)$$

In a weakly excited semiconductor the Fermi-energy level lies within the band gap and the energy levels E_1 and E_2 are at least several times K_bT then the fermi-distribution functions can be approximated as $f_v(E_1) \sim 0$ and $f_c(E_2) \sim 1$ Using the above result one can obtain the absorption coefficient of the semiconductor:

$$\alpha_0(\nu) = \frac{\sqrt{2}m_r^{3/2}}{\tau_r} \left(\frac{c}{h\nu} \right)^2 (h\nu - E_G)^{1/2} \quad (1.22)$$

where τ_r is the lifetime of the final state. Therefore; we expect the absorption above the band gap to follow a square root dependence on the photon energy.

Considering the Coulomb interaction of the electron and hole, these pairs can bind together forming a quasi-particle known as an exciton. Excitons can be modelled as a hydrogenic atom, with a lower binding energy (due to the screening effects of nearby electrons and holes). As a result, a series of bound states exists corresponding to transition energies slightly lower than the band gap of the semiconductor. This is represented in Figure 1.6 as a series of smaller discrete levels below the conduction band. In addition to bound states below the gap, the Coulomb interaction also enhances the absorption near the band edge by a process known as Sommerfeld enhancement [71]. These effects are shown qualitatively as a red curve in Figure 1.11 (a).

Contrast this with the expected absorption from a quantum well possessing discrete energy levels. In this case, the absorption spectra will be modified by the change in the density of states for a 2D confined structure. Counting the number of electrons that fill a circle of radius k in the lowest energy state:

$$N = \frac{L^2 m^*}{\pi \hbar^2} E \quad (1.23)$$

the density of states in this region can be found through:

$$\frac{dN}{dE} = \frac{L^2 m^*}{\pi \hbar^2} \quad (1.24)$$

which is constant with energy. The total density of states is found by multiplying this constant by the energy of the subband in question E_c , this gives:

$$\rho_{2D}(E) = \frac{L^2 m^*}{\pi \hbar^2} \sum_{nz} \Theta(h\nu - E_c) \quad (1.25)$$

where Θ is the Heaviside step function. The corresponding linear absorption spectrum is given by:

$$\alpha_0(\nu) \propto \frac{(h\nu - E_G)^{1/2}}{(h\nu)^2} \Theta(h\nu - E_c) \quad (1.26)$$

This absorption is represented as the dashed curve in Figure 1.11 (b). Excitonic and Sommerfeld enhancement applies to each subband in the quantum well, as is represented schematically by the red curve in Figure 1.11 (b).

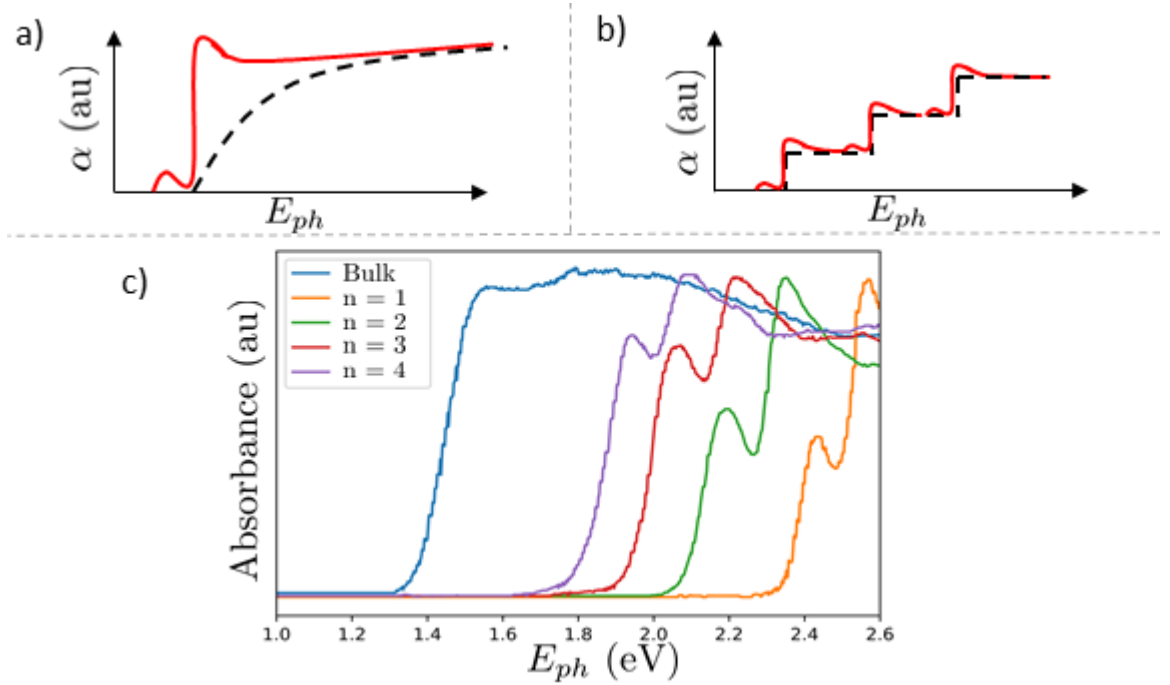


Figure 1.11: Schematic representation of the absorption spectrum, without (dashed lines), and with (red lines) excitonic and Sommerfeld enhancement effects for (a) a bulk semiconductor and (b) a quantum well. (c) Measured linear absorption of $\text{BA}_2\text{MA}_{n-1}\text{Pb}_n\text{I}_{3n-1}$ ($n = 1-4$) and bulk MAPbI_3 , adapted from reference [72].

Figure 1.11 (c) shows the measured absorption spectra for MAPbI_3 and $\text{BA}_2\text{MA}_{n-1}\text{Pb}_n\text{I}_{3n-1}$ ($n = 1-4$). In the bulk case (blue curve) there is a sharp onset to the band edge reflecting the strong Sommerfeld enhancement. The exciton binding energy in the bulk

perovskite has been found to be ~ 15 meV [73]. As a result, the exciton resonance is not apparent in the absorption curve for bulk MAPbI₃. In contrast, the confined absorption spectra of the BA₂MA_{n-1}Pb_nI_{3n-1} structures show a strong blue shift in the band gap with decreasing n-value. This observation is consistent with equation 1.9 as the length of the well is dictated by the layer number n: for decreasing n, equation 1.9 predicts an increase in the allowed energy levels. Furthermore, the excitonic effects are noticeable at energies just below the main absorption peak. This reflects the increase in binding energy with increasing degree of confinement. These trends are consistent with the picture laid out in Figure 1.11 (b).

1.5 Dynamic Processes in Semiconductors

Once an electron-hole pair has been formed through optical excitation with a laser source, these carrier will undergo transport, relaxation and recombination processes. Transport and relaxation processes are intraband processes, meaning they occur strictly within the conduction or valence bands, whereas recombination processes are interband, meaning they occur between the conduction and valence bands. When a carrier is first excited into the conduction band, it will be in a coherent superposition of the initial and final states of the transition. In other words, the electron-hole pair is an oscillating dipole and the phase of this dipole will be determined by the light field that excited it. The lifetime of this superposition is known as the dephasing time, and is typically sub picosecond. This timescale is dictated by incoherent (phase breaking) intraband processes such as carrier-carrier scattering, which destroy the phase relationship between the excitation pulse and the superposition. Once the dephasing time has passed, the carriers will be in a so called “hot” distribution with an energetic profile described by a Fermi distribution. The Fermi temperature and spread of kinetic energies is dictated by the centre photon energy and spectral width of the laser pulse used to excite the electron-hole pairs respectively. As the carriers continue to exchange energy with the lattice, the temperature of the distribution will reach a thermal equilibrium with the lattice. In typical inorganic semiconductors this occurs on a picosecond time scale.

During the time a carrier is in the conduction band it can undergo transport processes which move carriers through the crystal. These processes are dictated by

the carrier's mobility, denoted μ , which can differ for electrons and holes. The carrier mobility depends on the carrier effective mass and is a measure of how easily a carrier can propagate through the solid. The distance a carrier can move through a crystal before recombination occurs is known as the diffusion length (L_D). The relationship between the diffusion length, carrier lifetime, and the temperature (T) is:

$$L_D = \sqrt{\tau \frac{K_B T \mu}{e}} \quad (1.27)$$

where e is the fundamental charge and K_B is the Boltzmann constant.

Once the Fermi distribution has reached thermal equilibrium with the lattice, the interband transitions begin. In these processes electrons and holes recombine and lose their energy either to the lattice or through the emission of a photon. The time it takes for the electrons to relax down to the valence band is called the recombination time.

1.5.1 Ultrafast Probes of Carrier Dynamics

To study carrier and spin dynamics in semiconductors, a common ultrafast technique known as differential transmission is utilized. In the most basic case, an ultrafast laser pulse is split into two pulses, known as the pump and probe. The probe is kept much weaker ($\leq 10\times$) than the pump. The probe pulse is mechanically delayed from the pump pulse by a time τ , shown schematically in Figure 1.12 (a). The pulse is absorbed by electrons in the semiconductor which make vertical transitions to the conduction band. This creates a distribution of electrons in the conduction band of the semiconductor and a distribution of holes in the valence band. This distribution modifies the absorption coefficient of the semiconductor. This change in absorption can be expressed as:

$$\Delta\alpha = (1 - f_e - f_h) \alpha_0(\nu) \quad (1.28)$$

where f_e (f_h) is the distribution function for the electron (holes) in the conduction (valence) band. This excitation is shown in Figure 1.12 (b). Figure 1.12 (c) shows the system at a later time τ . The incident probe pulse is not absorbed as it cannot excite carriers into the filled states. Therefore; a measure of a change in the intensity of the probe pulse, between when the pump is present versus absent, will give a

measure of the absorption of the sample at that energy and delay time. A high probe signal indicates that there is low absorption and therefore a high carrier occupation, while a low probe signal indicates that there is high absorption and therefore a low carrier population. By measuring the change in transmission of the probe pulse as a function of the time delay between pulses, the change in absorption related to carrier occupation at the photon energy of the probe pulse can be measured. This is typically presented as $\frac{T-T_0}{T_0}$, where T (T_0) is the transmission of the probe beam in the presence (absence) of the pump beam. The number of carriers at the energy of the probe pulse will decay with time following excitation due to both intraband thermalization and interband recombination since both processes take carriers out of the optically coupled region of the band structure. With an initial population of electron-hole pairs N_0 , the signal will decay according to:

$$T - T_0 = \Delta T \propto N_0 (e^{-t/\tau} + e^{-t/\tau_{th}}) \quad (1.29)$$

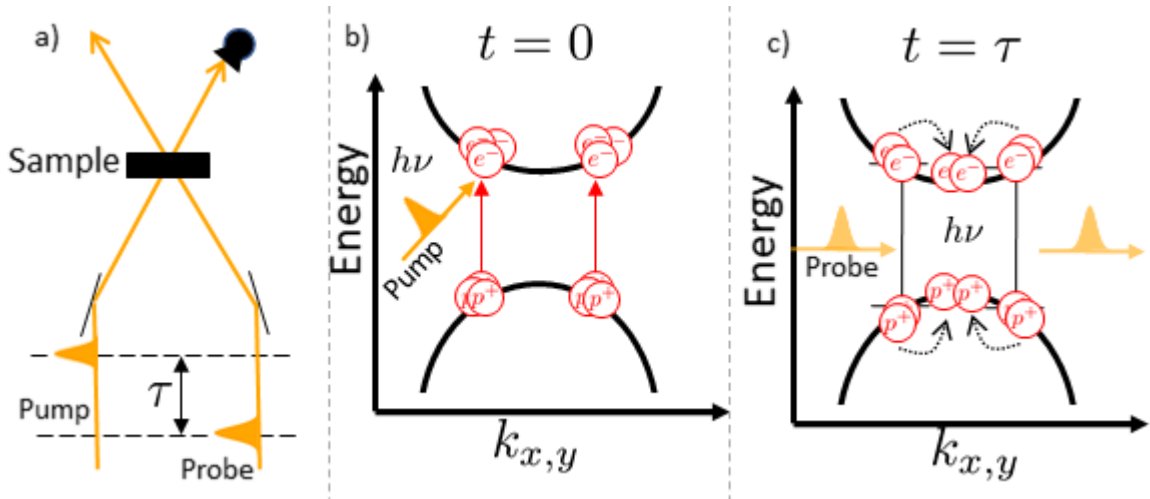


Figure 1.12: (a) Schematic representation of a differential transmission setup. The pump and probe beams are both incident at the same spot on the sample, the probe pulse is mechanically delayed with respect to the pump by a time τ . (b) Excitation of a semiconductor by the pump pulse. The pulse excites a carrier distribution into the conduction band at the energy of the pump pulse. This distribution will relax over time. (c) After a time τ the probe pulse is incident on the sample. The transmission of the probe will depend on the availability of states in the conduction band corresponding to the energy of the probe pulse.

Due to the optical selection rules (discussed in detail in section 2.1.2), using circularly polarized pump and probe pulses, the spin state of the carriers may also be probed as a function of delay time following optical excitation by the pump pulse. By measuring the change in transmission of the probe pulse with the same or opposite helicity, the occupation of the same or opposite spin states can be inferred by considering a quantity known as the degree of spin polarization, defined as:

$$P = \frac{(N^+ - N^-)}{(N^+ + N^-)} \quad (1.30)$$

where N^+ (N^-) is the population of electrons with the same (opposite) spin state associated with the circular pump beam. The rates of change of these populations can be expressed as:

$$\frac{d}{dt}N^+ = -\frac{N^+}{\tau} - \frac{N^+}{s} + \frac{N^-}{s} \quad (1.31)$$

$$\frac{d}{dt}N^- = -\frac{N^-}{\tau} - \frac{N^-}{s} + \frac{N^+}{s} \quad (1.32)$$

where τ is the carrier recombination time, and s is the spin relaxation time. The addition and subtraction of equation 1.31 and 1.32 leads to:

$$\frac{d}{dt}(N^+ + N^-) = -(N^+ + N^-) \left(\frac{1}{\tau} \right) \quad (1.33)$$

$$\frac{d}{dt}(N^+ - N^-) = -(N^+ - N^-) \left(\frac{1}{\tau} + \frac{2}{s} \right) \quad (1.34)$$

Which can be integrated to find:

$$(N^+ + N^-) = N_0 e^{-\frac{t}{\tau}} \quad (1.35)$$

$$(N^+ - N^-) = N_0 e^{-t(1/\tau + 2t/s)} \quad (1.36)$$

Equation 1.35 shows that the rate at which the total population decays is dependent on the carrier recombination time, while equation 1.36 shows that the difference in spin polarization is dependent on both the carrier recombination time and the spin lifetime. Dividing equation 1.36 by equation 1.35 gives an expression for the degree of spin polarization, of an initial distribution P_0 , as a function of time, independent of carrier recombination time.

$$P(t) = \frac{(N^+ - N^-)}{(N^+ + N^-)} = P_0 e^{-2t/s} \quad (1.37)$$

1.6 Rashba Effect in Semiconductors

As discussed in section 1.1, the spin-orbit interaction leads to an effective magnetic field ($\mathbf{\Omega}(\vec{k})$) dependent on the electron momentum (*i.e.* wavevector \vec{k}). This effective magnetic field determines the spin-quantization axis as well as the energetic splitting between spin states at each \vec{k} . To gain insight into this effect, it is instructive to consider the case where the symmetry breaking direction is perpendicular to the two dimensional plane of transport of electrons. This would describe for example the case of an applied electric field using a gate electrode across a semiconductor quantum well. This geometry was first analysed by Bychkov and Rashba [25]. One can show using a perturbative $\mathbf{k} \cdot \mathbf{P}$ approach that the spin orbit interaction in this case leads the perturbative Rashba hamiltonian:

$$\mathbf{H}_R = \mathbf{\Omega}(\vec{k}) \cdot \sigma \quad (1.38)$$

Here σ are the Pauli spin matrices and $\vec{k} = k_x \vec{x} + k_y \vec{y}$ is taken to be in the x - y plane where \vec{z} is the stacking direction of the quantum well. Given that $\mathbf{\Omega} \propto \nabla V \times \mathbf{k}$, with ∇V in the \vec{z} direction and \vec{k} in the x - y plane, $\mathbf{\Omega}$ will be in the x, y plane, perpendicular to \vec{k} . Keeping terms that are linear in \mathbf{k} , the above result may be written in the form:

$$\mathbf{H}_R = \lambda_R (k_x \sigma_x - k_y \sigma_y) \quad (1.39)$$

where the eigenstates are given by:

$$E_{\pm} = \frac{\hbar^2 \mathbf{k}^2}{2m_e} \pm \lambda_R |\mathbf{k}| \quad (1.40)$$

The Rashba coefficient (λ_R) is given in terms of the energy splitting between the two eigenstates at the minimum of the lower band $\lambda_R = \Delta E / |k_R|$ ($\Delta E = E_+ - E_-$). Figure 1.13 (a) shows the Rashba dispersion relation, indicating ΔE and $|k_R|$. Figure 1.13 (b) shows the direction of the effective magnetic field with respect to the electron wavevector.

1.7 Literature Review

1.7.1 Perovskite Photovoltaics

Photo-voltaics utilizing perovskites have shown remarkable ability to combine low-cost fabrication techniques such as spin coating [74], blade coating [75], and spray

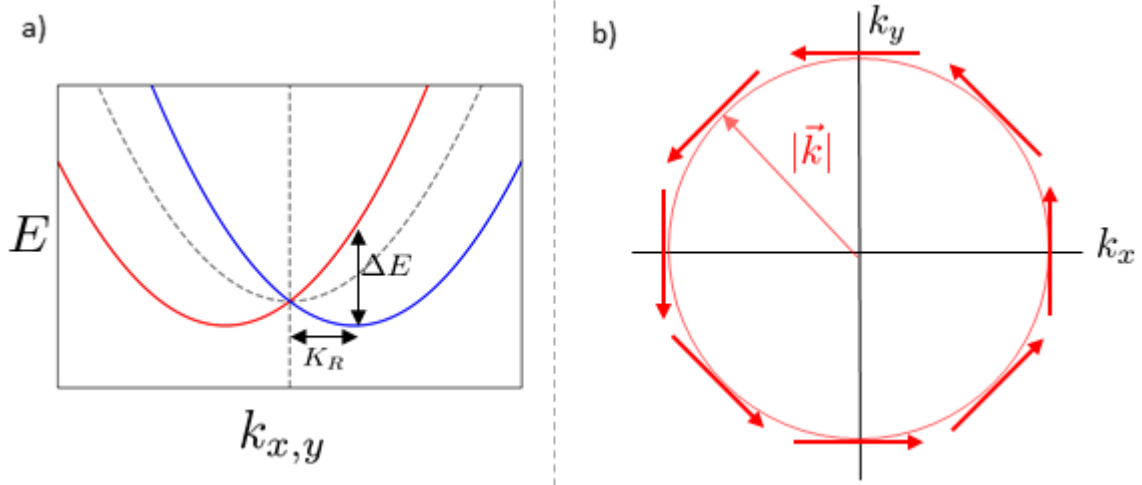


Figure 1.13: Dispersion relation for the Rashba Hamiltonian. The dotted parabola represents the unperturbed eigenstates, the red (blue) lines represent the + (-) Rashba energy eigenstates. Here the Rashba coefficient is defined as $\lambda_R = \Delta E/|k|$. (b) The Rashba effective magnetic field for a confined 2D electron gas with ∇V perpendicular to the plane of the 2D electron gas.

coating [76], with high power conversion efficiencies. In 2009 a group from the University of Tokyo, led by Professor Miyasaka, were the first to incorporate a perovskite as the absorbing layer of a solar cell. This perovskite was methylammonium lead iodide (MAPbI_3), which originally gained notoriety due to its high absorption in the solar spectrum [8]. Although this device achieved modest power conversion efficiencies ($\sim 3.8\%$) [3] methylammonium lead iodide continues to be at the forefront of perovskite photo-voltaics. Today the power conversion efficiencies of photo-voltaics incorporating methylammonium lead iodide have reached 22.1% [77]. This achievement was brought about through countless research groups competing to obtain a more efficient cell. Some major advancements in this field include: (i) the chemical engineering of the hole-transport material [78, 79], (ii) development of methods to control the morphology of the perovskite layer [80], and (iii) the deposition methods for the perovskite layer [3, 74, 81–84].

In addition to the demand for high power conversion efficiency there are two main obstacles for perovskites to overcome before widespread acceptance can occur: the presence of lead in the lattice, as well as the stability of the photo-voltaic devices.

The former issue is being tackled by many groups and is primarily being accomplished through the substitution of other group IV elements, such as tin, for the lead halide [85]. The latter issue occurs due to perovskites degradation due to interactions with other device layers, and exposure to moisture, heat, and light. Exposure to these variables either during fabrication or operation can lead to decreases in power conversion efficiency over time [52]. In 2014 Smith *et.al.* had success in increasing the moisture stability of their cells using a new family of perovskite known as Ruddlesden Popper perovskites (also known as 2D perovskites) [53].

1.7.2 2D Perovskite

Density functional theory has shown that the optical transitions in 2D perovskites are direct [48,86], confirmed by the steep onset in the linear absorption spectrum [8,47,86]. Kanatzidis' *et.al.* found that quantum confinement blue shifts the bandgap with decreasing layer number and creates discrete energetic transitions, both noticeable in the absorption spectra [87] (see Figure 1.11 (c)). Blancon *et.al.* found that the exciton binding energy and optical bandgap decreased with increasing layer number [86]. These observations are consistent with the quantum well model laid out in section 1.2.1.

The first photo-voltaic cells based on 2D perovskites were demonstrated in 2014 with a power conversion efficiency of 4.7% using $(\text{PEA})_2(\text{MA})_2\text{Pb}_3\text{I}_7$ (known simply as PEA) [53]. This device showed little changes in XRD or optical absorption after 46 days in 52% humidity. In 2015 Kanatzidis *et.al.* reported the first photo-voltaic devices using $\text{BA}_2\text{MA}_{n-1}\text{Pb}_n\text{I}_{3n-1}$ perovskites [87]. The authors found that for $n \leq 2$ the perovskites exhibited strong photoluminescence at room temperature, implying they would be suitable for use in LED's. For $n > 2$, they found that the perovskites exhibited strong absorption in the visible spectrum, indicating they would be suitable for photo-voltaic applications. By fine tuning the perovskite layer thickness, they were able to achieve devices with power conversion efficiency of 4.02%, in the $n = 3$ case. In a later report, Tsai *et.al.* showed that by orienting the wells perpendicular to the substrate, power conversion efficiencies of 12.52% can be achieved using the $n=3$ and $n=4$ 2D structures [51]. This is due to the alignment of the two dimensional charge transport direction of the quantum well with the charge collection of the solar cell.

Tsai *et.al.* found 3D perovskites photo-voltaics degrade to 40% of their initial power conversion efficiency in the first 24 hours, followed by a slow falloff down to <10% after 94 days, while 2D perovskite photo-voltaics retained 80% of its original power conversion efficiency after 200 hours and slowly degraded to about 70% after 94 days (both in 65% humidity) [51]. These studies illustrate the increased stability of 2D perovskites over their bulk counterparts. However; the power conversion efficiency of solar cell using these materials has only reached half of the bulk photo-voltaic devices. A comprehensive study of the charge transport properties of these materials is necessary to understand where the loss in power conversion efficiency occurs.

Using differential transmission to study carrier lifetimes and diffusion lengths in PEA, Milot *et.al.* [88] found that diffusion length increased for increasing layer number, and actually exceeded that of MAPbI₃ for $n = 3$. XRD analysis revealed that the $n=3$ layer preferentially oriented itself perpendicular to the substrate while the $n < 2$ cases oriented parallel. These results go a long way to explaining why both Kanatzidis and Tsai found the $n \geq 3$ based solar cells to have the highest power conversion efficiency. In 2017 Grozema *et.al.* used a combination of microwave conductivity and photoluminescence measurements to measure the mobility of carriers for various n values in BA₂MA _{$n-1$} Pb _{n} I _{$3n-1$} [89]. They found that the mobility of carrier increases with increasing layer number, and depends strongly on temperature. The authors attributed the increase in mobility to a decrease in exciton binding energy (~ 370 meV for $n = 1$, ~ 80 meV for $n = 4$). The observation of free carriers for $n > 3$ further explains why solar cells based on those cases attain the highest power conversion efficiencies. Despite these advances, the fundamental properties of the 2D perovskites are still not well understood. The experiments in this thesis work, which provide information on the carrier relaxation and spin dynamics, will further advance this fundamental knowledge.

1.7.3 Spin-Orbit Coupling in Perovskite Materials

Early electronic structure calculations for both 3D [90] and 2D perovskites [70] indicate that the strong spin orbit coupling in this material, due to heavy lead and iodine atoms in the lattice, has a strong impact on band structure. In 2003 Umebayashi *et.al.* highlighted the importance of spin-orbit effects to perovskite structures [90]. Using

a combination of ultraviolet photoelectron spectroscopy and linear combination of atomic orbital calculations, the authors showed that the valence band consists of lead 6s and iodide 5p orbitals while the conduction band consists of lead 6p and iodide 5s orbitals. This was confirmed by Even *et.al.* in 2013 for 3 dimensional perovskite structures [47,48]. Further, Even *et.al.* showed that the direct transitions in MAPbI₃ corresponded to transitions between a single degenerate valence band and a split-off band in the triply degenerate conduction band. Figure 1.14 shows the results of these calculations, adapted from reference [48]. The initial calculations incorporating spin-orbit coupling in perovskite assumed a perfectly symmetric octahedra. It was later found, through comparison of XRD and molecular structure calculations [46], that bulk and 2D perovskites octahedra have both static (such as tilting and twisting of the octahedra) and dynamic (such as rotations of the methylammonium cation) distortions. These distortions to the idealized structure bring about molecular dipoles, which are expressed in the crystal structure as bulk inversion asymmetry and give rise to the Rashba effect.

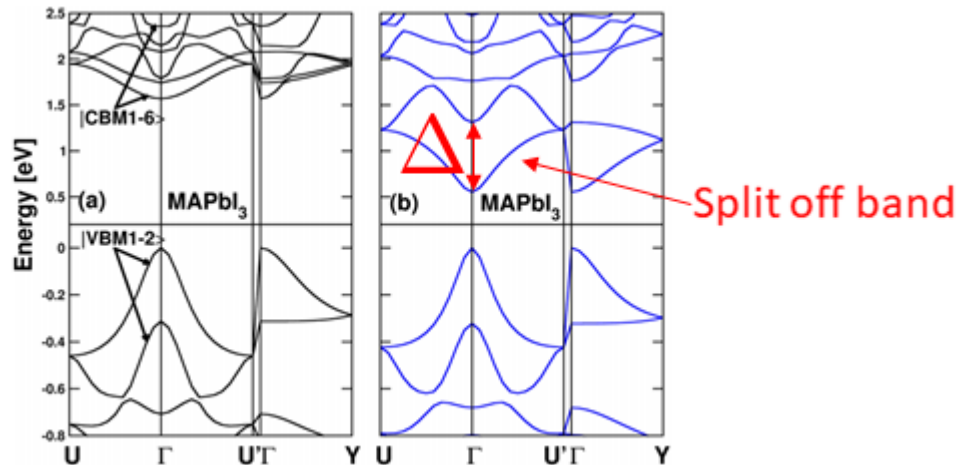


Figure 1.14: Calculated band structure for MAPbI₃(a) without and (b) with the effect of SOC. The effect of SOC is to split the conduction band into a split off band, and a triply degenerate band. Further; SOC lowers the band gap energy. adapted from reference [47]

The Rashba splitting in the band structure in perovskites has been the focus of numerous theoretical studies in recent years [49,91,92]. Calculations by Kepenekian *et.al.* revealed an extremely large Rashba coefficient in MAPbI₃, with a value of

$\lambda_R = 3.76$ (3.71) $\text{eV}\cdot\text{\AA}$ at the edge of the conduction (valence) band [92]. This was comparable to the record Rashba splitting observed in BiTeI [93]. Even *et.al.* calculated the Rashba coefficient for various 2 and 3 dimensional perovskite systems and found that the Rashba coefficient to be dependent on the temperature and phase of the crystal. Further; Even showed that the Rashba coefficient can be tuned through an external electric field, making the case for perovskites use in spin-transistors [92]. In 2016 Neaton *et.al.* demonstrated that the Rashba splitting (in APbX_3 ; $\text{A} = \text{CH}_3\text{NH}_3^+$, $\text{CH}(\text{NH}_2)_2^+$, Cs^+ , $\text{X} = \text{I,Br}$) can be controlled via chemical substitution of the larger cation in the perovskite lattice [49]. The authors further noted that the Rashba coefficient could be controlled via mechanical strain to the lattice, or via applied electric fields, confirming the earlier assertion by Even *et.al.*

In 2014 Kim *et.al.* used a tight binding approach to show the Rashba effect results in a mismatch between the spin states in the conduction band minimum and the valence band maximum, where the strength of this mismatch is characterized by the Rashba coefficient [91]. Following on the work by Kim *et.al.* in 2015 Zheng *et.al.* was able to show that the mismatch in spin states lead to spin-forbidden recombination dynamics at the band edge [46]. This mechanism allows perovskites to act as a direct band gap upon excitation and an indirect band gap upon recombination. This offers a intrinsic mechanism for explaining the long carrier lifetimes observed in MAPbI_3 [94–97]. The exotic spin properties observed in these calculations are typically expected in material with inversion asymmetries. However; in 2016 Etienne *et.al.* showed that regardless of the symmetry of the crystal these characteristics can arise from the rotational degrees of freedom associated with the methylammonium cation (in MAPbI_3) [50]. These reports demonstrate the important role that spin-orbit coupling and the Rashba effect have on the carrier dynamics of perovskite systems.

In 2016 Nieser *et.al.* made the first measurements of Rashba splitting in a perovskite system using spin and angle-resolved photoemission spectroscopy, revealing a giant Rashba coefficient with $\lambda_R = 7 \pm 1 \text{ eV}\cdot\text{\AA}$ [98]. Figure 1.15 (a) shows the results of this work. In 2017 Vardeny *et.al.* used a combination of density functional theory, transient absorption spectrometry, electrical absorption spectrometry, and transient photomodulation to measure the Rashba energy splitting and Rashba coefficient in $(\text{C}_6\text{H}_5\text{C}_2\text{H}_4\text{NH}_3)_2\text{PbI}_4$ (PEPI), a layered perovskite with $n = 1$. The authors were

able to estimate the Rashba splitting as (40 ± 5) meV [43]. Figure 1.15 (b) shows some of the results of these measurements.

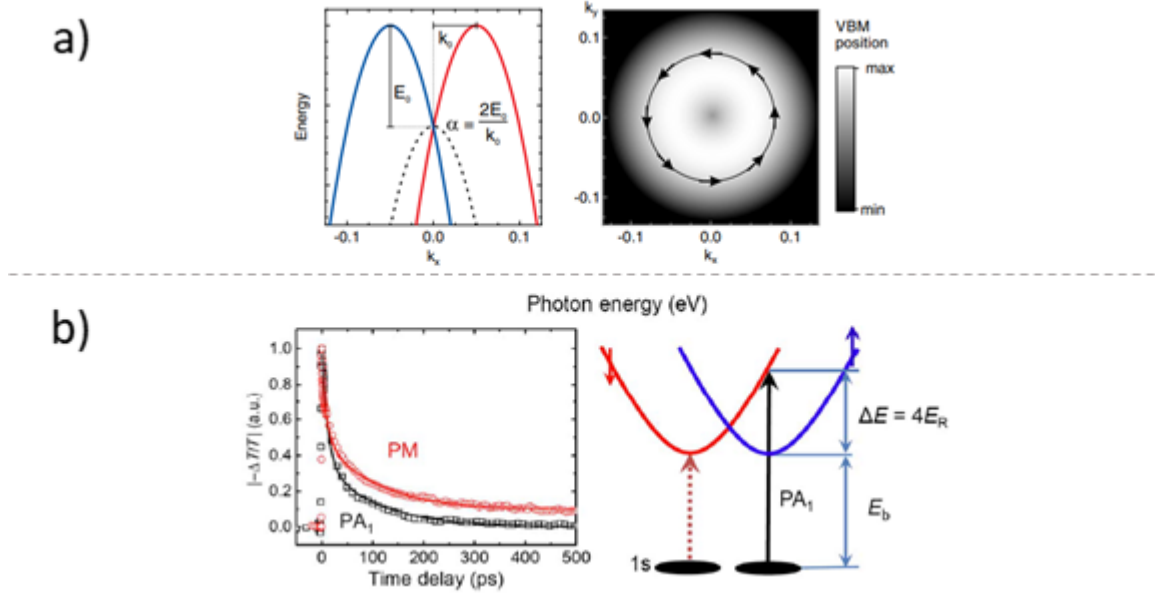


Figure 1.15: (a) Measured Rashba splitting for MAPbBr_3 adopted from reference [98]. The blue and green curve measure the dispersion of differing spin states. (b) Measured Rashba splitting for PEPI, adapted from [43]. Reprinted with permission from AAAS. The red and black curves indicate the relaxation through the two pathways shows graphically beside.

1.7.4 Spin-Dynamics in Perovskite Materials

In 2015 Giovanni *et.al.* became the first group to measure spin dynamics in perovskite materials [42]. Here the authors used circular dichroism to measure the spin lifetime as a function of incident power and temperature in MAPbI_3 . The authors found spin lifetimes for electrons (holes) on the order of pico (sub-pico) seconds, and noticed a decrease in spin lifetime as a function of fluence as well as temperature (from 77-300 K). This prompted the authors to attribute the Elliot-Yafet (EY) mechanism as the primary spin-relaxation pathway (in the EY mechanism a spin flip occurs as the result of a momentum scattering event, this process is described in detail in section 2.2.2). Concurrently Zhai *et.al.* used magnetic field-induced circularly polarized photoluminescence to measure spin dynamics in $\text{MAPbI}_{3-x}\text{Cl}_x$ thin films [43]. By careful measurement of the relationship between the spin injection, applied magnetic

field, and temperature the authors were able to estimate the spin lifetimes to be 80 ps at 18 K, comparable to some III-V systems [99]. In 2017 Odenthal *et.al.* use time-resolved Faraday rotation to measure spin relaxation in $\text{MAPbI}_{3-x}\text{Cl}_x$ films [44]. The authors found spin lifetimes to decrease with increasing temperature, contrary to Giovanni *et.al.*'s findings, and to exceed 1 ns at 4 K. This discrepancy could be attributed to the influence of the lighter chlorine atoms on the SOC. In any event the vast spread of values of the spin lifetimes highlight the the importance for further studies of the spin dynamics in these materials.

To the authors knowledge there have only been two experimental reports indicating spin dynamics in 2D perovskite systems. In 2018 Sum *et.al.* measured spin dynamics in PEPI using circular dichroism [43]. The authors observed sub-pico second spin lifetimes and attributed the relaxation mechanism to spin-flip via the Columb exchange. The final report, published in 2018, by Todd *et.al.* measure the spin lifetime using the same setup as described in Chapter 3. Figure 1.16 shows their results for spin lifetimes measured as a function of laser detuning and fluence. The decrease in spin lifetime with laser detuning (Figure 1.16 (a)) and the increase in spin lifetime with fluence (Figure 1.16 (b)) indicate that precessional spin relaxation has a significant effect on spin dynamics in this material. This led the authors to attribute the D'Yakanov Perel (DP) (see section 2.2.3 for a detailed description) mechanism as the primary relaxation pathway in this system, and to find a Rashba spin splitting of 10 meV for a 50 meV above gap excitation [45].

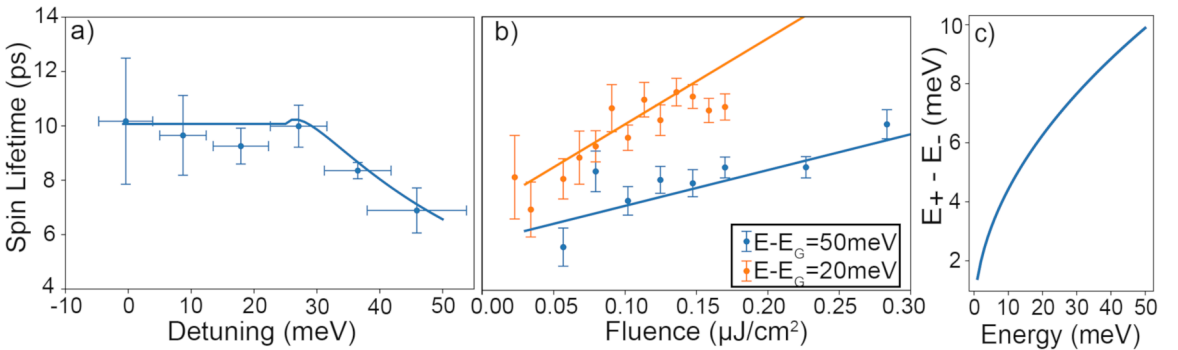


Figure 1.16: Measured spin lifetimes in $\text{BA}_2\text{MAPb}_2\text{I}_7$ as a function of (a) laser detuning and (b) laser fluence. Solid lines show the results of the carrier spin dynamics fit with the Rashba coefficient as the only fitting parameter. (c) Calculated spin splitting taken with the optimal parameter from (b). Adapted from reference [45]

1.7.5 Spintronic Applications of Perovskite Materials

In 2017, Vardeny *et.al.* demonstrated two optoelectronic-spintronic devices utilizing perovskite as the optoelectronic component and a CoFeB/MgO/CoFe stack as the magnetic tunnelling junction [100]. Figure 1.17 shows schematics of the two devices made. In Figure 1.17 (a) the perovskite photo-voltaic cell is used to create photocurrent. This photocurrent influences the conductivity of the magnetic tunnelling junction. This represents a unique way to modulate the spin-valve performance with an external light source, serving as a prototype for a photon-to-spin transducer. Figure 1.17 (b) shows a schematic for a magnetic field controlled light emitting diode. Here the perovskite stack acts as the diode where the injection of carriers into the perovskite is controlled by a magnetic tunnelling junction. This spin-dependent electroluminescence modifies the output wavelength of the light, in this case from green to red. These initial demonstrations of spintronic devices using perovskites, together with the above described studies indicating strong spin orbit coupling, are promising for the prospect of the development of a broad range of spintronic devices using perovskite materials.

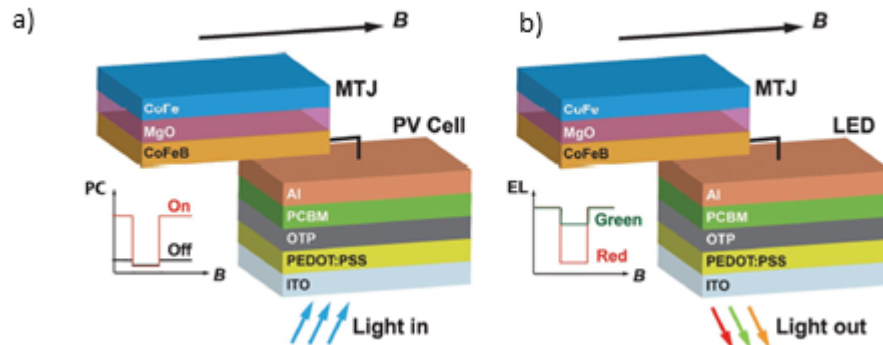


Figure 1.17: Schematics of a optoelectronic-spintronic devices from Vardeny *et.al.* [100]. (a) a prototype for mosulating spin-valve performance with an external light source. (b) a prototype for spin-dependent electroluminescence.

1.8 Outline of Thesis

Chapter 2 will outline the theoretical underpinnings necessary to the understanding of the experimental explorations. Section 2.1 will outline the key points leading to the

optical selection rules in perovskite materials. Section 2.2 will explain the differing spin relaxation mechanisms in semiconductors. Section 2.3 will outline how bulk and structural inversion asymmetry affects the spin dynamics in III-V and perovskite systems. Chapter 3 gives an overview of the experimental techniques used. Section 3.1 gives an explanation of the methods used to fabricate the samples studied. Section 3.2 and section 3.3 will give an overview of the experiments used to characterize the samples. Section 3.4 gives a description of the ultrafast laser source used. Finally section 3.5 describes the ultrafast spectroscopic techniques used to study the 4AMP perovskite in this thesis work. Chapter 4 presents the experimental results which indicate a reduced role played by precessional spin relaxation in 4AMP relative to BA systems studied previously [45, 54]. This is attributed to direction of the symmetry breaking in these two materials and is promising for the development of a spin field effect transistor and spin filters using this material. Chapter 5 will present the conclusions drawn by the author, as well as a description of possible future work in this area.

Chapter 2

Theoretical Considerations

2.1 Optical Selection Rules

Allowed optical transitions are those that conserve energy and angular momentum between the incident photon and the electron that transitions between the valence and conduction band. These allowed transitions are described by the optical selection rules. These depend on the nature of the incident light field and the nature of the optical transition. For example, a circularly polarized photon will carry angular momentum of $\pm\hbar$, which is transferred to the electron-hole pair upon excitation. For simplicity we will consider only vertical transitions in direct band gap semiconductors.

2.1.1 Electronic Structure of Semiconductors Including Spin-Orbit Coupling

To understand the optical selection rules of a semiconductor the effects of intrinsic angular momentum, or spin, must be taken into account. Blind application of Pauli's exclusion principle would assume that the number of available states doubles. However; the most interesting elements are missed. As a result of the spin-orbit interaction, given in equation 1.1, each of the bands in a semiconductor corresponds to an eigenstate of total angular momentum \mathbf{J} ($\mathbf{J} = \mathbf{S} + \mathbf{L}$), where \mathbf{S} is the spin angular momentum and \mathbf{L} is the orbital angular momentum. Before considering the band structure of perovskite, it is instructive to consider the simpler case of a III-V semiconductor. Figure 2.1 shows the (a) crystal and (b) band structure of GaAs. In GaAs, the cell function $U_{\nu\vec{k}}(\vec{R})$ for the conduction band is "s-like" and for the valence band is "p-like". Each band corresponds to a particular eigenstate of the total angular momentum, which are denoted here by $|j, m_j\rangle$. The conduction band is characterized by $l = 0$ ($|1/2, 1/2\rangle$). The valence band is characterized by $l = 1$ where the $j = 1/2$ and $j = 3/2$ states are separated by an energetic splitting of Δ called

the spin-orbit splitting energy. The $|1/2, \pm 1/2\rangle$ band is known as the split-off band. The $j = 3/2$ band is further split into the light ($J_z = \pm 1/2$) and heavy ($J_z = \pm 3/2$) hole bands, which are degenerate at the zone center but split away from $\vec{k} = 0$.

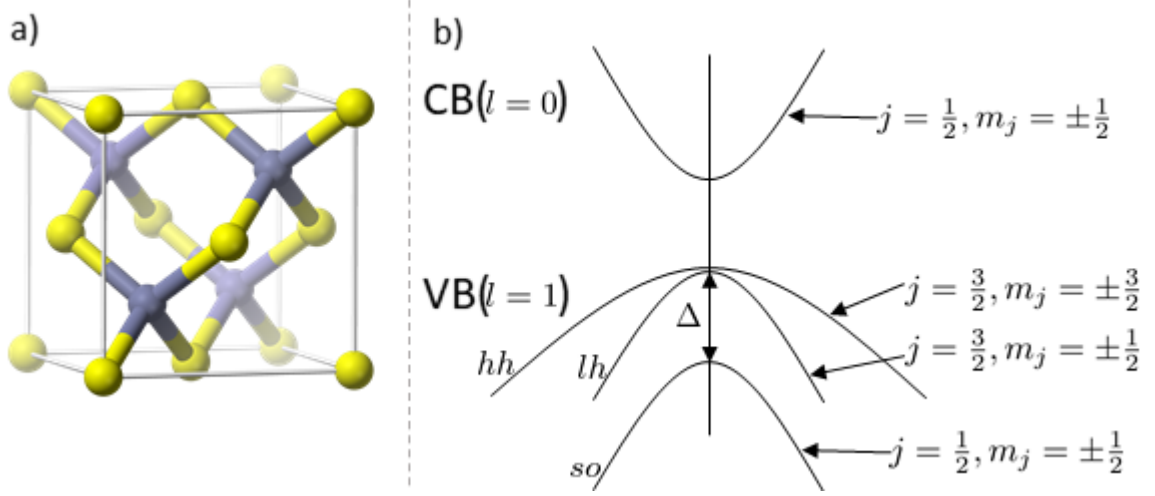


Figure 2.1: (a) Crystals structure of GaAs, consisting of two face-centred cubic lattices offset by $[\frac{1}{4}, \frac{1}{4}, \frac{1}{4}]$. (b) The band structure of GaAs near the zone center including the effects of spin-orbit coupling. Here the conduction band is “s-like” while the valence band is “p-like”. This leads to splitting in the valence band into the light hole (lh) and heavy hole (hh) bands. VB - valence band. CB - conduction band.

Figure 2.2 shows the calculated band structure of $([C_5H_{11}NH_3]PbI_4)$ a RP perovskite with 1 octahedral between spacer layers, (a) without and (b) with the spin-orbit coupling included, adapted from referece [48] by Even *et.al*. Contrary to GaAs, Evan *et.al*. found that the lead 6s electrons form the valence band while the iodide 5p electrons form the conduction band. Therefore the conduction band cell functions has p-symmetry, while the valence band has s-symmetry. Since GaAs and related III-V materials represent the prototypical system, the band edges in perovskites are referred to as “reversed”. The red double headed arrow indicates the splitting between the split-off band, with $j = 1/2$, and the other two conduction bands, with $j = 3/2$, caused by the spin-orbit interaction. Due to the large spin orbit splitting ($\sim 1eV$ [48, 101]) in perovskites the lowest energy transition will be between the “s-like” ($l = 0, j = 1/2$) valence band and the “p-like” ($l = 1, j = 1/2$) conduction band. Figure 2.2 (c) shows the calculated band structure for $(4AMP)MAPb_2I_7$,

adapted from reference [70] by Kanatzidis *et.al.* In addition to the inducing the spin-orbit splitting, the spin-orbit coupling effect further alters the electronic properties by pushing the conduction band downwards, lowering the band gap energy. These results illustrate the importance of including spin-orbit coupling effects when considering the electronic structure of 2D perovskite materials. The spin-orbit splitting Δ is much larger in perovskites than in GaAs. (Δ was calculated to be 1.2 eV in $[\text{C}_5\text{H}_{11}\text{NH}_3]\text{PbI}_4$ [48] compared to 340 meV in GaAs [40]). Note that the octahedral distortions were neglected for the calculated results in Figure 2.2.

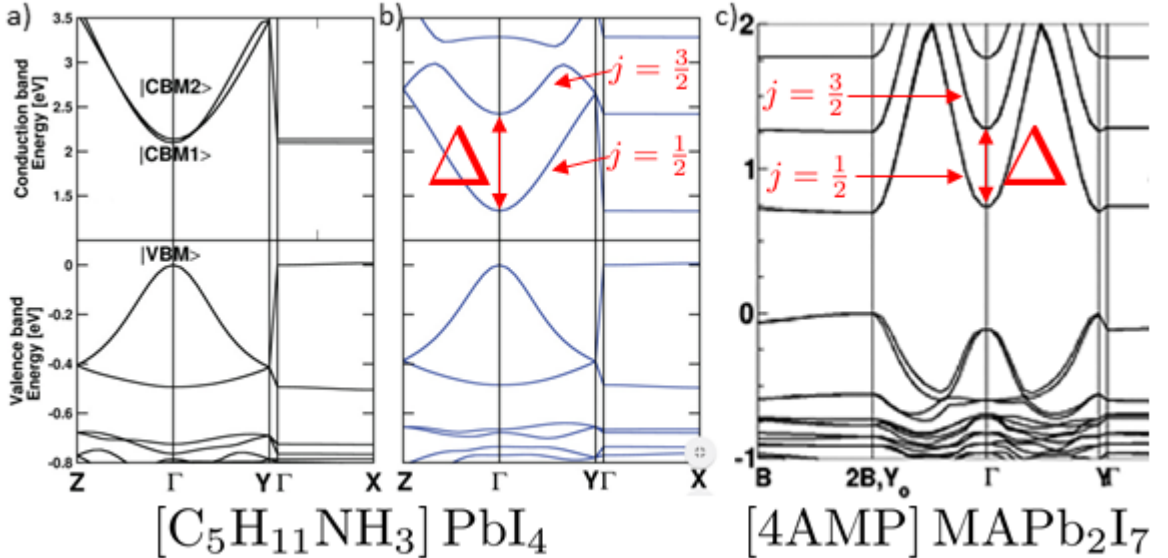


Figure 2.2: Density functional theory calculations of band structure $[\text{C}_5\text{H}_{11}\text{NH}_3]\text{PbI}_4$ without (a) and with (b) spin-orbit coupling. (c) Calculated band structure for $(4\text{AMP})\text{MAPb}_2\text{I}_7$ including the effects of spin-orbit coupling. Adapted from reference [48] (a and b) and [70] (c). Red double headed arrow indicates the spin-orbit splitting Δ .

2.1.2 Optical Transitions in Semiconductors

While considering particular optical transitions in a semiconductor it will be convenient to consider the incident light field as a weak perturbation to the eigenstates of the system without a light field. The unperturbed Hamiltonian can be expressed as:

$$H_{\text{Bloch}} |\nu\vec{k}\rangle = e_{\nu\vec{k}} |\nu\vec{k}\rangle \quad (2.1)$$

where $|\nu\vec{k}\rangle$ are the eigenstates of the unperturbed Hamiltonian, *i.e.* Bloch states described by the wavefunctions in equation 1.3, and $e_{\nu\vec{k}}$ are the eigenvalues. As discussed in section 1.2 the periodic part of the Bloch states ($U_k(\vec{r})$) are known as the cell functions. These appear as a linear combination of hydrogenic orbitals centered about each atom. The bands in a semiconductor originate from the bonding and anti-bonding atomic orbitals in the unit cell. For example in GaAs the valence band is formed by the (sp3 hybridized) p-like bonding orbitals while the conduction band is formed from the s-like anti-bonding orbitals.

To gain insight as to how light interacts with electrons in a semiconductor, we can consider an electron-hole pair in a direct band gap semiconductor as a dipole with a perturbing light field described as:

$$\vec{E}(t) = \hat{e}E_0e^{-i\omega t} \quad (2.2)$$

where \hat{e} is the polarization vector of the light field and ω is the angular frequency of the incident light. The perturbing Hamiltonian caused by the light field can be expressed as:

$$\mathbf{H}_{ph} = -e\vec{r} \cdot \vec{E}(t) \quad (2.3)$$

This is known as the electric-dipole approximation. We can express the perturbing Hamiltonian in terms of the Bloch eigenstates $|\nu\vec{k}\rangle$ as:

$$\mathbf{H}_{ph} = (E_0e^{-i\omega t}) \hat{e} \cdot \sum_{\nu\vec{k}} \sum_{\nu'\vec{k}'} |\nu'\vec{k}'\rangle \langle\nu'\vec{k}'| (-e\vec{r}) |\nu\vec{k}\rangle \langle\nu\vec{k}| \quad (2.4)$$

where the matrix elements of the electric dipole operator are:

$$\vec{d}_{\nu\nu'}(\vec{k}, \vec{k}') = \langle\nu'\vec{k}'| (-e\vec{r}) |\nu\vec{k}\rangle \quad (2.5)$$

By considering the commutator between the electric dipole operator and Hamiltonian operator:

$$[\mathbf{r}, \mathbf{H}_{Bloch}] = \langle\nu\vec{k}| [\mathbf{r}, \mathbf{H}_{Bloch}] |\nu\vec{k}\rangle \quad (2.6)$$

$$= \langle\nu\vec{k}| (\mathbf{r}\mathbf{H}_{Bloch} - \mathbf{H}_{Bloch}\mathbf{r}) |\nu\vec{k}\rangle \quad (2.7)$$

$$[\mathbf{r}, \mathbf{H}_{Bloch}] = \langle\nu\vec{k}| \mathbf{r} |\nu\vec{k}\rangle (e_{\nu\vec{k}} - e_{\nu'\vec{k}'}) \quad (2.8)$$

$$(2.9)$$

and recalling the commutator relations between position and momentum:

$$[\mathbf{r}, \mathbf{H}] = \frac{i\hbar}{m}\mathbf{P} \quad (2.10)$$

we can express the electric dipole operator as:

$$\vec{d}_{\nu\nu'}(\vec{k}, \vec{k}') = \frac{-i\hbar e}{m_e(e_{\nu\vec{k}} - e_{\nu'\vec{k}'})} \langle \nu'\vec{k}' | (\mathbf{P}) | \nu\vec{k} \rangle \quad (2.11)$$

where the transition is taken to be vertical ($\vec{k} = \vec{k}'$). This shows us that optical properties, such as transition rates and selection rules, are determined by the matrix elements of the momentum operator between different Bloch states. Since $\vec{k} = \vec{k}'$ the cell function part of the Bloch state is what determines the matrix elements. The matrix elements of \mathbf{H}_{ph} will only be non-zero for light polarizations where $\hat{\epsilon} \cdot \vec{d}_{\nu\nu'}(\vec{k}, \vec{k}') \neq 0$. This condition determines the optical selection rules. By considering the cell functions described in equation 1.3 we find the dipole matrix element vectors listed in Table 2.1 [40]. Figure 2.3 shows these transitions graphically. The red (blue) arrows indicate transitions between states of different spin angular momentum through the absorption of a right (left) helical photon carrying angular momentum of $+\hbar$ ($-\hbar$). As a result of these selection rules, excitation with circularly polarized light leads to a spin polarized distribution of electrons and holes. At the band edge of GaAs the electrons would be 50% spin polarized since the heavy and light hole valence bands are degenerate. In perovskites, in contrast, circularly polarized light leads to a 100% spin polarized distribution.

2.2 Mechanisms of Spin Relaxation

If a circularly polarized optical pulse is used to excite electron-hole pairs in a perovskite, these carriers will be fully polarized initially. This polarization state will relax to a statistically random sample. Three spin-relaxation mechanisms have been identified for electrons and holes in semiconductors: The Bir-Aronov-Pikus (BAP), Elliot-Yafet (EY), and D'yakonov-Perel (DP), named according to their discoverers.

2.2.1 Bir-Aronov-Pikus

In the BAP mechanism, carriers can undergo spin relaxation in a p-doped semiconductor through electron-hole spin-exchange interactions. The exchange interaction

Band	Valence	Conduction	
		$\frac{+1}{2}$	$\frac{-1}{2}$
Heavy Hole	$\frac{+3}{2}$	$-\sqrt{\frac{1}{2}}(\vec{x} + i\vec{y})$	0
	$\frac{-3}{2}$	0	$\sqrt{\frac{1}{2}}(\vec{x} - i\vec{y})$
Light Hole	$\frac{+1}{2}$	$\sqrt{\frac{2}{3}}(\vec{z})$	$-\sqrt{\frac{1}{6}}(\vec{x} + i\vec{y})$
	$\frac{-1}{2}$	$\sqrt{\frac{1}{6}}(\vec{x} - i\vec{y})$	$\sqrt{\frac{2}{3}}(\vec{z})$
Split Off	$\frac{+1}{2}$	$-\sqrt{\frac{1}{3}}(\vec{z})$	$-\sqrt{\frac{1}{3}}(\vec{x} + i\vec{y})$
	$\frac{-1}{2}$	$-\sqrt{\frac{1}{3}}(\vec{x} - i\vec{y})$	$\sqrt{\frac{1}{3}}(\vec{z})$

Table 2.1: Optical Selection rules for the transitions between the light hole, heavy hole and split-off bands to the conduction band in GaAs. \vec{x}, \vec{y} indicate unit vectors perpendicular to the direction of $\vec{d}_{\nu\nu'}(\vec{k}, \vec{k})$, \vec{z} indicate unit vectors parallel to the direction of $\vec{d}_{\nu\nu'}(\vec{k}, \vec{k})$.

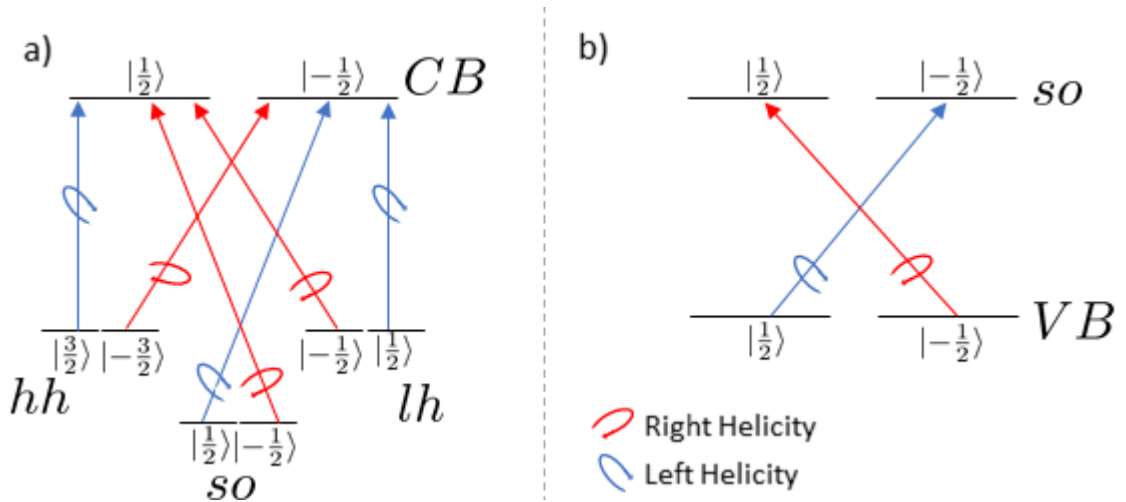


Figure 2.3: Optical selection rules for (a) bulk GaAs and (b) perovskites. The state kets are labelled with the angular momentum quantum number in each band. The red arrows indicate transitions through the absorption of a right helical photon carrying angular momentum of $+\hbar$ while the blue arrows indicate transitions through the absorption of a left helical photon carrying angular momentum of $-\hbar$. so- split-off band. hh - heavy hole band. lh - light hole band. CB - conduction band. VB - valence band.

Hamiltonian is given by:

$$\mathbf{H} = \mathbf{AS} \cdot \mathbf{J}\delta(\mathbf{r}) \quad (2.12)$$

where A is proportional to the exchange integral between the conduction and valence states, \mathbf{J} is the angular momentum operator for electrons, \mathbf{S} is the spin operator for holes, and \mathbf{r} is the relative position of electrons and holes. The relaxation rate has been calculated for p-doped III-V systems as:

$$\frac{1}{\tau_s} \propto N_p a_B^4 \frac{\Delta_{ex}^2}{E_B} k \quad (2.13)$$

Where a_B is the exciton bohr radius, N_p is the concentration of holes, Δ_{ex} is the exchange splitting between electrons and holes, and E_B is the exciton binding energy [40]. This mechanism is expected to be weak in perovskite materials due to the small value of the exchange splitting [44]. This mechanism will therefore not be discussed further in this thesis.

2.2.2 Elliot-Yafet

The EY mechanism works in conjunction with the spin-orbit coupling described by equation 1.1. The band state $|j, m_j\rangle$ discussed earlier corresponds to the eigenstates at $\vec{k} = 0$. In the presence of the spin-orbit interaction, away from $\vec{k} = 0$, the states are admixtures of the j -states. The rate of spin relaxation via the EY mechanism can be expressed as:

$$\frac{1}{\tau_s(\mathbf{E})} \propto \left(\frac{\Delta}{E_G + \Delta} \right)^2 \left(\frac{E}{E_g} \right)^2 \frac{1}{\tau_p} \quad (2.14)$$

where τ_p is the average momentum scattering time in state E . Since the band states are not eigenstates of spin, each scattering event has a non-zero probability of causing a spin flip. The stronger spin-orbit splitting (Δ) relative to the band gap, the stronger the degree of spin mixing of the band states, the shorter the spin lifetime. A distinguishing feature of this mechanism is that the spin lifetime is proportional to the momentum scattering time. As the carrier density increases the momentum scattering time should decrease and the spin flip lifetime should also decrease. Therefore; the spin lifetime should be inversely related to carrier density if the dominate relaxation pathway is the EY mechanism.

2.2.3 D'yakonov-Perel

The DP mechanism is also caused by the spin-orbit interaction in systems lacking in inversion symmetry, such as III-V and II-VI semiconductors. As discussed in section 1.6, the spin splitting induced by the asymmetry can be described by an intrinsic \mathbf{k} dependent magnetic field, $\mathbf{\Omega}(\mathbf{k})$, about which the electrons spin will precess with Larmor frequency $\mathbf{\Omega}_L(\mathbf{k}) = (e/m)\mathbf{\Omega}(\mathbf{k})$. The corresponding Hamiltonian is given by:

$$\mathbf{H}(\mathbf{k}) = \frac{1}{2}\hbar\sigma \cdot \mathbf{\Omega}_L(\mathbf{k}) \quad (2.15)$$

Since the effective magnetic field varies in magnitude and direction with \vec{k} , electrons at different \vec{k} 's will precess at different rates and about axes in different directions. This collective precession will cause an initially spin polarized distribution of carriers to become random. In contrast to the EY process, scattering of carriers slows spin relaxation because the carrier's spin does not precess as far between scattering events.

As this spin relaxation process occurs between scattering events, an electron can rotate an angle $\delta\phi = \Omega\tau_p$ before another scattering event takes place. It will then scatter to another \vec{k} -state where the effective magnetic field is different. As a result one can consider the phase of the spin state experiencing a random walk with time steps $1/\tau_p$. After a time t the phase will evolve to:

$$\phi(t) = \delta\phi\sqrt{t/\tau_p} \quad (2.16)$$

Defining the spin relaxation time as the time it takes for the phase to progress between the 0 and 1 state, we find the usual motional narrowing expression:

$$\frac{1}{\tau_s} = \mathbf{\Omega}_L^2\tau_p \quad (2.17)$$

The rate of this process is determined by $|\mathbf{\Omega}(\vec{k})|$, which is determined by the strength of the SOC, the degree of inversion asymmetry, and the momentum scattering time. In contrast to the EY mechanism, the spin relaxation time is inversely proportional to the momentum scattering time. Therefore; the spin lifetime will be directly proportional to the carrier density if the dominate spin relaxation pathway is the DP mechanism.

2.3 Symmetry Dependent Effects of Spin-Orbit Coupling

As discussed in section 1.6, the spin orbit interaction leads to an effective magnetic field $\mathbf{\Omega}(\vec{k})$. In the general case, this is given by

$$\mathbf{\Omega}(\vec{k}) = \langle \nu_{vk} | \frac{\hbar}{4m_e^2 c^2} (\nabla V \times (\hbar \mathbf{k} + \mathbf{P})) | \nu_{vk} \rangle \quad (2.18)$$

The direction of symmetry breaking reflects the direction of $\nabla V(\vec{r})$. This will depend on the bulk inversion asymmetry in the semiconductor crystal structure.

For instance, GaAs is a polar semiconductor with electric fields along each bond between an As and Ga atom. The symmetry of the effective magnetic field in \vec{k} space is determined by the symmetry of these polar bonds in real space. Dresselhaus analysed the effective magnetic field for this system and found that it has the form [102]:

$$\mathbf{\Omega}(\vec{k}) = \frac{\alpha \hbar^2}{m_c \sqrt{2m_c E_G}} \begin{cases} k_x (k_y^2 - k_z^2) \hat{x} \\ k_y (k_z^2 - k_x^2) \hat{y} \\ k_z (k_x^2 - k_y^2) \hat{z} \end{cases} \quad (2.19)$$

This effective magnetic field has a much more complicated structure than the simple Rashba magnetic fields introduced in section 1.6, reflecting the more complicated spatial dependence of $\nabla V(\vec{r})$. In the general case, as can be seen in equation 2.18, the strength of the effective magnetic field will depend on the matrix elements between Bloch states in the crystal. The origins of the large spin orbit coupling in perovskites occurs due to the large atomic number, Z , which is reflected in the cell functions for the band edge states being 6s and 5p.

Inversion asymmetry in 2D perovskite structures is dictated by the tilting or twisting of the lead iodide octahedra in the perovskite crystal structure, which leads to differences in the adjacent Pb-I bond lengths. The magnitude and direction of these distortions are determined by the interplay of the small and long organic cations in the structure. It is of interest to compare the case of BA to 4AMP as it isolates the role of the spacer molecule. In the BA structure (shown in Figure 1.10 (a)) the spacing layer is made up of two sheets of (+1) butylammonium cations, which occupy a place that would be occupied by a methylammonium cation in bulk MAPbI₃. The butylammonium nitrogen groups bond to all the surrounding iodide atoms in the

perovskite octahedra, causing both out of plane tilting and in plane rotation to the octahedra. In contrast, the 4AMP perovskite (shown in Figure 1.10 (b)) is comprised of one sheet of (+2) 4-aminomethyl piperidine cations. The 4AMP nitrogen groups bond to the bridging iodide atoms, indicated by the red dashed lines in Figure 1.10 (b), this results in very little out of plane tilting of the perovskite octahedra. The out of plane tilting and in plane twisting of the octahedra results in differences in the Pb-I bond lengths creating a dipole across a unit cell. These dipoles are expressed as an intrinsic electric field in the greater lattice. In the case of BA this results in $\nabla V(\vec{r})$ having components both in the plane and out of the plane perpendicular to the stacking axis, while in the case of 4AMP this would lead $\nabla V(\vec{r})$ to lie in the plane perpendicular to the stacking direction.

The difference in the direction of $\nabla V(\vec{r})$ has a dramatic effect on the direction of the effective magnetic field tied to the bulk inversion asymmetry. Section 1.6 describes the case in which $\nabla V(\vec{r})$ is perpendicular to transport direction (*i.e.* parallel to the stacking axis). This leads to an in plane direction for $\Omega(\vec{k})$, perpendicular to both \vec{k} and the stacking direction (as shown in Figure 2.4 (a)). For the 4AMP case $\nabla V(\vec{r})$ is in the plane perpendicular to the stacking direction. Since \vec{k} is also in the plane, $\Omega(\vec{k})$ from equation 1.38 will be in the stacking direction for all \vec{k} . This situation is depicted in Figure 2.4 (b)).

In practice carriers spins are always optically injected along the stacking direction (with the light propagating direction parallel to the stacking axis). The effective magnetic field will have a different impact on the carrier spin dynamics for the two cases shown Figure 2.4. In the case where $\nabla V(\vec{r})$ is along the stacking direction (as shown in Figure 2.4 (a), the most common Rashba case), the carriers will undergo precessional spin relaxation via the DP process. In contrast, the case in which $\nabla V(\vec{r})$ is in the plane (as shown in Figure 2.4 (b), and is the case for the 4AMP structure) the effective magnetic field is parallel to the initial spin polarization direction and no precession occurs. In this case the DP mechanism is turned off, yet the Rashba effect is still present.

The situation in 4AMP is analogous to the case of (110)-oriented III-V quantum wells. Under quantum confinement, the bulk inversion asymmetry effective magnetic field in equation 2.19 is modified because the component of \vec{k} along the quantum

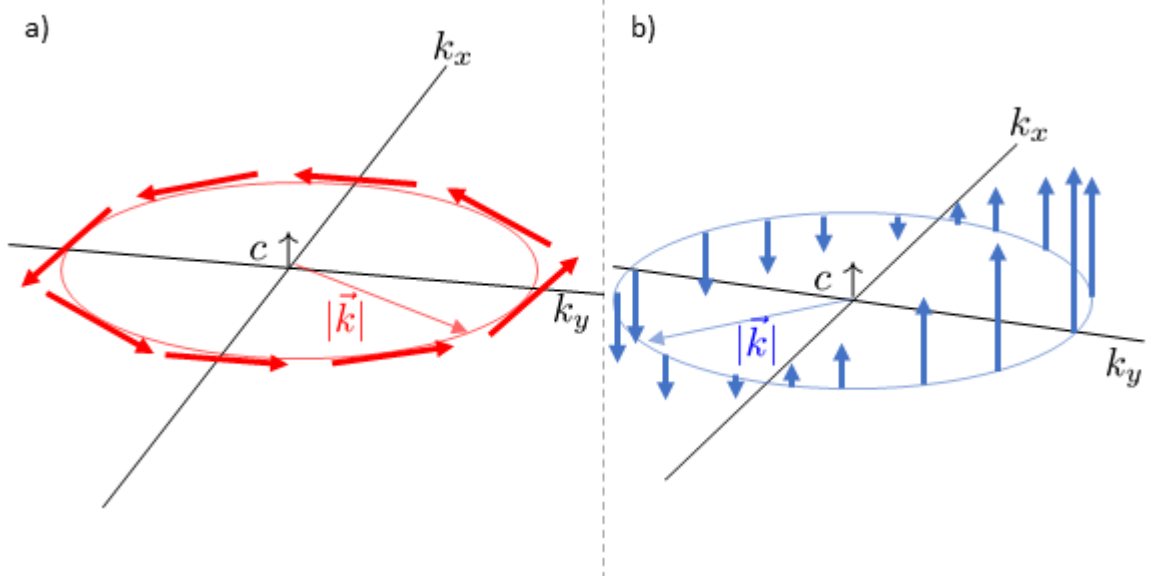


Figure 2.4: Rashba magnetic fields for the cases if bulk inversion asymmetry (a) parallel and (b) perpendicular to the stacking axis. Analogous to BA and 4AMP respectively.

well confined direction is enlarged, causing certain components of $\Omega(\vec{k})$ to become dominant. For confinement along the (110) direction, the effective magnetic field is along the stacking direction, with the same form as Figure 2.4 (b). The turning off of the DP process in (110) oriented III-V quantum wells has been shown for both AlGaAs [103] and InAs/GaSb systems [99]. The structure of $\Omega(\vec{k})$ in Figure 2.4 (b) is very useful for the development of spintronic devices because, as long as the \vec{z} component of the spin is utilized, the trade off between spin lifetime and spin splitting is eliminated. This structure is the basis for both a spin resonant tunnelling diode [104] and a spin field-effect transistor [30].

Chapter 3

Experimental Techniques

3.1 Sample Fabrication

3.1.1 Precursor Crystals

The material studied in this thesis is the layered ($n = 2$) Dion-Jacobson Perovskite 4-aminomethyl piperidinium methyl ammonium lead iodide ((4AMP)MAPb₂I₇). The full chemical formula for this series of perovskites is (C₆N₂H₁₆)(CH₃NH₃) _{$n-1$} Pb _{n} I_{3 $n-1$} . The precursor crystals were fabricated at North Western University using a technique called reverse crystallization (laid out in reference [72]), sealed in glass vials, and shipped to Dalhousie University. In the reverse crystallization procedure, 449 mg (3 mmols) of 99.9 % PbO powder was dissolved in a solution of 6 mL of hydrogen iodide and 1 mL of hydrophosphorous acid by heating on a 130° hot plate under magnetic stirring for 5-10 minutes until the solution turned a bright yellow color. 477 mg (3 mmol) of methylammonium iodide was added directly to the above solution under heating. Separately 37.7 mg (0.33 mmol) of 4-aminomethyl piperidinium (C₆N₂H₁₆) was added to 0.5 mL of hydrogen iodide under magnetic stirring at room temperature. The second solution was added into the perovskite solution under heating and stirring over 5 minutes. The stirring was then turned off and the solution was allowed to cool to room temperature. During this process, dark red plate-like crystals precipitated at the bottom of the vial. These crystals were then extracted via vacuum suction and dried. This returned a yield of 684 mg, or 31.5% based on initial lead content.

3.1.2 Thin Films

The thin films used in this thesis were fabricated, by the author, in the Hill Laboratory at Dalhousie University. 127.5 mg of (4AMP)MAPb₂I₇ was dissolved in 101.2 μ L of DMF (0.45 M) and heated on a hotplate under magnetic stirring for one hour. This created a yellow opaque solution. A clean and UV-treated sapphire substrate (0.5

mm thick, 12.7 mm in diameter) was heated to 120° on a hot plate. The substrate was then transferred to the spin coater and 75 μL of the perovskite solution was micro-pipetted onto the center of the substrate. The substrate was then spun for 20 seconds at 5000 rpm. During this process the perovskite solution stayed opaque. As soon as the spin cycle was completed, the sapphire was transferred to the hot plate and the opaque solution rapidly (≤ 5 seconds) turned a dark red color starting from the center and moving radially outwards. The resultant film was smooth, dark red, and semi opaque film completely covering the substrate. Figure 3.1 (a) shows a photograph of the completed sample held in a cold finger tip. The resultant film was stored in a dry nitrogen glove box and transferred to a Janis ST-100 cryostat when under investigation.

3.2 Linear Absorbance

Linear Absorbance, also known as optical density or extinction, is a measure of the attenuation of transmitted light through a sample. A broadband source is focused onto a sample and the transmission is monitored via a spectrometer. This is compared to a reference spectrum representing the incident flux. Absorbance is related to the ratio of the incident to the transmitted flux as:

$$A = \log_{10} \left(\frac{\phi_i}{\phi_t} \right) \quad (3.1)$$

where ϕ_i and ϕ_t are the incident and transmitted fluxes respectively. In these experiments the source was a broadband tungsten halogen lamp (LS-1-LL) purchased from Ocean Optics, the sample was held in an ST-100 cryostat, and the transmitted light was collected by a Ocean Optics USB-4000 spectrometer. The light from the tungsten lamp was coupled via a QP1000-2-VIS-BX ocean optics optical fibre into the probe focusing lens in Figure 3.8, resulting in a beam waist of 2 mm. Moving the beam spot to various locations on the sample showed little change in the absorption spectrum, indicating homogeneous optical density across the sample.

Figure 3.1 (b) shows the linear absorption spectra for the thin film prepared at Dalhousie University (black curve), along side the 4AMP series, for single crystals, collected at North Western University and a bulk MAPbI_3 crystal, adapted from reference [70]. These data have been normalized for easy comparison, as the thickness

of the sample greatly increases the optical depth. The optical absorption at 2.21 eV for the thin film created at Dalhousie University was found to be 1.2, leading to an optical depth of 2.7. From a comparison between the green curve in Figure 3.1 and the black curve (our sample), it is clear that the thin film is primarily composed of $n = 2$ 4AMP. The increase in absorbance associated with the exciton (~ 2.05 eV) and interband (~ 2.15 eV) transitions occur at the same spectral locations in the black and green curve. The exciton is weaker relative to the interband transitions in our thin film sample, which is expected because the results from reference [70] are taken on single crystals of 4AMP. The increased disorder in the film will broaden the exciton resonance, reducing the relative height of the absorption spectrum. The presence of weak absorption (between 1.8 and 2.0 eV) below the band gap of the $n = 2$ thin film likely reflects contamination with a small amount of $n = 3$ 4AMP. As the absorption coefficient for the $n = 3$ case is much larger than the $n = 2$ case around 1.8 eV and the measured absorption in this region is small compared to that associated with the $n=2$ material, the amount of $n = 3$ contamination in the sample must be small and most of the optical excitation will occur in the $n = 2$ crystals. In addition, some contamination by $n = 1$ 4AMP cannot be ruled out from the absorption spectrum alone since it would be superimposed as the interband response for $n = 2$ at high photon energies. Such contamination, if present, would not affect the differential transmission and circular dichroism measurements described in sections 3.5.1 and 3.5.2, as the photon energies used in those experiments are between 2.0 and 2.2 eV, below the exciton transition for $n = 1$ (~ 2.3 eV).

3.2.1 Tauc Analysis

A Tauc analysis is used to determine a semiconductor's band gap. The analysis consists of plotting the absorbance of light times the energy at that absorbance $((\alpha h\nu)^{1/r})$, vs the energy $(h\nu)$, where the quantity r denotes the nature of the transition ($r = 1/2$ for direct allowed transitions, applicable to the present case [40, 72]). The resulting plot has a linear regime between the exciton and interband transitions. Extrapolating this regime to the horizontal axis gives the material's optical band gap. Figure 3.2 shows the Tauc analysis for the 4AMP sample. The bandgap was determined to be 2.13 ± 0.04 eV, consistent with literature values [72].

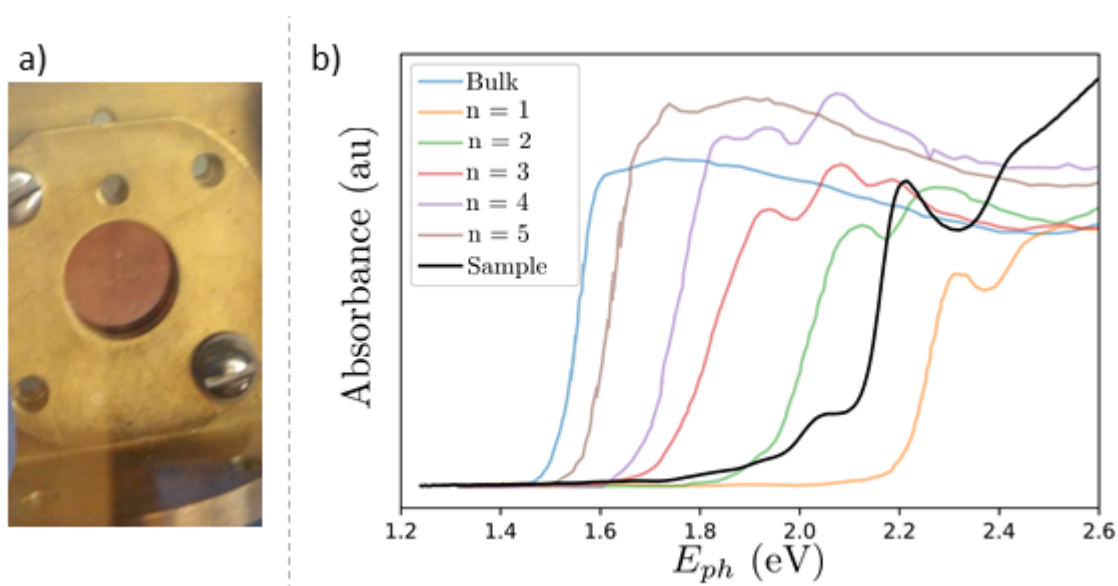


Figure 3.1: Linear Absorption spectra for 4AMP series of single crystals made at North Western University (coloured curves), adapted from reference [70], and $n = 2$ 4AMP film fabricated at Dalhousie University (black curve).

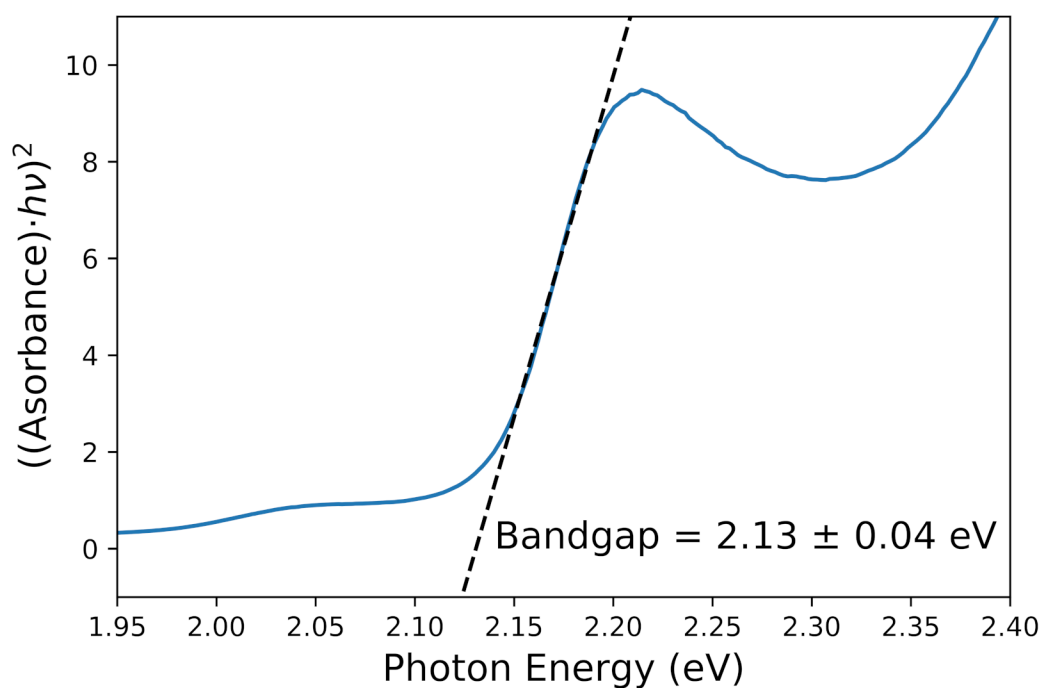


Figure 3.2: The tauc analysis carried out on the 4AMP material. The bandgap was determined to be 2.13 ± 0.04 eV.

3.3 X-ray crystallography

X-ray diffraction (XRD) is a technique used to determine the atomic and molecular structure of a crystalline material. A periodic lattice such as that shown in the inset of Figure 3.3 (a) consists of planes on which the atoms are rigidly stuck (at 0 K). An incident beam of x-rays will interfere constructively only if the extra length travelled by different x-rays from successive planes is a half integer multiple of the x-ray wavelength. This is known as Bragg's Law and is given by:

$$d \sin \theta = n \frac{\lambda}{2} \quad (n = 1, 2, 3 \dots) \quad (3.2)$$

By scanning across a range of theta, constructive interference angles for each plane can be found and equation 3.2 can be solved to find the plane spacing d .

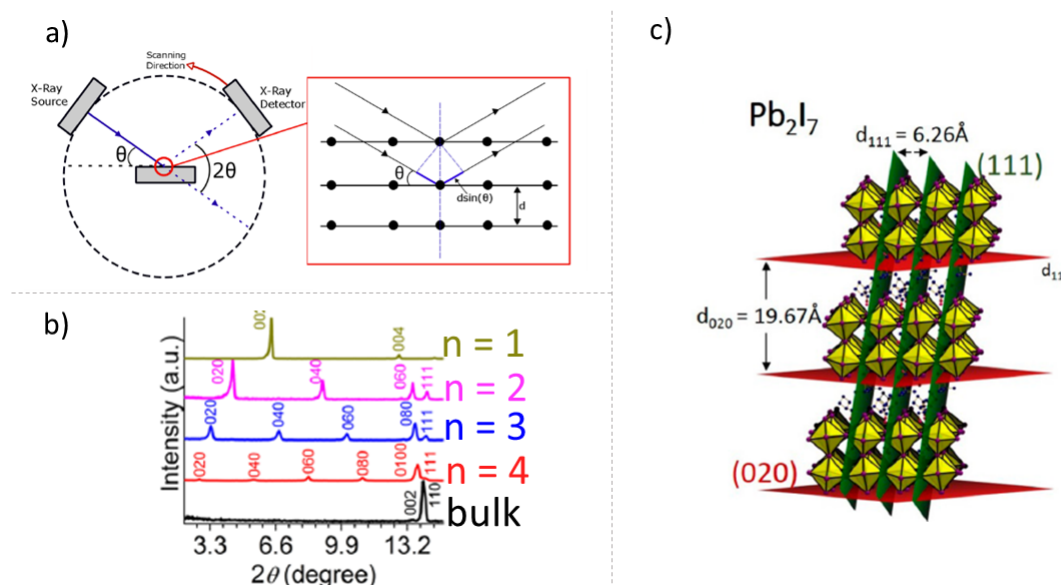


Figure 3.3: (a) Schematic representation of the XRD apparatus (inset) a representation of Bragg scattering from a crystal lattice. (b) XRD taken on $BA_2MA_{n-1}Pb_nI_{3n-1}$ for $n = 1, 2, 3, 4$, and (c) an illustration of the diffraction planes for the $n = 2$ case. Adapted from reference [87]

XRD is also useful in determining the thickness and orientation of a confined structure. This is known as grazing XRD as low angle peaks ($< 20^\circ$) can be used to identify the orientation. Figure 3.3 (b) shows the XRD intensity as a function of angle for $BA_2MA_{n-1}Pb_nI_{3n-1}$ ($n = 1, 2, 3, 4$) [70]. The numbering of the peaks correspond to

the Miller indices of the diffraction plane. The $(0k0)$ family of planes, ($k = 2, 4, 6 \dots$) correspond to the stacking of the perovskite layers parallel to the substrate, as shown by the red planes in Figure 3.3 (c). As the physical distance between the planes increases the angles corresponding to each member of the $(0k0)$ family decreases. This effect is seen in Figure 3.3 (b) where the (020) and (040) planes appear closer together in angle for $n = 1$ but farther apart for $n = 3$, compared to the $n = 2$ case. The (111) peak, located near 13° , corresponds to the stacking of perovskite layers perpendicular to the substrate, shown by the green planes in Figure 3.3 (c). Therefore; the number of perovskite octahedra making up the layers can be determined from the number of evenly spaced $(0k0)$ peaks below the (111) peak, while the orientation of the stacking layers can be qualitatively found by comparing the relative intensity of the $(0k0)$ peaks to the (111) peak.

Thin films were prepared at North Western university under identical conditions as those studied in the optical experiments in this thesis while the author was visiting collaborators there. These samples were characterized using a Rigaku Ultima IV X-Ray Diffractometer, with a beam size of 0.4×12 mm. Figure 3.4 shows the results of grazing angle X-Ray diffraction measurements, plotted on a log scale, taken on these samples. The presence of three evenly spaced relatively intense peaks, indicated by the black dashed lines, indicates the presence of the (020) , (040) , and (060) planes for the $n = 2$ case. The absence of a (111) plane, which should appear just after this triplet, indicates that the films have formed a parallel alignment to the substrate. Note here that although these angles do not correspond perfectly to the expected values for the $(0k0)$ family of planes, the author and collaborators are confident in this assertion as a small tilt in the thin film during measurements can cause a relative shift in these angles. There are small, but not insignificant, features at 4.1° , 8.64° , and 12.00° , this is most likely due to the presence of some $n = 3$ material. While the small features at 7.98° and 14.30° are most likely due to some $n = 4$ material. This mixing of layer numbers is caused by imperfect stoichiometric ratios during the reverse crystallization of the perovskite platelets. This mixing of the layers is consistent with the linear absorption measurements in Figure 3.1.

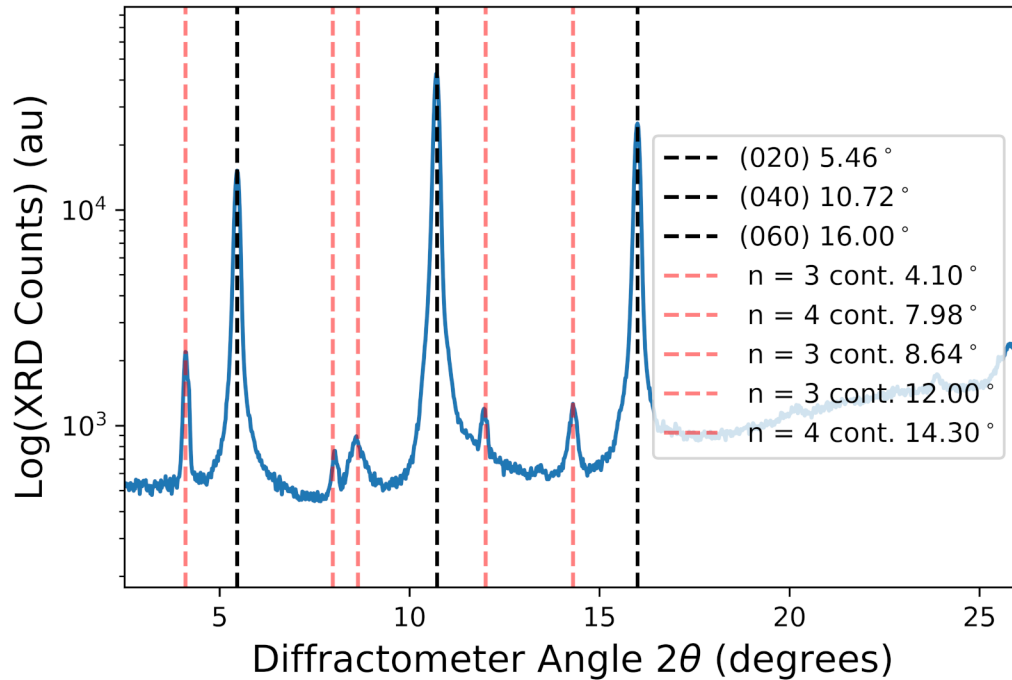


Figure 3.4: Results of X-Ray diffraction measurements, plotted on a log scale, taken on a sister sample created under equivalent conditions at North Western University. Dashed black lines indicate the peaks associated with $n = 2$, red dashed lines indicate contamination with other layer numbers.

3.4 Ultrafast Laser Source

Since the carrier dynamics described in section 1.5 occur on picosecond timescales it is necessary to use a probe that has sub-picosecond resolution. Since this is not possible using any mechanical shuttering or timing techniques, such as those used in time resolved photoluminescence, ultrafast light sources on femtosecond timescales are utilized. The light source used here was purchased from Coherent Inc. and is composed of three main components: (i) the Verdi-V18 pump laser, (ii) the Mira HP oscillator cavity, and the (iii) APE Optical Parametric Oscillator, and is shown in Figure 3.5.

3.4.1 Verdi-V18 Pump Laser

The Verdi V-18 is a solid state continuous wave diode pump laser. This output is used to pump a gain medium of Nd:YV₀₄ (Neodymium doped Vanadate), with a

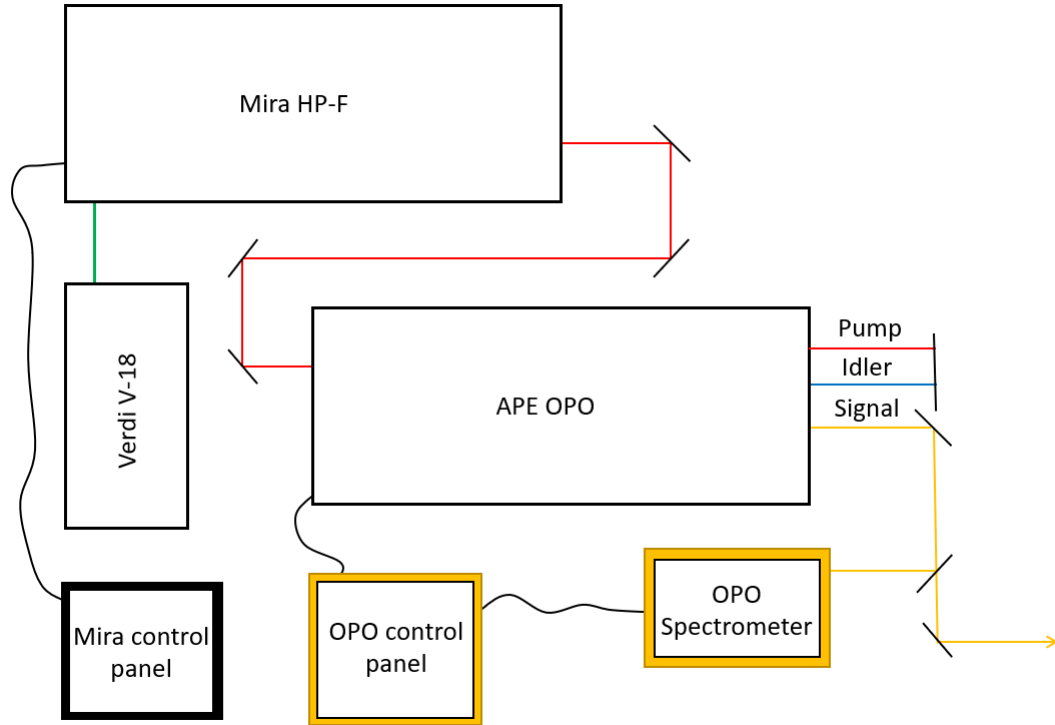


Figure 3.5: A schematic overview of the laser system used in this thesis work. The Verdi V-18 pumps the Mira HP-F oscillator cavity, which in turn pumps the APE OPO. The OPO converts the Mira output into the visible spectrum with tunability between 550 nm and 770 nm. The OPO spectrometer measures the output spectrum of the OPO which is used as feedback to control the cavity length.

characteristic wavelength of 1064 nm. Part of the 1064 nm light is converted into 532 nm light through a process known as frequency doubling, achieved through the χ^2 interaction of a lithium triborate crystal. The 532 nm output of the Verdi is used to pump the Mira HP-F ultrafast laser cavity.

3.4.2 Mira HP-F

The Mira HP-F, shown in figure 3.6, is a mode-locked ultrafast laser cavity that uses a Ti:Sapp gain medium (sapphire doped with titanium), and a built-in prism group velocity dispersion (GVD) compensator. This enables the creation of near transform limited pulses of 150 fs, at 76 MHz repetition rate, and tunability between 700 nm and 980 nm. Mode-locking is achieved through the Kerr Lens mode-locking. The Kerr effect corresponds to the fact that high intensities of light will experience a nonlinear

refractive index ($n \approx n^0 + n^2(I)$). Since the laser has a Gaussian cross section this effect leads to the focusing of light. The laser initially operates in continuous wave mode. Any noise spike generated in the cavity will get preferentially focused through the Kerr effect in the Ti:Sapp gain medium. Mode locking is achieved by placing a slit aperture at a location in the cavity where the Kerr focused light will experience a beam waist. The noise spike experiences a larger net gain and the residual continuous wave components transition to a state of net loss until only one pulse remains in the cavity. The repetition rate of the laser is determined by the length of the cavity since a portion of this single pulse leaks through the cavity end mirror on each round trip. This in conjunction with a slit aperture at the cavity output creates a pulsed output with no continuous wave components. The effective cavity length is controlled by the birefringent filter, which introduces a wavelength dependent loss, allowing for controllable spectral output.

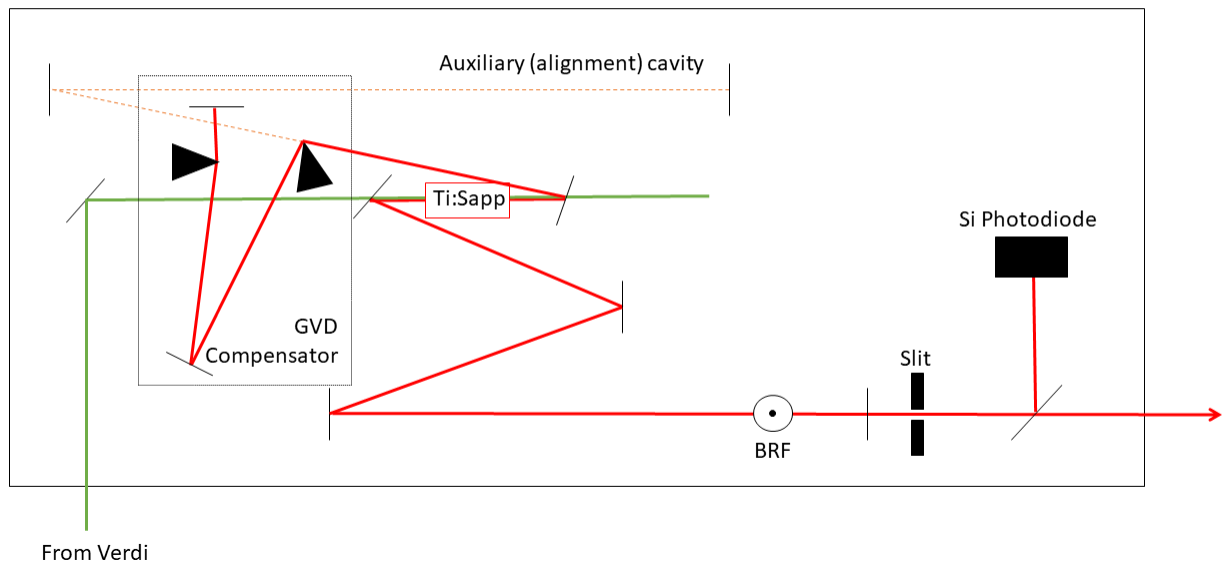


Figure 3.6: A schematic diagram of the Mira HP-F. Here the Kerr Lens mode-locking occurs within the Ti:Sapp crystal. GVD - group velocity compensator. BRF - birefringent filter.

3.4.3 APE Optical Parametric Oscillator (OPO)

The OPO, shown schematically in Figure 3.7 is designed to frequency transform the femtosecond pulses generated in the Ti:Sapp oscillator, outputting at 830 nm, into the visible wavelength range. This is achieved through a χ^2 process known as optical parametric down conversion and the use of a periodic poled crystal. In parametric down conversion, a high energy pump photon is converted into two lower energy photons, known as the signal (higher energy) and idler (lower energy), obeying the laws of conservation of momentum and conservation of energy. From conservation of momentum:

$$\vec{k}_{\text{Pump}} = \vec{k}_{\text{Signal}} + \vec{k}_{\text{Idler}} \quad (3.3)$$

$$\frac{n(\lambda_{\text{Pump}})}{\lambda_{\text{Pump}}} = \frac{n(\lambda_{\text{Signal}})}{\lambda_{\text{Signal}}} + \frac{n(\lambda_{\text{Idler}})}{\lambda_{\text{Idler}}} \quad (3.4)$$

and conservation of energy:

$$E_{\text{Pump}} = E_{\text{Signal}} + E_{\text{Idler}} \quad (3.5)$$

$$\frac{1}{\lambda_{\text{Pump}}} = \frac{1}{\lambda_{\text{Signal}}} + \frac{1}{\lambda_{\text{Idler}}} \quad (3.6)$$

This process requires the pump, signal, and idler beams to propagate through the crystal at the same phase speed, known as phase matching. Since crystalline materials contain dispersion, the index of refraction changes with wavelength ($n(\lambda_{\text{Pump}}) \neq n(\lambda_{\text{Signal}})$). In most parametric down conversion materials, these indices can be made to match using the two axes of a birefringent crystal. However; this limits the spectral range of the output and can lead to restrictions on which crystallographic orientations may be used, limiting the conversion efficiency. A more modern technique known as quasi-phase matching uses a periodic poled crystal. A periodic poled crystal consists of alternating thin strips of a bulk crystal with oppositely poled domains. The idea is to allow the waves of λ_{Pump} and λ_{Signal} to walk off and walk back on in successive poled regions, where the index of refraction is repeatedly reversed. These crystals are manufactured by sequentially growing a thin slice of the bulk crystal and applying an high (2-3 KV) voltage across the most recently grown domain creating a permanent electric dipole. The next domain is then grown and the voltage is reversed. This

results in a an effective χ^2 susceptibility with constant amplitude and opposite sign. The length of the poled sections is chosen such that the pump wavelength is phase shifted $\pi/2$, which brings the pump back into phase with the signal beam in the next domain of the crystal. This is equivalent to modifying equation 3.3 to:

$$\frac{n(\lambda_{\text{Pump}})}{\lambda_{\text{Pump}}} = \frac{n(\lambda_{\text{Signal}})}{\lambda_{\text{Signal}}} + \frac{n(\lambda_{\text{Idler}})}{\lambda_{\text{Idler}}} + \frac{1}{\Delta} \quad (3.7)$$

where Δ is the period of poling.

This configuration of the OPO allows for down conversion (down in energy). Therefore; the output of a OPO is limited to wavelengths greater than the original output of the Ti:Sapp, in practice. In order to access the visible range of the spectrum an intracavity periodically poled second harmonic LBO (Lithium Borate) crystal is used, allowing the output frequency to be doubled. A thermoelectric cooler is used to control the temperature of the crystal to phase match to the desired wavelength. The temperature of the LBO crystal and the desired wavelength is set by the operator while a P-I-D loop is employed by the OPO to control the cavity length with input via an external spectrometer. As the OPO is pumped by the Mira beam it also operates at a 76 MHz repetition rate.

3.5 Ultrafast Spectroscopy Techniques

3.5.1 Differential Transmission

Differential transmission, also known as pump-probe spectroscopy, is the most common form of ultrafast spectroscopy. Figure 3.8 shows a schematic of the experimental apparatus used in the differential transmission and circular dichroism experiments. The OPO creates pulses of light that are linearly polarized horizontal with respect to the optical table. These pulses are split by a beam splitter into the pump and probe pulses. The pump pulse travels through a half waveplate which is set to rotate the pulse 90° . This pulse then travels through the computer controlled delay stage that has a retro-reflector mounted on it, such that the time delay added to the line is twice the time taken for light to traverse the change in position of the retro-reflector. The pump then passes through the chopper blade, which modulates the laser pulse train at 400 Hz. The pump is then focused onto the sample, and the throughput is blocked. This pulse changes the absorption coefficient of the sample by optically

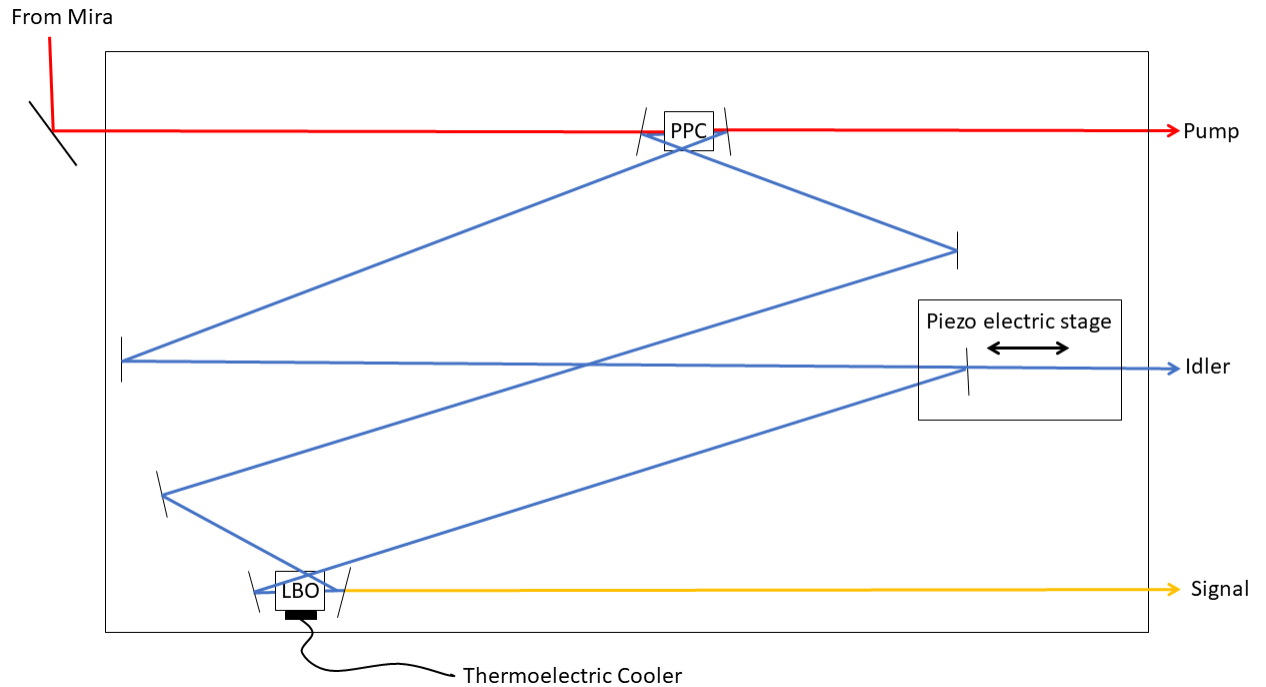


Figure 3.7: A schematic diagram of the APE OPO. Here blue is used to represent infrared wavelengths.

injecting carriers into the conduction band according to equation 1.28. Concurrently, the probe pulse travels through a wave plate oriented such that the polarization is not rotated. The average power of the probe pulse is kept much less (at most 10%) that the pump, this is to reduce the change in absorption due to the probe beam itself. This attenuation is achieved through the use of neutral density wheels placed in both the pump and probe path. The probe pulse is then focused at the same spot on the sample as the pump, and the throughput is measured by a Thor-Labs PDA36A photo diode connected to the lock-in amplifier. The lock-in amplifier provides a measure of the change in voltage of the probe beam at the frequency of the pump modulation (400 Hz). The reading on the lock-in is then a direct measure of the change in absorption of the probe due to the presence of the pump. The change in absorption can be directly related to the change in the carrier concentration at that energy. Therefore this technique provides a probe of both the interband and intraband recombination dynamics in semiconductor materials. The differential transmission signal can be monitored as a function of delay between the pump and probe pulse by decreasing the distance travelled by the pump. The resulting data can be fit to equation 1.29

to extract the inter- and intraband carrier lifetimes. Although the lock-in amplification increases the signal to noise ratio to a measurable level, scatter from the pump beam will inevitably make it into the photo diode. This noise level can be reduced by using cross polarized beams. If the pump and probe beam are polarized 90° from one another (as in the case described above) and a linear polarizer is placed after the sample, the pump scatter can be greatly reduced. Figure 3.9 shows a close up schematic of this geometry.

At the beginning of each day the spatial overlap of the pump and probe beams must be found. This is done by placing a power meter behind the cryostat and the cryostat is moved such that the transmission of the probe beam passes through a $50 \mu\text{m}$ pinhole, held below the sample in the cryostat, is a maximum implying that the pinhole is located at the probe beam waist. The ratio of transmitted power to incident power (T) can be used to find the spot size (ω) of the focused beam through the relation:

$$\omega = a\sqrt{2} [\log(1 - T)]^{-\frac{1}{2}} \quad (3.8)$$

where a is the size of the pinhole. The pump beam is then focused, using the 3D stage the pump focusing lens is mounted on, through the same pinhole and the transmitted power is measured. The pump and probe beam spot size for the experimental conditions were found to be $\sim 60 \mu\text{m}$ at a pump/probe wavelength of 600 nm .

Once spatial overlap is achieved, the pump beam drift must be assessed. The transmission of the pump beam is monitored as the delay stage is moved to the extreme ends of its range, if the transmitted power changes by more than 5% the pump beam alignment into the delay stage is not parallel with the movement of the stage. This misalignment causes the pump beam to drift across the pinhole as the stage moves between its extremes, changing the transmission. If the change in transmission is greater than 5% the alignment into the delay stage must be altered and this process repeated until the transmission stays within 5%.

The pulse duration at the sample is not known precisely as an autocorrelation at these wavelengths would require a detector with a spectral range well into the UV. However; as the OPO outputs near transform limited pulses of 150 fs , and autocorrelations using the same experimental apparatus, with the Mira-HP beam as input yielded a pulse duration of $\sim 300 \text{ fs}$, it can be estimated that the pulse duration

is no more than 500 fs at the sample.

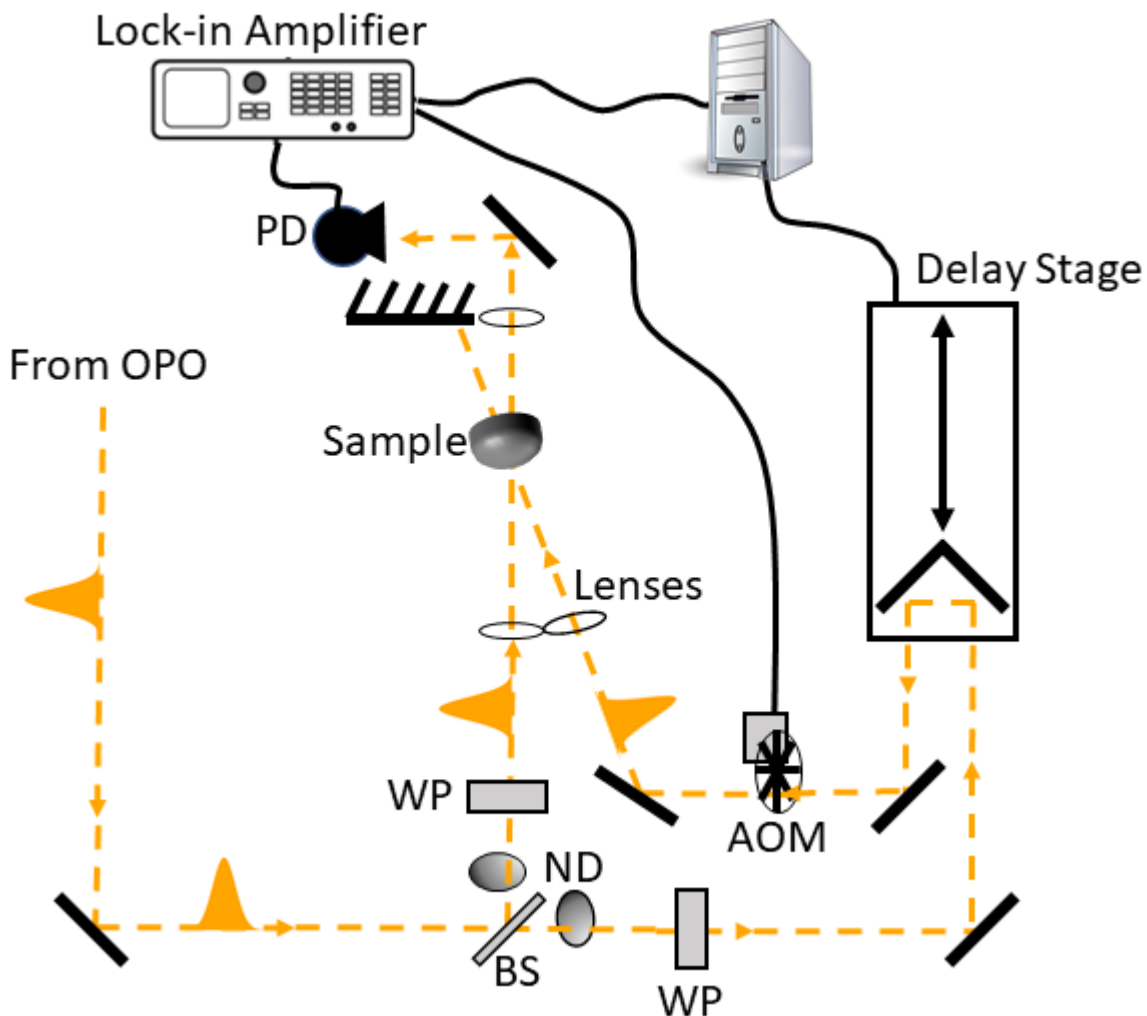


Figure 3.8: A schematic diagram of the entire experimental apparatus. In linear differential transmission the WP (waveplates) are half wave plates, while in circular dichroism the WP are replaced with quarter wave plates. BS - beam splitter, AOM - acousto optical modulator, PD - photodiode ND-variable neutral density wheels.

3.5.2 Circular Dichroism

In the case of circular dichroism, the same experimental apparatus shown in Figure 3.8 is used, except the half wave plates are replaced with quarter wave plates. The quarter waveplate in the probe path is set to create circular light of one helicity. The quarter wave plate in the pump path is set to create circular light of the same or opposite

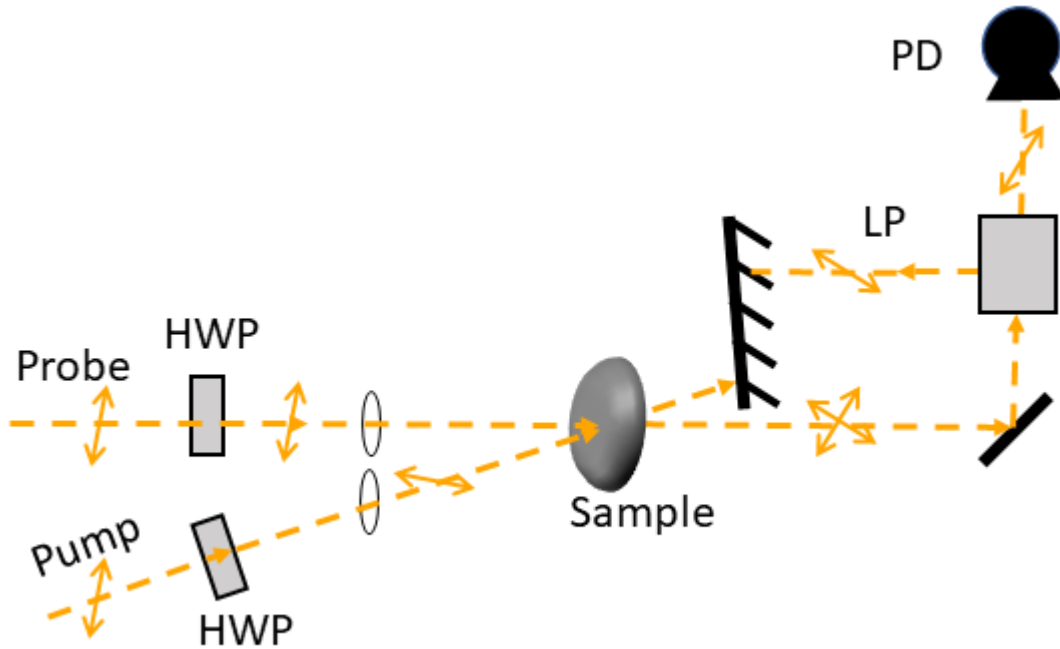


Figure 3.9: A schematic of the optical setup for a differential transmission experiment. The probe half wave plate (HWP) is set to add no rotation to the pulse, while the pump HWP rotates the pump beam by 90° . Both pulses are focused onto the sample and the throughput is a combination of the probe pulse and scatter from the pump beam. The linear polarizer (LP) is used to eliminate the pump scatter from the probe pulse.

helicity. Differential transmission data is collected for co-circular and counter-circular polarizations in the pump and probe beams, providing a measurement of the carrier dynamics of the injected and opposite spin states. This data can be used to calculate the degree of circular polarization and fit to equation 1.37 to extract the spin lifetime.

3.5.3 Calibration of Quarter Wave Plates

The light produced by the OPO has a linear polarization, for circular dichroism experiments the beams must be converted to circular polarization. This is accomplished for the pump and probe pulses by a quarter wave plate. A quarter wave plate is a birefringent material that has a fast and a slow axis, with indices of refraction n_f and n_s respectively ($n_f > n_s$). By orienting the incident light 45° to the birefringent axes and properly choosing the amount of material the light propagates through, one can

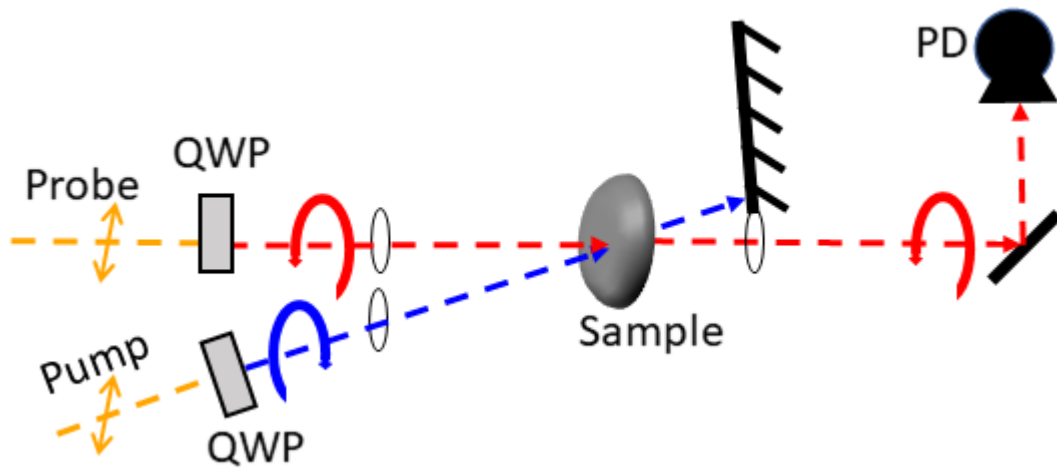


Figure 3.10: A schematic of the circular dichroism setup to probe the minority spin population. The pump beam injects carriers with spin dictated by the pulses helicity. Changes in the probe signal are an indication of the population of carriers with opposite helicity. quarter wave plate - quarter wave plate, PD - photodiode.

precisely choose the phase shift between the two components of the light field. To make circular polarized light the material thickness is chosen such that

$$\Delta\phi = \frac{2\pi(n_f - n_s)}{\lambda} = \frac{\pi}{2} \quad (3.9)$$

It is therefore imperative to know the orientation of the birefringence axes. Figure 3.11 shows a schematic of the apparatus used to verify the angle of the birefringent axes. The input HeNe beam, which is also linearly polarized, is split by a polarizing beam cube, the output travels through a quarter wave plate mounted in a 360° mount. If the quarter wave plate is set such that the input light is at 45° to the birefringent axis a $\pi/2$ phase shift will be introduced and perfectly circular light will be created. This will reflect off the mirror and pass back through the quarter wave plate, adding another $\pi/2$ phase shift, effectively acting as a half wave plate. The light will now be in the opposite linear polarization state as the input beam and will pass through the polarizing beam cube and be collected by the power meter. When the power meter reads high the quarter wave plate is set to create perfectly circular light.

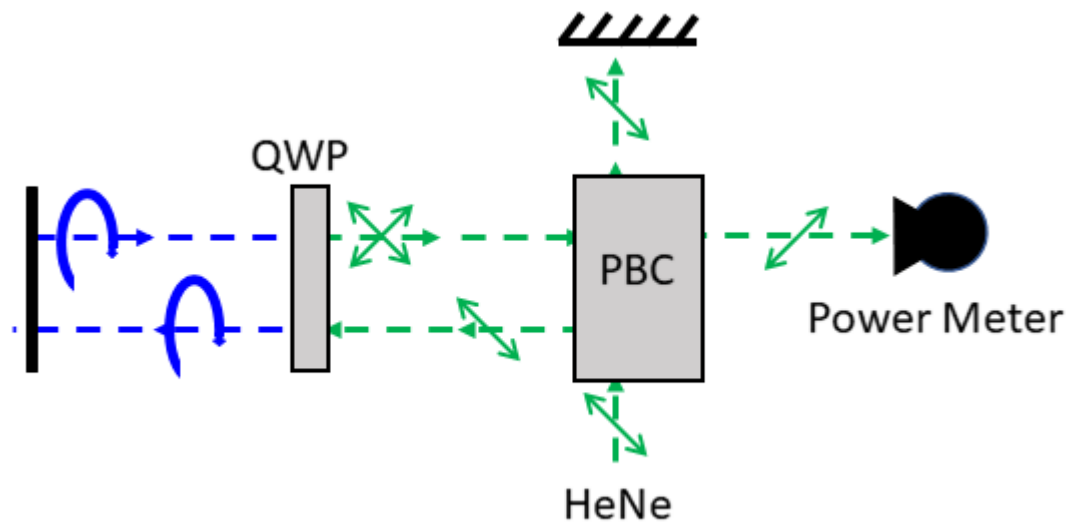


Figure 3.11: Schematic of the apparatus used to calibrate the quarter wave plates. In this diagram the HeNe laser outputs 633 nm horizontally polarized light, the quarter wave plate is set such that it creates perfectly circular light in the blue region, here the power meter would read high. PBC-polarizing beam cube. QWP-Quarter wave plate. Note: the optical paths are spatially separated here for ease of explanation, in practice the horizontal and vertical paths overlap one another.

Chapter 4

Results and Discussion

4.1 Photo Induced Degredation

As perovkites are known to degrade with exposure to illumination, it was imperative to discover the conditions under which the laser pulse would cause degradation to the sample so that those conditions could be avoided during the optical experiments. This was done by performing test measurements with the sample exposed to the laser beam. The throughput of the laser incident on the sample was monitored for a period of 5 minutes for a range of laser beam fluence values, where fluence is defined as:

$$\text{Fluence} = \frac{(\text{Average Power})}{\pi(\omega)^2 (\text{Repetition Rate})} \quad \text{units:} \left[\frac{\text{nJ}}{\text{cm}^2} \right] \quad (4.1)$$

where ω is the size of the beam waist. If the throughput was seen to rise, then the absorption coefficient of the film is dropping during laser exposure. The origin of this drop is not known but based on the linear absorption spectrum, the likely explanation is that the film is converting partially to $n = 1$. Since the band gap is much higher than the 2.21 eV photon energy used, these converted components of the film no longer contribute to the absorption. Since the absorption coefficient increases with increasing photon energy, the test was performed at the peak of the absorption curve (2.21 eV).

Figure 4.1 shows the results of this experiment. There is no rise in throughput for fluences 257 and 299 nJ/cm². There is a small rise starting at 342 nJ/cm², which becomes significant by 470 nJ/cm². Therefore during all optical experiments the fluence was kept at or below 257 nJ/cm² to be confident that the laser exposure was not degrading the sample.

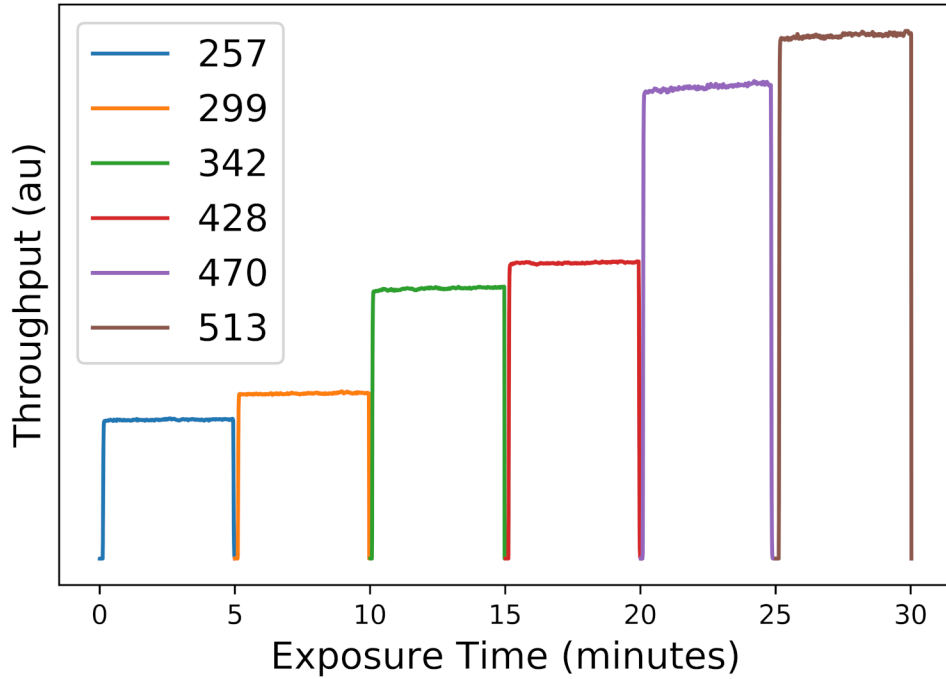


Figure 4.1: Results from the photo induced degradation test with a pulse energy of 2.21 eV, for various laser fluences in nJ/cm².

4.2 Differential Transmission

Prior to studying the carrier spin dynamics, it is essential to characterize the spin-independent carrier thermalization and recombination times. Figure 4.2 shows a typical graph for above bandgap excitation. Here the excitation photon energy is 38 meV above band gap. The data points prior to 0 delay indicate that the pump beam is arriving before the probe, and provides the base line for no change in the probes transmission. After zero delay the signal shows a fast (< 20 ps) decay indicating the carriers are undergoing intraband scattering processes. Over greater time scales the decay follows a second exponential indicating interband recombination. This is consistent with the theory laid out in section 1.5, where the lifetimes are found by fitting to equation 1.29. This yielded a carrier thermalization time of 18 ± 2 (ps) and a carrier recombination time of 160 ± 20 (ps). Therefore; the lifetime of the differential transmission signal was found to be less than the repetition rate of the source.

Figure 4.3 shows results of differential transmission measurements for various excitation energies. Figure 4.4 shows the height of the differential transmission signal

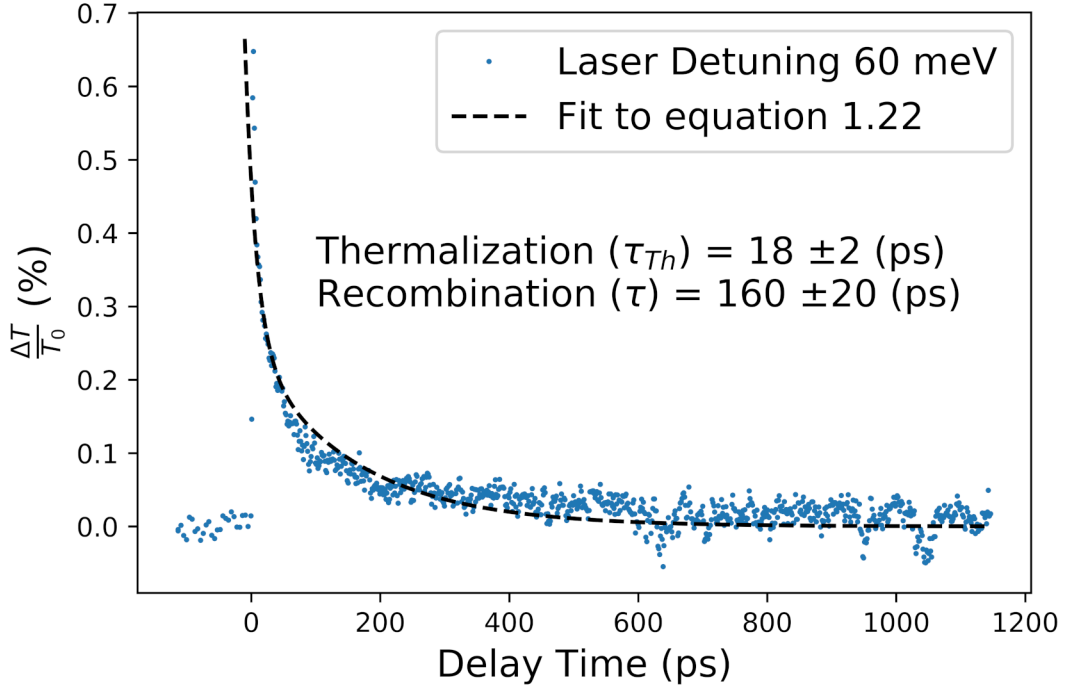


Figure 4.2: Results of differential transmission signal for 60 meV above gap excitation, 257 nJ/cm^2 . Fitting to equation 1.29, leads to a carrier thermalization time of 18 ± 2 and a carrier recombination time of 160 ± 20 .

at 50 ps as a function of laser detuning from the band edge, overlain with the linear absorption spectrum. The differential transmission is a measure of the change in the absorption coefficient at a particular probe energy due to the state filling induced by the carriers injected by the pump beam, while the linear absorption is simply a measure of the transmission of a broadband source. The differential transmission signal tracks the linear absorption through the excitonic peak ($\sim -100 \text{ meV}$) and decreases as the excitation energy is tuned towards the band edge. In the vicinity of the band edge we observe photoinduced absorption, this is due to the low absorption coefficient in this region coupled with the high excitation fluence. The presence of a high density of electron-hole pairs in the semiconductor leads to a slight reduction of the band gap due to the exchange interactions between electrons. This process, which is a manifestation of many body interactions, is referred to as band gap re-normalization. This results in the probe absorption increasing for energies in the vicinity of the band edge. As the excitation energy is tuned above the band edge there is a steep onset of signal up to $\sim 50 \text{ meV}$ above gap. It is typical for the differential transmission signal to

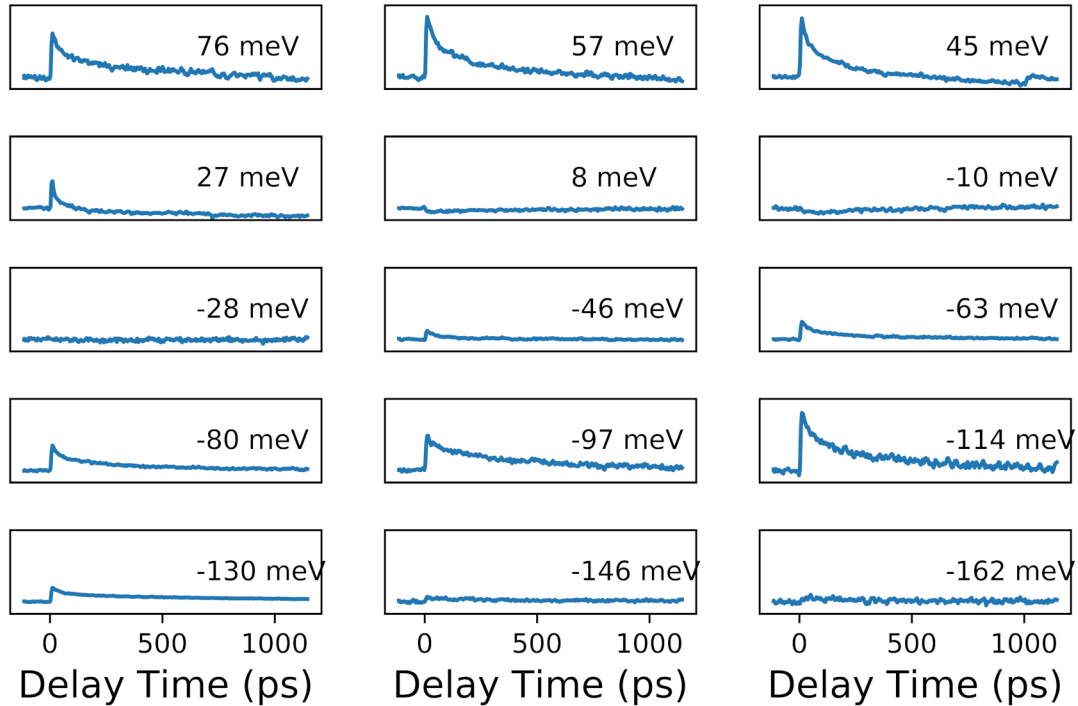


Figure 4.3: Results of differential transmission signal for various laser detunings at 257 nJ/cm^2 .

exhibit a sharper band edge than the linear absorption signal as the linear absorption is impacted not only by the state filling signal but also by scattering from roughness at the sample surface. The differential transmission then decreases as the laser is tuned above the band gap. This is due to the reduction in the absorption depth as the photon energy increases eventually getting smaller than the sample thickness.

4.3 Circular Dichroism

Typical circular dichroism results are shown in the upper panel of Figure 4.5 for a pump and probe beam with the same and opposite helicities, as a function of the delay time between pulses. In the case of the same helicity (blue curve) the signal is large in the vicinity of zero delay and follows an exponential trend over the first $\sim 15 \text{ ps}$. Here the probe is measuring the state filling response of the carriers with the same angular momentum as injected by the pump beam. In the case of opposite helicity (orange curve) the signal levels off quickly after zero delay. After $\sim 20 \text{ ps}$

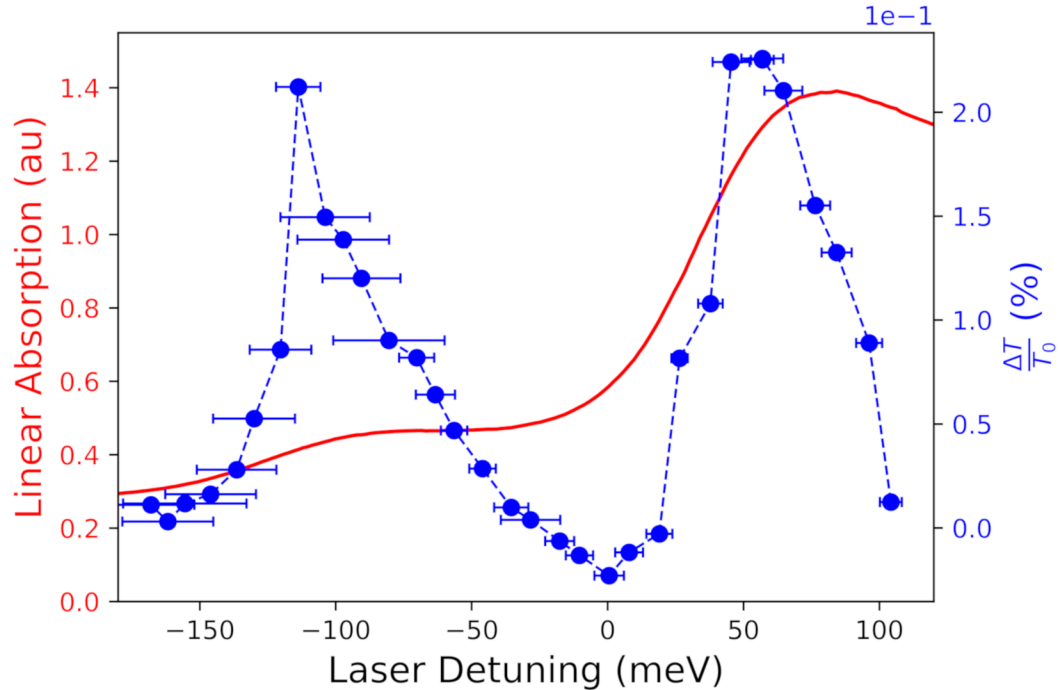


Figure 4.4: Magnitude of the differential transmission signal, at 50 ps, for various laser detunings at 257 nJ/cm^2 .

the signals are equivalent and begin to decay at the same rate. These observations are consistent with the theory laid out in section 1.5. The convergence of the blue and orange curve indicates the spin relaxation of the optically injected carriers. The lower panel in Figure 4.5 shows the degree of spin polarization as a function of delay. The degree of spin polarization in the vicinity of zero delay is $\sim 50\%$ and decays in a single exponential trend towards zero. Fitting this decay to equation 1.37 yields a intraband spin lifetime of $12 \pm 2 \text{ ps}$.

The process described above was carried out for various excitation energies and pulse fluences. Figure 4.6 shows the circular dichroism results for various excitation energies. At energies above gap the typical response for above band gap excitation is observed, as described above. As the energy is tuned below gap photoinduced absorption, tied to the band gap re-normalization, is observed as reflected by the fact that the differential transmission signal for the opposite helicity state dips below zero. As the excitation energy is tuned across the excitonic resonance the typical state filling response is recovered. This is summarized in the top panel of Figure 4.7 where

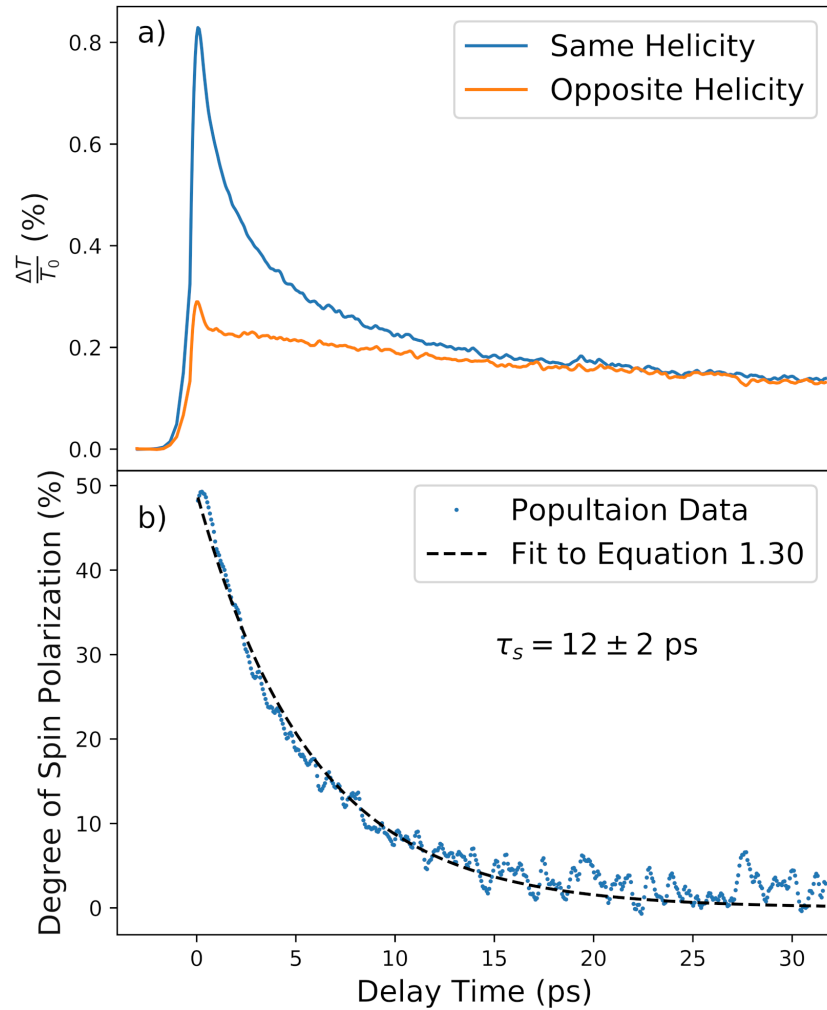


Figure 4.5: (a) Circular dichroism results for an excitation energy 38 meV above band gap, at a excitation fluence of 572 nJ/cm^2 . (b) Degree of spin polarization for the signal above, fit to equation 1.37 yields a spin lifetime of 12 ± 2 ps.

the degree of spin polarization at 3 ps is presented for various excitation energies. The spin polarization is greatest just above the band gap at 27 meV ($\sim 80\%$) and near the excitonic resonance at -114 meV ($\sim 55\%$). The lower panel of Figure 4.7 shows the spin lifetimes as a function of excitation energy. As the energy is tuned over the excitonic resonance the spin lifetime increases to a maximum at -104 meV then decreases rapidly as the energy is tuned towards the band edge. Although this transition is expected to be sharp, inhomogeneous broadening as a result of lattice distortions causes spectral broadening of the transition. The same feature was noticed

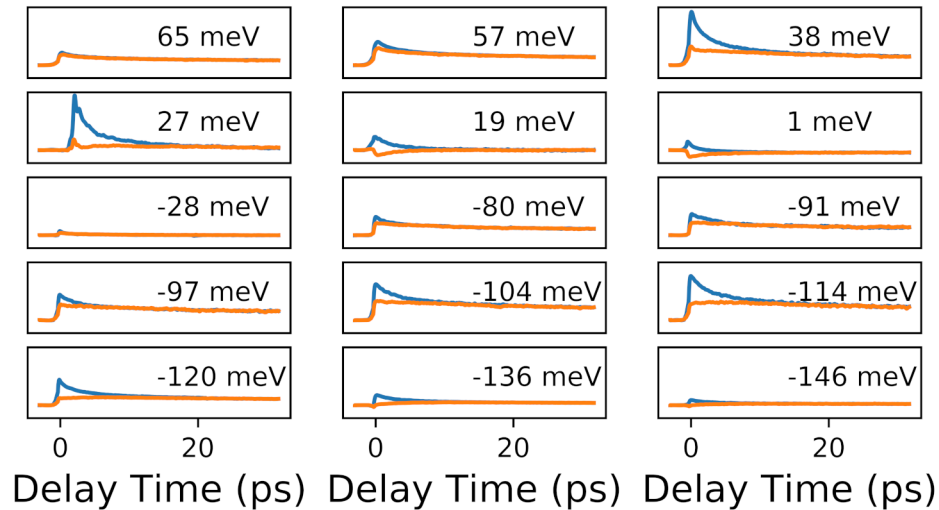


Figure 4.6: Circular dichroism results for various excitation energies referenced from the band edge, taken with a fluence of 572 nJ/cm^2 . Blue (orange) curves represent the same (opposite) helicity between the pump and probe pulses

in the BA series by Todd *et.al.* [45]. The lack of points around the band gap is due to the low degree of circular polarization at the band edge, making extraction of spin lifetimes impossible. Above gap we see a decrease in spin lifetime with increasing energy.

The Initial degree of spin polarization is high for probe energies just above the band gap (80%). This is consistent with the observations in MAPbI_3 by Giovanni *et.al.*, for which a polarization of 90% was observed [42]. A reduction in the degree of spin polarizations at high photon energies is consistent with the findings by Todd *et.al.* [45]. The observation of a high degree of polarization at the band edge indicates that the electrons and holes are both spin polarized immediately after excitation. This is because, according to equation 1.28 the bleaching signal has contributions from both electrons (via f_e) and holes (via f_h). Electronic structure calculations for a similar 2D perovskite ($n=1$, $(\text{C}_6\text{H}_5\text{C}_2\text{H}_4\text{NH}_3)_2\text{PbI}_4$) indicate a similar effective mass for electrons and holes [43]. This suggests that electrons and holes contribute to the bleaching signal to a similar extent. Nevertheless, the observation of a single exponential decay suggests that the spin lifetimes for the electrons and holes are similar.

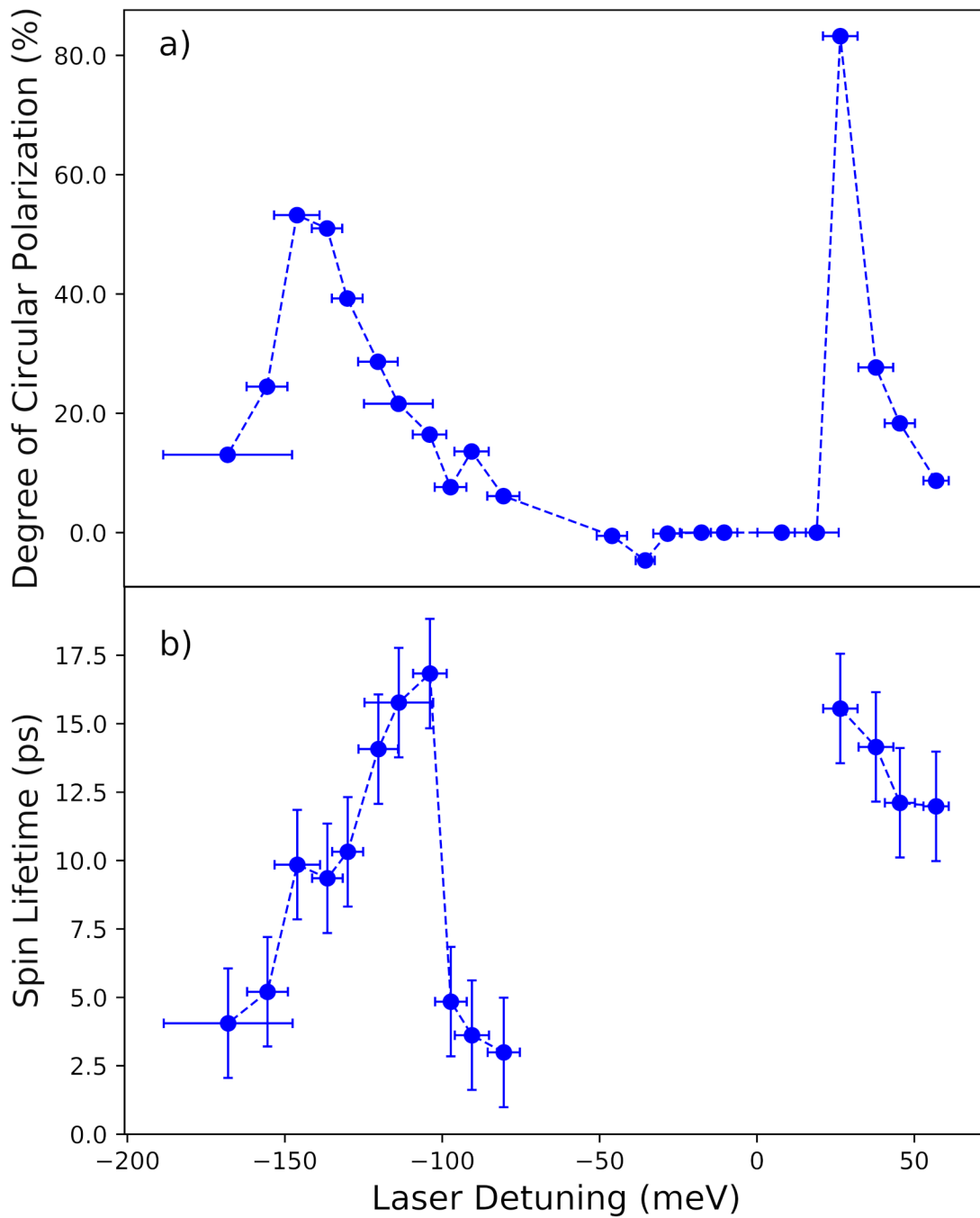


Figure 4.7: (a) Degree of circular polarization and (b) spin lifetime as a function of laser detuning, at 3 ps after zero delay for a fluence of $572 \text{ nJ}/\text{cm}^2$.

Figure 4.8 shows the spin lifetimes for various pulse fluences. The spin lifetime is observed to stay constant with changing excitation fluence over an order of magnitude.

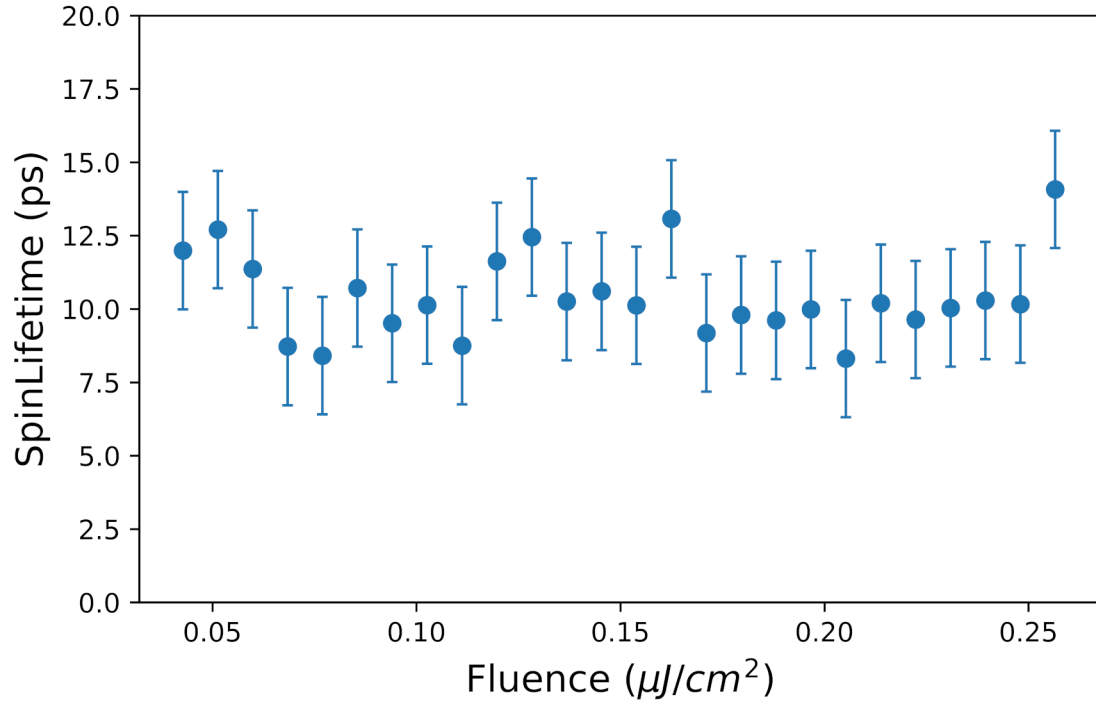


Figure 4.8: Spin lifetime as a function of laser excitation fluence at an excitation energy 38 meV above band gap.

We can gain insight into the carrier spin relaxation process from the lack of dependence of the lifetime on the carrier density. The two spin relaxation mechanisms discussed in section 2.2 (EY and DP) both depend on the momentum scattering time. Changing the optical pulse fluence changes the optically injected density of electron-hole pairs. The carriers within each band interact with each other through the Coulomb interaction, a process called carrier-carrier scattering. These scattering events change the wavevector of the scattered carriers. The trend in the spin lifetime versus carrier density therefore provides a means to distinguish between the EY and DP processes. For the EY mechanism, the spin lifetime should decrease with carrier density and for the DP mechanism the spin lifetime should increase with carrier density. The results shown in figure 4.8, which show no dependence on carrier density are therefore interesting.

In previous experiments carried out by a former graduate student on the 2D perovskite BA, the spin lifetime was observed to increase with increasing carrier density,

in contrast to the results shown in Figure 4.8 for 4AMP [54]. This indicates that changing the long spacer cation (from butylammonium to 4-amonomethyl piperidinium) has had a dramatic impact on the carrier spin dynamics. The increase in spin lifetime, observed in BA, indicated a dominance of the DP spin relaxation mechanism in that structure. As discussed in section 2.2, the DP mechanism is caused by the effective magnetic field induced by the spin-orbit interaction. For the BA structure, symmetry is broken in the stacking direction, reflecting the out of plane tilting of the lead iodide octahedra. This effective magnetic field is oriented in the plane of carrier transport (*i.e.* perpendicular to the stacking direction), with a direction that is perpendicular to \vec{k} . Since the laser pulse excites carriers with spin oriented along the stacking direction, this in plane effective magnetic field causes the carriers spins to precess, leading to spin relaxation. The spin lifetimes in the BA structure were used in reference [45] to obtain an estimate of the Rashba spin splitting, yielding a value that was 20 times larger than GaAs quantum wells, as expected from the strong SOC in perovskite materials.

Due to the strong spin orbit coupling in the 4AMP material a non-zero Rashba effective magnetic field is expected. The lack of a dependence of the spin lifetime on carrier density in the 4AMP structure studied in this thesis work could reflect a competition between the EY and DP mechanisms. However; an exact cancellation of the EY and DP processes would seem to an unlikely event.

An alternative explanation is provided by the symmetry of the effective magnetic field in the 4AMP film, which is expected to differ from the BA film. As shown in Figure 1.10 (a) the distortions of the lead iodide octahedra caused by the competition between the methylammonium and 4AMP cations corresponds to twisting, with no out of plane tilting. In this case, the symmetry breaking axis is in the plane perpendicular to the stacking axis. This leads to an effective magnetic field aligned with the stacking axis. Such a field, despite being non-zero, does not contribute to spin relaxation since no precession of the optically injected spins (also aligned with the stacking direction) occurs. A similar situation is expected to occur for BZ_2PbCl_4 as shown in Figure 4.9, adapted from reference [92]. The spin splitting associated with the Rashba effective magnetic field was found to be quite large in this material (with a $\lambda_R = 2 \text{ eV}\cdot\text{\AA}$) with the field aligned with the stacking axis. The preferred

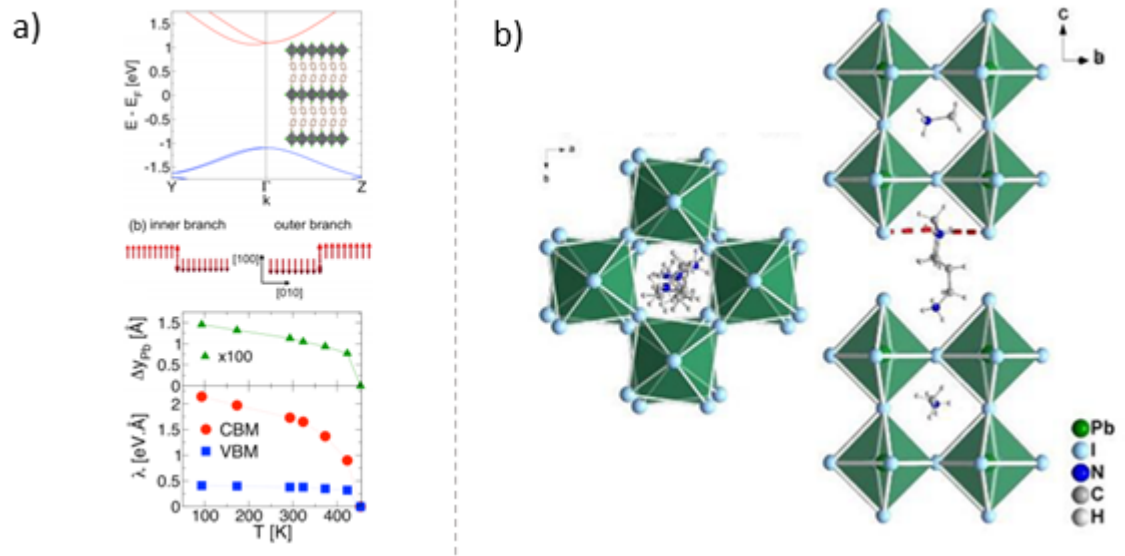


Figure 4.9: (a) Calculated band structure and associated Rashba coefficient for BZ_2PbCl_4 , adapted from reference [92]. (b) Molecular structure calculations for $(3AMP)MAPb_2I_7$, adapted from reference [70].

alignment of the Rashba effective magnetic field accounts for the lack of an observed dependence of the spin-relaxation on the carrier density in the experiments carried out for this thesis. Measurements on other 2D perovskites with differing choices of spacer molecule would provide further support of this interpretation and will be the subject of future work.

Chapter 5

Conclusion

In this thesis the spin dynamics of (4AMP)MAPb₂I₇ were studied using circular dichroism. A degree of spin polarization of 80% was observed and spin lifetimes of ~ 10 ps were measured at the band edge. The spin lifetime was observed to decrease with increasing energy above the band gap, and has no dependency on fluence. This result indicates that the D'yakonov-Perel mechanism for precessional spin relaxation is suppressed when compared to BA₂MAPb₂I₇. This contrast comes about due to the interaction of the spacer molecule with the perovskite lattice. In 4AMP the effective magnetic field due to the inversion asymmetry is in the stacking direction, causing no precession of the spins about the magnetic field. This differs from the BA case as the out of plane tilting of the perovskite octahedra causes an in place effective magnetic field about which the spins precess. The choice of spacer molecule in the 2D perovskite lattice, therefore provides an effective way to engineer the distortions in the perovskite octahedra.

A spin resonant tunnelling junction or a spin field effect transistor requires a material where the bulk inversion asymmetries is perpendicular to the spin-quantization axis, (as is the case in 4AMP). Therefore; a detailed understanding of the spacer molecule is crucial to the development of a perovskite based spintronic applications. This thesis covers only one potential spacer molecule and only one layer number for the perovskite crystal. As the functional space for creating these perovskite structures is vast, a more comprehensive study of the effect of spacer molecule is pertinent. Possible future works include substituting the spacer molecule for a longer organic chain, such as heptylamine (C₇H₁₇N) or for other aromatic organic chains such as 3-aminomethyl piperidinium (3AMP), (shown in Figure 4.9) which has been shown to cause even less distortions in the perovskite octahedra than the 4AMP case [72]. Further; to deal with the issue of toxicity, the lead atom in the perovskite lattice could be substituted with other group IV elements such as tin. The lower atomic number

of tin will decrease the effect of spin-orbit coupling, and possibly lead to longer spin lifetimes as well as contrasting relaxation dynamics.

The study of perovskite materials applicability to spintronic applications has been brought to the forefront of perovskite research through the investigation of the effect of spin-orbit coupling on the electronic and optoelectronic properties of perovskites. Potential spintronic applications are numerous, requiring differing material characteristics for each application. The strong spin orbit coupling combined with the low cost manufacturing and vast parameter space of perovskite crystals make the family of perovskite materials a strong candidate for spintronic applications.

Bibliography

- [1] A. Elasser and T. P. Chow. Silicon carbide benefits and advantages for power electronics circuits and systems. *Proceedings of the IEEE*, 90(6):969–986, June 2002.
- [2] Bernard Kippelen and Jean-Luc Brédas. Organic photovoltaics. *Energy & Environmental Science*, 2(3):251–261, 2009.
- [3] Akihiro Kojima, Kenjiro Teshima, Yasuo Shirai, Tsutomu Miyasaka. Organometal halide perovskites as visible-light sensitizers for photovoltaic cells. *Journal of American Chemical Society*, 131:6050–6051, 2009.
- [4] C.K. Moller. Crystal structure and photoconductivity of caesium plumbahalides. *Nature*, 182:1436, 1958.
- [5] AM Glazer. The classification of tilted octahedra in perovskites. *Acta Crystallographica Section B: Structural Crystallography and Crystal Chemistry*, 28(11):3384–3392, 1972.
- [6] Aurelien MA Leguy, Jarvist Moore Frost, Andrew P McMahon, Victoria Garcia Sakai, W Kockelmann, ChunHung Law, Xiaoe Li, Fabrizia Foglia, Aron Walsh, Brian C Oregan, et al. The dynamics of methylammonium ions in hybrid organic–inorganic perovskite solar cells. *Nature communications*, 6:7124, 2015.
- [7] Woon Seok Yang, Jun Hong Noh, Nam Joong Jeon, Young Chan Kim, Seungchan Ryu, Jangwon Seo, and Sang Il Seok. High-performance photovoltaic perovskite layers fabricated through intramolecular exchange. *Science*, 348(6240):1234–1237, 2015.
- [8] Guichuan Xing, Nirpan Mathews, Shuangyong Sun, Swee Sien Lim, Yeng Ming Lam, Michael Grätzel, Subodh Mhaisalkar, Tze Chein Sum. Long range balanced electron and hole transport lengths in organic-inorganic . *Science*, 342:344–347, 2013.
- [9] Jingshan Hou, Xin Yin, Yongzheng Fang, Fuqiang Huang, and Weizhong Jiang. Novel red-emitting perovskite-type phosphor $\text{Ca}_{1-x}\text{Mg}_x\text{O}_6:\text{Eu}^{3+}$ ($m = \text{nb, ta}$) for white led application. *Optical Materials*, 34(8):1394–1397, 2012.
- [10] N. Wu et al., October 27 2009. US Patent 7,608,467.
- [11] S. Liu et al., March 20 2001. US Patent 6,204,139.
- [12] D. Mitzi. *IBM J. of R and D*, 45(1):29–45, 2001.

- [13] P. Bijumon. *Japanese journal of applied physics*, 41(6R):3834, 2002.
- [14] P. Dereń. *J. Appl. Phys.*, 103(4):043102, 2008.
- [15] S. Yakunin. *Nature communications*, 6, 2015.
- [16] M. D. McGehee. Perovskite solar cells: Continuing to soar. *Nature Materials*, 13:845–846, 2014.
- [17] NREL Efficiency Chart. url = energy.gov/eere/solar/downloads/research-cell-efficiency-records. 2017.
- [18] D Basu, D Saha, and P Bhattacharya. Optical polarization modulation and gain anisotropy in an electrically injected spin laser. *Physical review letters*, 102(9):093904, 2009.
- [19] T Jungwirth, X Marti, P Wadley, and J Wunderlich. Antiferromagnetic spintronics. *Nature Nanotechnology*, 11(3):231, 2016.
- [20] O Gomonay, T Jungwirth, and J Sinova. Concepts of antiferromagnetic spintronics (phys. status solidi rrl 4/2017). *Physica Status Solidi Rapid Research Letters*, 11:1770319, 2017.
- [21] Ian Appelbaum, Biqin Huang, and Douwe J. Monsma. Electronic measurement and control of spin transport in silicon. *Nature*, 447(7142):295–298, May 2007.
- [22] B. T. Jonker, Y. D. Park, B. R. Bennett, H. D. Cheong, G. Kioseoglou, and A. Petrou. Robust electrical spin injection into a semiconductor heterostructure. *Phys. Rev. B*, 62:8180–8183, Sep 2000.
- [23] Sebastiaan van Dijken, Xin Jiang, and Stuart S. P. Parkin. Room temperature operation of a high output current magnetic tunnel transistor. *Applied Physics Letters*, 80(18):3364–3366, 2002.
- [24] Jacky Even, Laurent Pedesseau, Claudine Katan. Analysis of multivalley and multibandgap absorption and enhancement of free carriers related to exciton screening in hybrid perovskites. *The Journal of Physical Chemistry*, 118:11566–11572, 2014.
- [25] Yu A Bychkov and É I Rashba. Properties of a 2d electron gas with lifted spectral degeneracy. *JETP lett*, 39(2):78, 1984.
- [26] K. C. Hall, Wayne H. Lau, K. Gndodu, Michael E. Flatt, and Thomas F. Boggess. Nonmagnetic semiconductor spin transistor. *Applied Physics Letters*, 83(14):2937–2939, 2003.
- [27] Sebastiaan van Dijken, Xin Jiang, and Stuart S. P. Parkin. Room temperature operation of a high output current magnetic tunnel transistor. *Applied Physics Letters*, 80(18):3364–3366, 2002.

- [28] Yuji Nishikawa, Atsushi Tackeuchi, Satoshi Nakamura, Shunichi Muto, and Naoki Yokoyama. Alloptical picosecond switching of a quantum well etalon using spinpolarization relaxation. *Applied Physics Letters*, 66(7):839–841, 1995.
- [29] J. Rudolph, D. Hgele, H. M. Gibbs, G. Khitrova, and M. Oestreich. Laser threshold reduction in a spintronic device. *Applied Physics Letters*, 82(25):4516–4518, 2003.
- [30] Kimberley C. Hall and Michael E. Flatt. Performance of a spin-based insulated gate field effect transistor. *Applied Physics Letters*, 88(16):162503, 2006.
- [31] O. Gomonay, T. Jungwirth, and J. Sinova. Concepts of antiferromagnetic spintronics. *physica status solidi (RRL) Rapid Research Letters*, 11(4):1700022, 2017.
- [32] A. Imamoglu, D. D. Awschalom, G. Burkard, D. P. DiVincenzo, D. Loss, M. Sherwin, and A. Small. Quantum information processing using quantum dot spins and cavity qed. *Phys. Rev. Lett.*, 83:4204–4207, Nov 1999.
- [33] SA Wolf, DD Awschalom, RA Buhrman, JM Daughton, S Von Molnar, ML Roukes, A Yu Chtchelkanova, and DM Treger. Spintronics: a spin-based electronics vision for the future. *science*, 294(5546):1488–1495, 2001.
- [34] Ching Tsang, Robert E Fontana, Tsann Lin, David E Heim, Virgil S Speriosu, Bruce A Gurney, and Mason L Williams. Design, fabrication and testing of spin-valve read heads for high density recording. *IEEE Transactions on Magnetics*, 30(6):3801–3806, 1994.
- [35] S. Datta, B. Das. Electronic analog of the electro-optic modulator. *Applied Physics Letters*, 56:665–667, 1990.
- [36] Wikipedia contributors. Tunnel magnetoresistance — Wikipedia, the free encyclopedia, 2018. [Online; accessed 27-November-2018].
- [37] Muhammad Zahir Iqbal, Ghulam Hussain, Salma Siddique, and Muhammad Waqas Iqbal. Enhanced magnetoresistance in graphene spin valve. *Journal of Magnetism and Magnetic Materials*, 429:330–333, 2017.
- [38] H. Yokoi, S. Choowitsakunlert, K. Kobayashi, and K. Takagiwa. Optical isolator with si guiding layer fabricated by photosensitive adhesive bonding. In *Semiconductor Wafer Bonding: Science, Technology and Applications 14*, volume 75, pages 215–220. Electrochemical Society Inc., 2016.
- [39] Jing Li, Haixin Liu, Sayeef Salahuddin, and Kaushik Roy. Variation-tolerant spin-torque transfer (stt) mram array for yield enhancement. In *Custom Integrated Circuits Conference, 2008. CICC 2008. IEEE*, pages 193–196. IEEE, 2008.

- [40] Felix Meier and Boris Petrovich Zakharchenya. *Optical orientation*. Elsevier, 2012.
- [41] David D Awschalom, Daniel Loss, and Nitin Samarth. *Semiconductor spintronics and quantum computation*. Springer Science & Business Media, 2013.
- [42] David Giovanni, Hong Ma, Julianto Chua, Michael Grtzel, Ramamoorthy Ramesh, Subodh Mhaisalkar, Nripan Mathews, Tze Chien Sum. Highly spin-polarized carrier dynamics and ultralarge photoinduced magnetization in $\text{CH}_3\text{NH}_3\text{PbI}_3$ perovskite thin films. *Nano Letters*, 15:1553–1558, 2015.
- [43] Yaxin Zhai, Sangita Baniya, Chuang Zhang, Junwen Li, Paul Haney, Chuan-Xiang Sheng, Eitan Ehrenfreund, and Zeev Valy Vardeny. Giant rashba splitting in 2d organic-inorganic halide perovskites measured by transient spectroscopies. *Science Advances*, 3(7), 2017.
- [44] Patrick Odenthal, William Talmadge, Nathan Gundlach, Ruizhi Wang, Chuang Zhang, Dali Sun, Zhi-Gang Yu, Z Valy Vardeny, and Yan S Li. Spin-polarized exciton quantum beating in hybrid organic–inorganic perovskites. *Nature Physics*, 13(9):894, 2017.
- [45] S. B. Todd, D. B. Riley, A. Binai-Motlagh, C. Clegg, A. Ramachandran, S. A. March, I. G. Hill, C. C. Stoumpos, M. G. Kanatzidis, Z.-G. Yu, and K. C. Hall. Detection of Rashba spin splitting in 2D organic-inorganic perovskite via precessional carrier spin relaxation. *ArXiv e-prints*, July 2018.
- [46] Fan Zheng, Liang Z Tan, Shi Liu, and Andrew M Rappe. Rashba spin–orbit coupling enhanced carrier lifetime in $\text{ch}_3\text{nh}_3\text{pb}_3\text{i}_3$. *Nano letters*, 15(12):7794–7800, 2015.
- [47] Jacky Even, Laurent Pedesseau, Jean-Marc Jancu, and Claudine Katan. Importance of spinorbit coupling in hybrid organic/inorganic perovskites for photovoltaic applications. *The Journal of Physical Chemistry Letters*, 4(17):2999–3005, 2013.
- [48] Jacky Even, Laurent Pedesseau, M-A Dupertuis, J-M Jancu, and Claudine Katan. Electronic model for self-assembled hybrid organic/perovskite semiconductors: Reverse band edge electronic states ordering and spin-orbit coupling. *Physical Review B*, 86(20):205301, 2012.
- [49] L. Leppert, S. E. Reyes-Lillo, and J. B. Neaton. Electric field and strain induced Rashba effect in hybrid halide perovskites. *ArXiv e-prints*, August 2016.
- [50] Thibaud Etienne, Edoardo Mosconi, and Filippo De Angelis. Dynamical origin of the rashba effect in organohalide lead perovskites: A key to suppressed carrier recombination in perovskite solar cells? *The journal of physical chemistry letters*, 7(9):1638–1645, 2016.

- [51] Hsinhan Tsai, Wanyi Nie, Jean-Christophe Blancon, Constantinos C Stoumpos, Reza Asadpour, Boris Harutyunyan, Amanda J Neukirch, Rafael Verduzco, Jared J Crochet, Sergei Tretiak, Laurent Pedesseau, Jacky Even, Muhammad A Alam, Gautam Gupta, Jun Lou, Pulickel M Ajayan, Michael J Bedzyk, and Mercouri G Kanatzidis. High-efficiency two-dimensional ruddlesden-popper perovskite solar cells. *Nature*, 536(7616):312316, August 2016.
- [52] Charlotte Clegg and Ian G. Hill. Systematic study on the impact of water on the performance and stability of perovskite solar cells. *RSC Adv.*, 6:52448–52458, 2016.
- [53] Ian C. Smith, Eric T. Hoke, Diego Solis-Ibarra, Michael D. McGehee, and Hemamala I. Karunadasa. A layered hybrid perovskite solar-cell absorber with enhanced moisture stability. *Angewandte Chemie*, 126(42):11414–11417, 2014.
- [54] Seth Todd. Pump probe studies of spin dynamics in the 2d perovskite butylammonium methylammonium lead iodide. 2018.
- [55] Charles Kittel. *Introduction to Solid State Physics*. John Wiley & Sons, Inc., New York, 6th edition, 1986.
- [56] Khan MF Shahil and Alexander A Balandin. Thermal properties of graphene and multilayer graphene: Applications in thermal interface materials. *Solid State Communications*, 152(15):1331–1340, 2012.
- [57] Rashida Arsat, Michael Breedon, Mahnaz Shafiei, PG Spizziri, Scott Gilje, RB Kaner, Kouros Kalantar-zadeh, and Wojtek Wlodarski. Graphene-like nano-sheets for surface acoustic wave gas sensor applications. *Chemical Physics Letters*, 467(4-6):344–347, 2009.
- [58] Fanke Meng, Zhanglian Hong, James Arndt, Ming Li, Mingjia Zhi, Feng Yang, and Nianqiang Wu. Visible light photocatalytic activity of nitrogen-doped $\text{La}_2\text{Ti}_2\text{O}_7$ nanosheets originating from band gap narrowing. *Nano Research*, 5(3):213–221, 2012.
- [59] Alfredo M Morales and Charles M Lieber. A laser ablation method for the synthesis of crystalline semiconductor nanowires. *Science*, 279(5348):208–211, 1998.
- [60] Lionel Vayssieres. Growth of arrayed nanorods and nanowires of zno from aqueous solutions. *Advanced Materials*, 15(5):464–466, 2003.
- [61] J Tersoff, Ch Teichert, and MG Lagally. Self-organization in growth of quantum dot superlattices. *Physical Review Letters*, 76(10):1675, 1996.
- [62] Sarbajit Banerjee and Stanislaus S Wong. In situ quantum dot growth on multiwalled carbon nanotubes. *Journal of the American Chemical Society*, 125(34):10342–10350, 2003.

- [63] Arthur J Nozik, Matthew C Beard, Joseph M Luther, Matt Law, Randy J Ellingson, and Justin C Johnson. Semiconductor quantum dots and quantum dot arrays and applications of multiple exciton generation to third-generation photovoltaic solar cells. *Chemical reviews*, 110(11):6873–6890, 2010.
- [64] Julien Claudon, Joël Bleuse, Nitin Singh Malik, Maela Bazin, Périne Jaffrennou, Niels Gregersen, Christophe Sauvan, Philippe Lalanne, and Jean-Michel Gérard. A highly efficient single-photon source based on a quantum dot in a photonic nanowire. *Nature Photonics*, 4(3):174, 2010.
- [65] Daniel Loss and David P DiVincenzo. Quantum computation with quantum dots. *Physical Review A*, 57(1):120, 1998.
- [66] M Kalin, J Kogovšek, and M Remškar. Mechanisms and improvements in the friction and wear behavior using mos2 nanotubes as potential oil additives. *Wear*, 280:36–45, 2012.
- [67] Sanghyun Ju, Antonio Facchetti, Yi Xuan, Jun Liu, Fumiaki Ishikawa, Peide Ye, Chongwu Zhou, Tobin J Marks, and David B Janes. Fabrication of fully transparent nanowire transistors for transparent and flexible electronics. *Nature nanotechnology*, 2(6):378, 2007.
- [68] P Tongying, F Vietmeyer, D Aleksasuk, GJ Ferraudi, G Krylova, and M Kuno. Double heterojunction nanowire photocatalysts for hydrogen generation. *Nanoscale*, 6(8):4117–4124, 2014.
- [69] Seth Coe-Sullivan, Wenhao Liu, Peter Allen, and Jonathan S Steckel. Quantum dots for led downconversion in display applications. *ECS Journal of Solid State Science and Technology*, 2(2):R3026–R3030, 2013.
- [70] Lingling Mao, Weijun Ke, Laurent Pedesseau, Yilei Wu, Claudine Katan, Jacky Even, Michael R Wasielewski, Constantinos C Stoumpos, and Mercuri G Kanatzidis. Hybrid dion–jacobson 2d lead iodide perovskites. *Journal of the American Chemical Society*, 140(10):3775–3783, 2018.
- [71] Hartmut Haug and Stephan W Koch. *Quantum Theory of the Optical and Electronic Properties of Semiconductors: Fifth Edition*. World Scientific Publishing Company, 2009.
- [72] Chan Myae Myae Soe, Constantinos C. Stoumpos, Mikal Kepenekian, Boubacar Traor, Hsinhan Tsai, Wanyi Nie, Binghao Wang, Claudine Katan, Ram Seshadri, Aditya D. Mohite, Jacky Even, Tobin J. Marks, and Mercuri G. Kanatzidis. New type of 2d perovskites with alternating cations in the interlayer space, $(\text{c}(\text{nh}_2)_3)(\text{ch}_3\text{nh}_3)\text{npbni}_{3n+1}$: Structure, properties, and photovoltaic performance. *Journal of the American Chemical Society*, 139(45):16297–16309, 2017. PMID: 29095597.

- [73] Samuel A March, Charlotte Clegg, Drew B Riley, Daniel Webber, Ian G Hill, and Kimberley C Hall. Simultaneous observation of free and defect-bound excitons in $\text{CH}_3\text{NH}_3\text{PbI}_3$ using four-wave mixing spectroscopy. *Scientific Reports*, 6:39139, 2016.
- [74] Julian Burschka, Norman Pellet, Soo-Jin Moon, Robin Humphry-Baker, Peng Gao, Peng Gao, Mohammad K Nazeeruddin, and Michael Grätzel. Sequential deposition as a route to high-performance perovskite-sensitized solar cells. *Nature*, 499(7458):316319, July 2013.
- [75] Jong H. Kim, Spencer T. Williams, Namchul Cho, Chu-Chen Chueh, and Alex K.-Y. Jen. Enhanced environmental stability of planar heterojunction perovskite solar cells based on blade-coating. *Advanced Energy Materials*, 5(4):1401229, 2015.
- [76] Sanjib Das, Bin Yang, Gong Gu, Pooran C. Joshi, Ilia N. Ivanov, Christopher M. Rouleau, Tolga Aytug, David B. Geohegan, and Kai Xiao. High-performance flexible perovskite solar cells by using a combination of ultrasonic spray-coating and low thermal budget photonic curing. *ACS Photonics*, 2(6):680–686, 2015.
- [77] Jing Cao, Binghui Wu, Ruihao Chen, Youyunqi Wu, Yong Hui, Bing-Wei Mao, and Nanfeng Zheng. Efficient, hysteresis-free, and stable perovskite solar cells with ZnO as electron-transport layer: Effect of surface passivation. *Advanced Materials*, 30(11):1705596.
- [78] Dongqin Bi, Lei Yang, Gerrit Boschloo, Anders Hagfeldt, and Erik M.J. Johansson. Effect of different hole transport materials on recombination in $\text{CH}_3\text{NH}_3\text{PbI}_3$ perovskite-sensitized mesoscopic solar cells. *The journal of physical chemistry letters*, 4(9):1532–1536, 2013.
- [79] Michael M Lee, Joël Teuscher, Tsutomu Miyasaka, Takuro N Murakami, and Henry J Snaith. Efficient hybrid solar cells based on meso-superstructured organometal halide perovskites. *Science*, 338(6107):643–647, 2012.
- [80] Chun-Yu Chang, Cheng-Ya Chu, Yu-Ching Huang, Chien-Wen Huang, Shuang-Yuan Chang, Chien-An Chen, Chi-Yang Chao, and Wei-Fang Su. Tuning perovskite morphology by polymer additive for high efficiency solar cell. *ACS applied materials & interfaces*, 7(8):4955–4961, 2015.
- [81] Hui-Seon Kim, Chang-Ryul Lee, Jeong-Hyeok Im, Ki-Beom Lee, Thomas Moehl, Arianna Marchioro, Soo-Jin Moon, Robin Humphry-Baker, Jun-Ho Yum, Jacques E Moser, et al. Lead iodide perovskite sensitized all-solid-state submicron thin film mesoscopic solar cell with efficiency exceeding 9%. *Scientific reports*, 2, 2012.
- [82] Michael M. Lee, Joël Teuscher, Tsutomu Miyasaka, Takuro N. Murakami, and Henry J. Snaith. Efficient hybrid solar cells based on meso-superstructured organometal halide perovskites. *Science*, 2012.

- [83] Namyoung Ahn, Dae-Yong Son, In-Hyuk Jang, Seong Min Kang, Mansoo Choi, and Nam-Gyu Park. Highly reproducible perovskite solar cells with average efficiency of 18.3% and best efficiency of 19.7% fabricated via lewis base adduct of lead(ii) iodide. *Journal of the American Chemical Society*, 137(27):8696–8699, 2015. PMID: 26125203.
- [84] Jin-Wook Lee, Hui-Seon Kim, and Nam-Gyu Park. Lewis acidbase adduct approach for high efficiency perovskite solar cells. *Accounts of Chemical Research*, 49(2):311–319, 2016. PMID: 26797391.
- [85] Maria Konstantakou and Thomas Stergiopoulos. A critical review on tin halide perovskite solar cells. *Journal of Materials Chemistry A*, 5(23):11518–11549, 2017.
- [86] J-C Blancon, AV Stier, H Tsai, W Nie, CC Stoumpos, B Traor, L Pedesseau, M Kepenekian, F Katsutani, GT Noe, J Kono, S Tretiak, SA Crooker, C Katan, MG Kanatzidis, JJ Crochet, J Even, and AD Mohite. Scaling law for excitons in 2d perovskite quantum wells. *Nature communications*, 9(1):2254, June 2018.
- [87] Duyen H. Cao, Constantinos C. Stoumpos, Omar K. Farha, Joseph T. Hupp, and Mercuri G. Kanatzidis. 2d homologous perovskites as light-absorbing materials for solar cell applications. *Journal of the American Chemical Society*, 137(24):7843–7850, 2015. PMID: 26020457.
- [88] Rebecca L. Milot, Rebecca J. Sutton, Giles E. Eperon, Amir Abbas Haghighirad, Josue Martinez Hardigree, Laura Miranda, Henry J. Snaith, Michael B. Johnston, and Laura M. Herz. Charge-carrier dynamics in 2d hybrid metal-halide perovskites. *Nano Letters*, 16(11):7001–7007, 2016. PMID: 27689536.
- [89] Mara C. Glvez-Rueda, Eline M. Hutter, Duyen H. Cao, Nicolas Renaud, Constantinos C. Stoumpos, Joseph T. Hupp, Tom J. Savenije, Mercuri G. Kanatzidis, and Ferdinand C. Grozema. Interconversion between free charges and bound excitons in 2d hybrid lead halide perovskites. *The Journal of Physical Chemistry C*, 121(47):26566–26574, 2017.
- [90] T Umabayashi, K Asai, T Kondo, and A Nakao. Electronic structures of lead iodide based low-dimensional crystals. *Physical Review B*, 67(15):155405, 2003.
- [91] Minsung Kim, Jino Im, Arthur J Freeman, Jisoon Ihm, and Hosub Jin. Switchable $s = 1/2$ and $j = 1/2$ rashba bands in ferroelectric halide perovskites. *Proceedings of the National Academy of Sciences*, page 201405780, 2014.
- [92] Mikal Kepenekian, Roberto Robles, Claudine Katan, Daniel Saponi, Laurent Pedesseau, and Jacky Even. Rashba and dresselhaus effects in hybrid organo-inorganic perovskites: From basics to devices. *ACS Nano*, 9(12):11557–11567, 2015. PMID: 26348023.


- [93] K Ishizaka, MS Bahramy, H Murakawa, M Sakano, T Shimojima, T Sonobe, K Koizumi, S Shin, H Miyahara, A Kimura, et al. Giant rashba-type spin splitting in bulk bitei. *Nature materials*, 10(7):521, 2011.
- [94] Z. Guo, J. S. Manser, Y. Wan, P. V. Kamat, and L. Huang. Spatial and temporal imaging of long-range charge transport in perovskite thin films by ultrafast microscopy. *Nature Communications*, 6:7471, jun 2015.
- [95] Joseph S Manser and Prashant V Kamat. Band filling with free charge carriers in organometal halide perovskites. *Nature Photonics*, 8(9):737, 2014.
- [96] Arianna Marchioro, Joël Teuscher, Dennis Friedrich, Marinus Kunst, Roel Van De Krol, Thomas Moehl, Michael Grätzel, and Jacques-E Moser. Unravelling the mechanism of photoinduced charge transfer processes in lead iodide perovskite solar cells. *Nature photonics*, 8(3):250, 2014.
- [97] Wanyi Nie, Hsinhan Tsai, Reza Asadpour, Jean-Christophe Blancon, Amanda J Neukirch, Gautam Gupta, Jared J Crochet, Manish Chhowalla, Sergei Tretiak, Muhammad A Alam, et al. High-efficiency solution-processed perovskite solar cells with millimeter-scale grains. *Science*, 347(6221):522–525, 2015.
- [98] Daniel Niesner, Max Wilhelm, Ievgen Levchuk, Andres Osvet, Shreetu Shrestha, Mirosław Batentschuk, Christoph Brabec, and Thomas Fauster. Giant rashba splitting in $\text{CH}_3\text{NH}_3\text{PbBr}_3$ organic-inorganic perovskite. *Physical review letters*, 117(12):126401, 2016.
- [99] K. Hall, K. Gündoğdu, J.L. Hicks, A.N. Kocbay, T.F. Boggess, K. Holabird, A. Hunter, D.H. Chow, J.J. Zinck. Room-temperature electric-field controlled spin dynamics in (110) InAs quantum wells. *Applied Physics Letters*, 86:202114–1,202114–3, 2005.
- [100] Chuang Zhang, Dali Sun, and Z Valy Vardeny. Multifunctional optoelectronic–spintronic device based on hybrid organometal trihalide perovskites. *Advanced Electronic Materials*, 3(2):1600426, 2017.
- [101] Takeshi Kataoka, Takashi Kondo, Ryoichi Ito, Satoshi Sasaki, Kazuhito Uchida, and Noboru Miura. Magneto-optical study on excitonic spectra in $(\text{C}_6\text{H}_{13}\text{NH}_3)_2\text{PbI}_4$. *Phys. Rev. B*, 47:2010–2018, Jan 1993.
- [102] Gene Dresselhaus. Spin-orbit coupling effects in zinc blende structures. *Physical Review*, 100(2):580, 1955.
- [103] K. C. Hall, E. J. Koerperick, Thomas F. Boggess, O. B. Shchekin, and D. G. Deppe. Hole spin relaxation in neutral ingaas quantum dots: Decay to dark states. *Applied Physics Letters*, 90(5):053109, 2007.
- [104] J. J. Zinck, D. H. Chow, K. S. Holabird, J. N. Schulman, K. C. Hall, and T. F. Boggess. Resonant tunneling in (110) oriented interband diodes. *Applied Physics Letters*, 86(7):073502, 2005.


Appendix A

Rights and Permissions


A.1 Figure 1.10 and Figure 4.9 (b) and Figure 2.2 (c)

11/26/2018 Rightslink® by Copyright Clearance Center

 **Copyright Clearance Center**

 **RightsLink®**

[Home](#) [Create Account](#) [Help](#)

 **ACS Publications**
Most Trusted. Most Cited. Most Read.

Title: Hybrid Dion–Jacobson 2D Lead Iodide Perovskites

Author: Lingling Mao, Weijun Ke, Laurent Pedesseau, et al

Publication: Journal of the American Chemical Society

Publisher: American Chemical Society

Date: Mar 1, 2018

Copyright © 2018, American Chemical Society

LOGIN

If you're a [copyright.com](#) user, you can login to RightsLink using your copyright.com credentials. Already a [RightsLink user](#) or want to [learn more?](#)

PERMISSION/LICENSE IS GRANTED FOR YOUR ORDER AT NO CHARGE

This type of permission/license, instead of the standard Terms & Conditions, is sent to you because no fee is being charged for your order. Please note the following:

- Permission is granted for your request in both print and electronic formats, and translations.
- If figures and/or tables were requested, they may be adapted or used in part.
- Please print this page for your records and send a copy of it to your publisher/graduate school.
- Appropriate credit for the requested material should be given as follows: "Reprinted (adapted) with permission from (COMPLETE REFERENCE CITATION). Copyright (YEAR) American Chemical Society." Insert appropriate information in place of the capitalized words.
- One-time permission is granted only for the use specified in your request. No additional uses are granted (such as derivative works or other editions). For any other uses, please submit a new request.

If credit is given to another source for the material you requested, permission must be obtained from that source.

[BACK](#)

[CLOSE WINDOW](#)

Copyright © 2018 [Copyright Clearance Center, Inc.](#) All Rights Reserved. [Privacy statement](#). [Terms and Conditions](#). Comments? We would like to hear from you. E-mail us at customercare@copyright.com

A.2 Figure 1.4 (b)

11/28/2018

Rightslink® by Copyright Clearance Center



RightsLink®

Home

Account
Info

Help



Title: Enhanced magnetoresistance in graphene spin valve

Author: Muhammad Zahir Iqbal, Ghulam Hussain, Salma Siddique, Muhammad Waqas Iqbal

Publication: Journal of Magnetism and Magnetic Materials

Publisher: Elsevier

Date: 1 May 2017

© 2017 Elsevier B.V. All rights reserved.

Logged in as:

Drew Riley
Dalhousie University

LOGOUT

Order Completed

Thank you for your order.

This Agreement between Dalhousie University -- Drew Riley ("You") and Elsevier ("Elsevier") consists of your license details and the terms and conditions provided by Elsevier and Copyright Clearance Center.

Your confirmation email will contain your order number for future reference.

[printable details](#)

License Number	4477780883469
License date	Nov 28, 2018
Licensed Content Publisher	Elsevier
Licensed Content Publication	Journal of Magnetism and Magnetic Materials
Licensed Content Title	Enhanced magnetoresistance in graphene spin valve
Licensed Content Author	Muhammad Zahir Iqbal, Ghulam Hussain, Salma Siddique, Muhammad Waqas Iqbal
Licensed Content Date	1 May 2017
Licensed Content Volume	429
Licensed Content Issue	n/a
Licensed Content Pages	4
Type of Use	reuse in a thesis/dissertation
Portion	figures/tables/illustrations
Number of figures/tables/illustrations	1
Format	both print and electronic
Are you the author of this Elsevier article?	No
Will you be translating?	No
Original figure numbers	1a
Title of your thesis/dissertation	Spin-Dynamics is Halide Perovskites
Expected completion date	Dec 2018
Estimated size (number of pages)	60
Requestor Location	Dalhousie University 6310 coburg dr Halifax, NS B3L5v9

A.3 Figure 1.4 (d)

11/28/2018

Rightslink® by Copyright Clearance Center



RightsLink®

Home

Create Account

Help



Title: Variation-tolerant Spin-Torque Transfer (STT) MRAM array for yield enhancement

Conference Proceedings: 2008 IEEE Custom Integrated Circuits Conference

Author: Jing Li

Publisher: IEEE

Date: Sept. 2008

Copyright © 2008, IEEE

LOGIN

If you're a **copyright.com user**, you can login to RightsLink using your copyright.com credentials. Already a **RightsLink user** or want to [learn more?](#)

Thesis / Dissertation Reuse

The IEEE does not require individuals working on a thesis to obtain a formal reuse license, however, you may print out this statement to be used as a permission grant:

Requirements to be followed when using any portion (e.g., figure, graph, table, or textual material) of an IEEE copyrighted paper in a thesis:

- 1) In the case of textual material (e.g., using short quotes or referring to the work within these papers) users must give full credit to the original source (author, paper, publication) followed by the IEEE copyright line © 2011 IEEE.
- 2) In the case of illustrations or tabular material, we require that the copyright line © [Year of original publication] IEEE appear prominently with each reprinted figure and/or table.
- 3) If a substantial portion of the original paper is to be used, and if you are not the senior author, also obtain the senior author's approval.

Requirements to be followed when using an entire IEEE copyrighted paper in a thesis:

- 1) The following IEEE copyright/ credit notice should be placed prominently in the references: © [year of original publication] IEEE. Reprinted, with permission, from [author names, paper title, IEEE publication title, and month/year of publication]
- 2) Only the accepted version of an IEEE copyrighted paper can be used when posting the paper or your thesis on-line.
- 3) In placing the thesis on the author's university website, please display the following message in a prominent place on the website: In reference to IEEE copyrighted material which is used with permission in this thesis, the IEEE does not endorse any of [university/educational entity's name goes here]'s products or services. Internal or personal use of this material is permitted. If interested in reprinting/republishing IEEE copyrighted material for advertising or promotional purposes or for creating new collective works for resale or redistribution, please go to http://www.ieee.org/publications_standards/publications/rights/rights_link.html to learn how to obtain a License from RightsLink.

If applicable, University Microfilms and/or ProQuest Library, or the Archives of Canada may supply single copies of the dissertation.

BACK

CLOSE WINDOW

Copyright © 2018 [Copyright Clearance Center, Inc.](#) All Rights Reserved. [Privacy statement](#). [Terms and Conditions](#). Comments? We would like to hear from you. E-mail us at customercare@copyright.com

A.4 Figure 1.14

12/12/2018 Rightslink® by Copyright Clearance Center



Copyright
Clearance
Center



[Home](#) [Create Account](#) [Help](#)



ACS Publications
Most Trusted. Most Cited. Most Read.

Title: Importance of Spin–Orbit Coupling in Hybrid Organic/Inorganic Perovskites for Photovoltaic Applications

Author: Jacky Even, Laurent Pedesseau, Jean-Marc Jancu, et al

Publication: Journal of Physical Chemistry Letters

Publisher: American Chemical Society

Date: Sep 1, 2013

Copyright © 2013, American Chemical Society

LOGIN

If you're a **copyright.com user**, you can login to RightsLink using your copyright.com credentials. Already a **RightsLink user** or want to [learn more?](#)

PERMISSION/LICENSE IS GRANTED FOR YOUR ORDER AT NO CHARGE

This type of permission/license, instead of the standard Terms & Conditions, is sent to you because no fee is being charged for your order. Please note the following:

- Permission is granted for your request in both print and electronic formats, and translations.
- If figures and/or tables were requested, they may be adapted or used in part.
- Please print this page for your records and send a copy of it to your publisher/graduate school.
- Appropriate credit for the requested material should be given as follows: "Reprinted (adapted) with permission from (COMPLETE REFERENCE CITATION). Copyright (YEAR) American Chemical Society." Insert appropriate information in place of the capitalized words.
- One-time permission is granted only for the use specified in your request. No additional uses are granted (such as derivative works or other editions). For any other uses, please submit a new request.

If credit is given to another source for the material you requested, permission must be obtained from that source.

[BACK](#)
[CLOSE WINDOW](#)

Copyright © 2018 [Copyright Clearance Center, Inc.](#) All Rights Reserved. [Privacy statement.](#) [Terms and Conditions.](#) Comments? We would like to hear from you. E-mail us at customercare@copyright.com

A.5 Figure 1.15 (a)



12-Dec-2018

This license agreement between the American Physical Society ("APS") and Drew Riley ("You") consists of your license details and the terms and conditions provided by the American Physical Society and SciPris.

Licensed Content Information

License Number:	RNP/18/DEC/010280
License date:	12-Dec-2018
DOI:	10.1103/PhysRevLett.117.126401
Title:	Giant Rashba Splitting in $S_{\text{CH}_3\text{NH}_3}\text{PbBr}_3$ Organic-Inorganic Perovskite
Author:	Daniel Niesner et al.
Publication:	Physical Review Letters
Publisher:	American Physical Society
Cost:	USD \$ 0.00

Request Details

Does your reuse require significant modifications:	No
Specify intended distribution locations:	Worldwide
Reuse Category:	Reuse in a thesis/dissertation
Requestor Type:	Academic Institution
Items for Reuse:	Figures/Tables
Number of Figure/Tables:	1
Figure/Tables Details:	Figure 1 d and e
Format for Reuse:	Print and Electronic
Total number of print copies:	Up to 1000

Information about New Publication:

University/Publisher:	Dalhousie University
Title of dissertation/thesis:	Circular Dichroism Studies of Spin Dynamics in (4AMP)MAPb2I7 Quantum Wells.
Author(s):	Drew Riley
Expected completion date:	Dec. 2018

License Requestor Information

Name:	Drew Riley
Affiliation:	Individual
Email Id:	drewbriley@gmail.com
Country:	Canada

A.6 Figure 1.17

11/28/2018

Rightslink® by Copyright Clearance Center

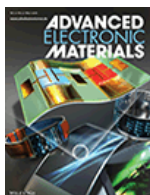


RightsLink®

Home

Account
Info

Help



Title: Multifunctional Optoelectronic–Spintronic Device Based on Hybrid Organometal Trihalide Perovskites

Author: Chuang Zhang, Dali Sun, Z. Vally Vardeny

Publication: Advanced Electronic Materials

Publisher: John Wiley and Sons

Date: Jan 17, 2017

Copyright © 2017, John Wiley and Sons

Logged in as:
Drew Riley
Dalhousie University

LOGOUT

Order Completed

Thank you for your order.

This Agreement between Dalhousie University -- Drew Riley ("You") and John Wiley and Sons ("John Wiley and Sons") consists of your license details and the terms and conditions provided by John Wiley and Sons and Copyright Clearance Center.

Your confirmation email will contain your order number for future reference.

[printable details](#)

License Number	4477781133239
License date	Nov 28, 2018
Licensed Content Publisher	John Wiley and Sons
Licensed Content Publication	Advanced Electronic Materials
Licensed Content Title	Multifunctional Optoelectronic–Spintronic Device Based on Hybrid Organometal Trihalide Perovskites
Licensed Content Author	Chuang Zhang, Dali Sun, Z. Vally Vardeny
Licensed Content Date	Jan 17, 2017
Licensed Content Volume	3
Licensed Content Issue	2
Licensed Content Pages	7
Type of use	Dissertation/Thesis
Requestor type	University/Academic
Format	Print and electronic
Portion	Figure/table
Number of figures/tables	1
Original Wiley figure/table number(s)	1
Will you be translating?	No
Title of your thesis / dissertation	Spin-Dynamics is Halide Perovskites
Expected completion date	Dec 2018
Expected size (number of pages)	60
Requestor Location	Dalhousie University 6310 coburg dr

<https://s100.copyright.com/AppDispatchServlet>

1/2

A.7 Figure 2.2 (a) and (b)



12-Dec-2018

This license agreement between the American Physical Society ("APS") and Drew Riley ("You") consists of your license details and the terms and conditions provided by the American Physical Society and SciPris.

Licensed Content Information

License Number:	RNP/18/DEC/010278
License date:	12-Dec-2018
DOI:	10.1103/PhysRevB.86.205301
Title:	Electronic model for self-assembled hybrid organic/perovskite semiconductors: Reverse band edge electronic states ordering and spin-orbit coupling
Author:	J. Even et al.
Publication:	Physical Review B
Publisher:	American Physical Society
Cost:	USD \$ 0.00

Request Details

Does your reuse require significant modifications:	No
Specify intended distribution locations:	Worldwide
Reuse Category:	Reuse in a thesis/dissertation
Requestor Type:	Academic Institution
Items for Reuse:	Figures/Tables
Number of Figure/Tables:	1
Figure/Tables Details:	Figure 3 a and b
Format for Reuse:	Print and Electronic
Total number of print copies:	Up to 1000

Information about New Publication:

University/Publisher:	Dalhousie University
Title of dissertation/thesis:	Circular Dichroism Studies of Spin Dynamics in (4AMP)MAPb2I7 Quantum Wells.
Author(s):	Drew Riley
Expected completion date:	Dec. 2018

License Requester Information

Name:	Drew Riley
Affiliation:	Individual
Email Id:	drewbriley@gmail.com
Country:	Canada

A.8 Figure 3.3 (b) and (c)

12/12/2018

Rightslink® by Copyright Clearance Center



RightsLink®

Home

Create Account

Help

ACS Publications
Most Trusted. Most Cited. Most Read.

Title: 2D Homologous Perovskites as Light-Absorbing Materials for Solar Cell Applications

Author: Duyen H. Cao, Constantinos C. Stoumpos, Omar K. Farha, et al

Publication: Journal of the American Chemical Society

Publisher: American Chemical Society

Date: Jun 1, 2015

Copyright © 2015, American Chemical Society

LOGIN

If you're a **copyright.com user**, you can login to RightsLink using your copyright.com credentials. Already a **RightsLink user** or want to [learn more?](#)

PERMISSION/LICENSE IS GRANTED FOR YOUR ORDER AT NO CHARGE

This type of permission/license, instead of the standard Terms & Conditions, is sent to you because no fee is being charged for your order. Please note the following:

- Permission is granted for your request in both print and electronic formats, and translations.
- If figures and/or tables were requested, they may be adapted or used in part.
- Please print this page for your records and send a copy of it to your publisher/graduate school.
- Appropriate credit for the requested material should be given as follows: "Reprinted (adapted) with permission from (COMPLETE REFERENCE CITATION). Copyright (YEAR) American Chemical Society." Insert appropriate information in place of the capitalized words.
- One-time permission is granted only for the use specified in your request. No additional uses are granted (such as derivative works or other editions). For any other uses, please submit a new request.

If credit is given to another source for the material you requested, permission must be obtained from that source.

BACK

CLOSE WINDOW

Copyright © 2018 [Copyright Clearance Center, Inc.](#) All Rights Reserved. [Privacy statement](#). [Terms and Conditions](#). Comments? We would like to hear from you. E-mail us at customercare@copyright.com

A.9 Figure 4.9 (a)

12/12/2018

Rightslink® by Copyright Clearance Center



RightsLink®

Home

Create Account

Help

ACS Publications
Most Trusted. Most Cited. Most Read.

Title: Rashba and Dresselhaus Effects in Hybrid Organic-Inorganic Perovskites: From Basics to Devices

Author: Mikaël Kepenekian, Roberto Robles, Claudine Katan, et al

Publication: ACS Nano

Publisher: American Chemical Society

Date: Dec 1, 2015

Copyright © 2015, American Chemical Society

LOGIN

If you're a **copyright.com** user, you can login to RightsLink using your copyright.com credentials. Already a **RightsLink** user or want to [learn more?](#)

PERMISSION/LICENSE IS GRANTED FOR YOUR ORDER AT NO CHARGE

This type of permission/license, instead of the standard Terms & Conditions, is sent to you because no fee is being charged for your order. Please note the following:

- Permission is granted for your request in both print and electronic formats, and translations.
- If figures and/or tables were requested, they may be adapted or used in part.
- Please print this page for your records and send a copy of it to your publisher/graduate school.
- Appropriate credit for the requested material should be given as follows: "Reprinted (adapted) with permission from (COMPLETE REFERENCE CITATION). Copyright (YEAR) American Chemical Society." Insert appropriate information in place of the capitalized words.
- One-time permission is granted only for the use specified in your request. No additional uses are granted (such as derivative works or other editions). For any other uses, please submit a new request.

If credit is given to another source for the material you requested, permission must be obtained from that source.

BACK

CLOSE WINDOW

Copyright © 2018 [Copyright Clearance Center, Inc.](#) All Rights Reserved. [Privacy statement.](#) [Terms and Conditions.](#) Comments? We would like to hear from you. E-mail us at customer care@copyright.com